STARS

Electronic Theses and Dissertations, 2020-

2021

Development of RF-MEMS Based Passive Wireless Respiratory Monitoring Systems

Sina Moradian
University of Central Florida

Showcase of Text, Archives, Research & Scholarship

DEVELOPMENT OF RF-MEMS BASED PASSIVE WIRELESS RESPIRATORY MONITORING SYSTEMS

by

SINA MORADIAN
B.S. Iran University of Science and Technology, 2013
M.S. University of Central Florida, 2017

A dissertation submitted in partial fulfillment of the requirements
for the degree of Doctor of Philosophy
in the Department of Electrical and Computer Engineering
in the College of Engineering and Computer Science
at the University of Central Florida
Orlando, Florida

Spring Term
2021

Major Professor: Reza Abdolvand

ABSTRACT

This dissertation explores the application of high frequency, low loss, high quality factor thin-film piezoelectric MEMS resonators as passive wireless respiratory monitoring sensors. In this work we build on advances in RF MEMS technology and wearables to develop a respiratory monitoring system capable of measuring respiration without any on-board circuitry and battery First, a wireless MEMS-based respiration sensor that operates without a battery or any on-board circuitry is presented. The sensing system is made up two major components, the wireless sensor and a base transceiver and computational unit. The sensor is only made of up of two RF-MEMS resonators and a custom UHF RFID antenna. The base unit is composed of transmitter antenna connected to a signal generator, and a receiver antenna connected to an oscilloscope. The frequency of the MEMS resonator is highly sensitive towards both temperature and also water vapor condensation. This sensitivity results in the modulation of the resonator (and sensor) when exposed to respiratory airflow. For a mean excitation signal power of 80μW, the sensor was measured to be capable of recording the respiratory profile of human subject from distance of up to 2 meters away from the base transceiver unit. At a distance of 0.5 meters the sensor was measured to have a SNR of 124.8dB. Next, building on the above sensor and using a novel time-of-flight sensing technique a respiratory flow sensor with only 7.2cm^2 footprint was developed. To facilitate the time-of-flight sensor, two low

loss, high quality factor TPoS MEMS resonators are placed ~1cm apart and are connected to a small (3.8cm^2) planar ground antenna. We were able to measure flow rate and respiration profile of human subject from a distance of 20cm from the base transceiver.

ACKNOWLEDGEMENTS

TABLE OF CONTENTS

LIST OF FIGURES

LIST OF TABLES

CHAPTER ONE: INTRODUCTION

It is estimated that from the hundreds of millions burdened with chronic respiratory conditions globally, annually four million individuals die prematurely [1]. This immense humanitarian and economic toll can be alleviated with proper care and monitoring of respiratory function in at-risk patients [1], [2]. Also, respiration rate is an excellent predictor for the need to admit patients at-risk of cardiac arrest into intensive care units [3]. Some studies suggest the relative changes in respiration rate are a more significant indicator of at-risk patients than systolic blood pressure in the case of physiologically unstable patients [4].

Regardless of the accuracy of diagnostic tools, limited information gathering at in-clinic visits provides a narrow snapshot of the patient's physiology that is not measured under natural conditions [5]. This creates an inherent limitation in the quality of the clinical evaluation based on the results of diagnostic tools. In addition to diagnostic applications, studies have shown the benefit of long-term continuous respiration monitoring for patient's recovery [6]. As such, research results emphasize the need for respiration monitoring systems that are capable of continuously measuring respiration rate and depth [7].

Despite the stated benefits of monitoring the respiratory rate, research shows that the proper measurement is routinely neglected, even in cases where the patient's main

complication is a respiratory condition [8]. This could be the result of the relative complexity of conventional respiratory monitoring diagnostic tools that necessitate the patient to be connected to a stationary measurement unit with cables and tubes. Needless to say, this cumbersome setup renders continuous long-term monitoring impractical for most patients.

Monitoring systems designed to fill this gap in healthcare can be categorized based on whether the sensor comes into contact with the patient and also according to the physiological signatures that are monitored in proxy of respiration [9]. A good overview for contact-based methods is shown in Figure 1. The main categories are temperature [10], moisture content [11], , acoustic signature [12], cardiac activity [13], chest movement [2], flow rate [14]. An overview for each type is presented here and a deep dive into flow rate is provided in chapter 4. This categorization is primarily based on [9], [13], [15]–[17].

Figure 1. Overview of categories of contact based respiratory monitoring systems with breakdown of each category according to the sensing mechanism [9].

For a typical measurement environment, exhaled air has a significantly higher temperature as compared to ambient air with the difference having been measured to be up to 15C [18] for room temperature environment. Using a sensing mechanism with a relatively high response rate we can measure the respiration rate of the patient [19]. If calibrated appropriately, other signatures such as respiratory flow and tidal volume can also be measured using this type of sensor. This type of respiratory sensor can be further subdivided according to the sensing mechanism.

Thermocouple-based sensors operate based on the Seebeck effect [20] whereby a temperature gradient applied to the junction of two different conductive material creates a voltage difference between the two that is proportional to the temperature gradient [21]. By converting this voltage difference into temperature and monitoring that over time researchers have developed a mechanism for measuring respiration rate by placing the thermocouple it in the respiratory pathway [22]. The response time of this sensor was reported to be 0.5S and their accuracy was measured to be ±2.2C for the popular type-K thermocouple [23]. The response time and accuracy can be improved by reducing the size of the sensor optimizing the constituting material.

Thermistor-based sensors take advantage of material whose resistance changes as a function of temperature. By monitoring the resistance using front-end circuits such as Wheatstone bridge we can create a simple and effective temperature sensor. These sensors have the advantage of compacts design which enables them to be subtly integrated into wearables and low unit cost. A disadvantage of thermistor-based respiration sensors is their relatively long response time (in the order of seconds) [24] which disqualifies them for applications such as apnea that require fast response time.

A wireless thermistor-based respiration sensor is shown in Figure 2. Here, heat exchange between exhaled air and the thermistor modulates the operating frequency of the oscillator which is in turn sensed by the base unit. By plotting the changes over time researchers were able to measure respiration rate of a human subject [25].
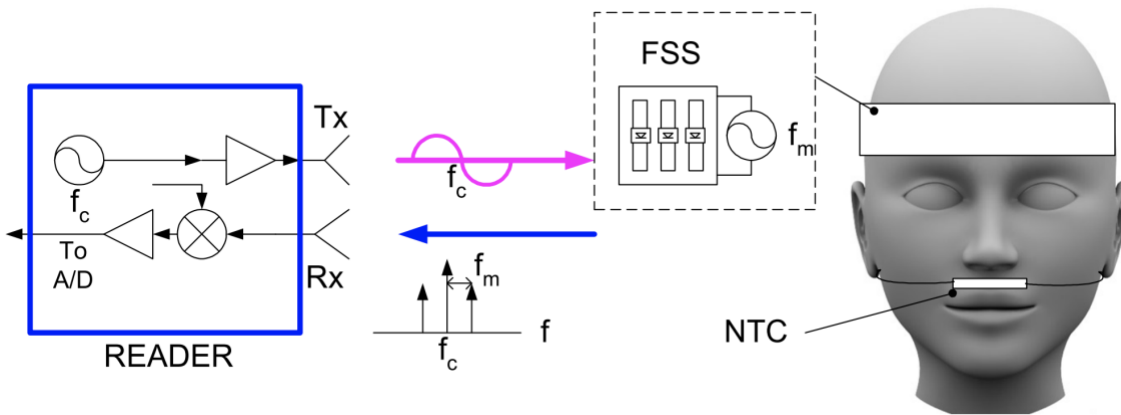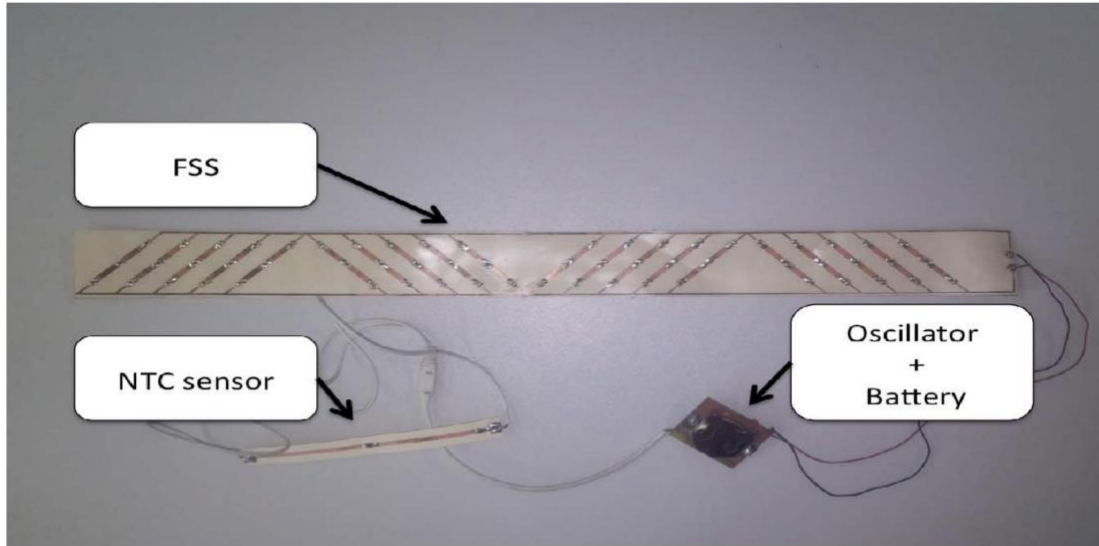
Figure 2. wireless thermistor-based respiration sensor composed of a NTC thermistor placed on the upper lip, and a capacitor bank, battery, and oscillator incorporated into a headband. Change in resistance of the thermistor results in a shift in operating frequency of the oscillator which is in turn measured by a base transceiver unit [25].

Pyroelectricity is a property of a group of crystals whereby a temperature induced change of atom positions modifies the polarization of the crystal and generates an electric voltage [26] which is then measured and calibrated against temperature. Accuracy of this type of temperature sensor has been measured to be ±1C [27]. It is important to note that

in pyroelectric sensors the output current is proportional to the rate of temperature change and not temperature itself. In [27] researchers incorporated a piezoelectric material with pyroelectric properties in a headphone's microphone (Figure 3) and utilized it to a patient's respiration rate.
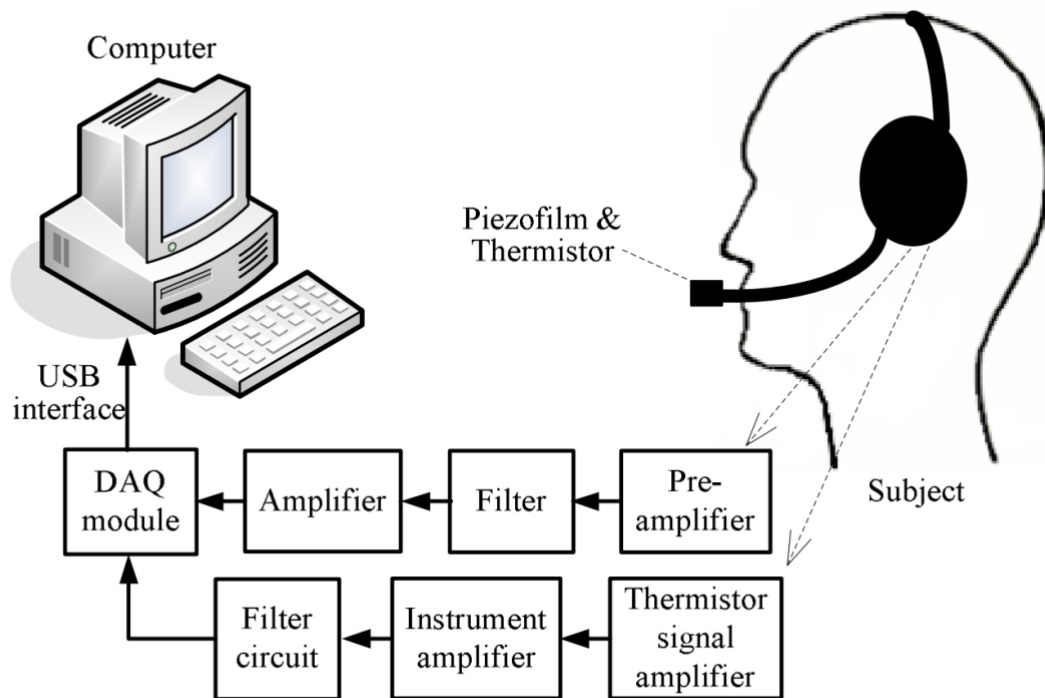
Figure 3. a piezoelectric film with pyroelectric properties is incorporated in a headphone form factor. Exhalation modulates the temperature of the film which is measured after signal conditioning by a computer [27].

Fiber optic-based temperature sensor operate based on modulation of the Bragg wavelength of a fiber optic by hot exhaled air. As the patient exhales, the Bragg wavelength temporarily shifts to longer wavelengths and then subsequently recovers

during inhalation. Fiber optic based respiration sensors have been shown to have a fast response time at 10ms [28] and are therefore not only suitable for respiration rate monitoring but can also can be used to detect minute changes in the respiration profile patients and enable new types of studies of the respiratory system. While optical fibers themselves are inexpensive, the costs associated with the systems needed to detect shifts in Bragg wavelength make this type of sensor prohibitively expensive for point of care applications [9]. Additionally, the mechanical fragility of optical fibers further complicates their applications as respiration monitoring systems. In [29] researchers added a polymer tip that shifts in color with temperature to a fiber optical cable and where capable of measuring respiration rate of a patient placed in an MRI machine. In this sensor, shown in Figure 4, the tip of the optical fiber is placed in the nasal pathway of the patient while an additional optical fiber is stuck on the abdomen. The former measures respiration by proxy of exhalation temperature and the latter uses movement of the patient's chest as the proxy.
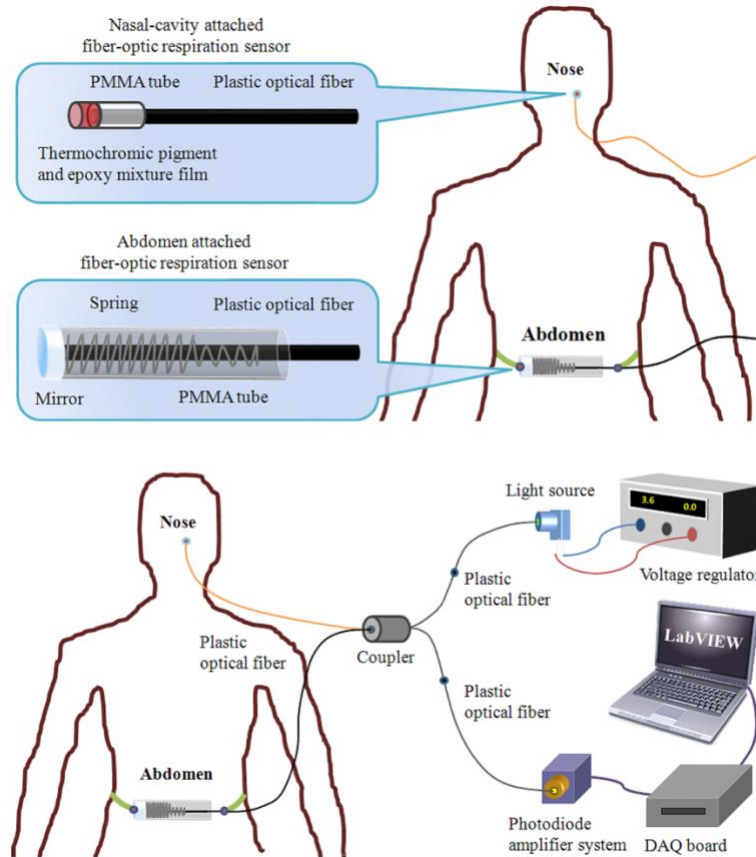
Figure 4. Fiber-optic based respiratory sensors designed to enable respiration monitoring in an MRI machine [29]. This sensing system has a secondary fiber optical respiratory sensor that uses strain to measure respiration.

Movement of the chest during respiration has been studied extensively as a proxy for monitoring the respiration system with a recent review paper concluding that 60% of publications on respiration sensors use some format of chest wall movement [17]. In addition to optical fibers [29] (Figure 4), capacitive [30], piezoresistive [31], piezoelectric [32], ultrasound [33], and accelerometer [34] sensing has been utilized for chest wall movement measurement of respiration. In [35] researchers utilized a wearable commercial

ultrasonic transducer operating at 2.2MHz and placed on the zone of apposition and was compared with other measurement techniques including spirometry, PCG, and acceleration. The front end of the sensing system, shown in Figure 5, is used to amplify the detected ultrasound echo and the resulting signal is passed onto an ADC following envelope detection.
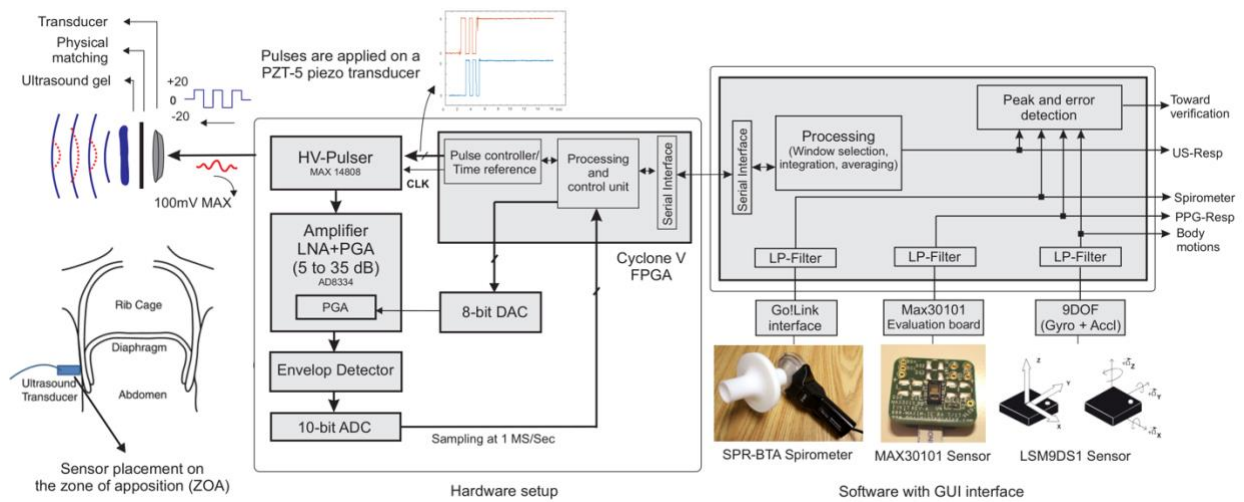
Figure 5. Respiration monitoring system using a wearable ultrasonic transducer operating at 2.2MHz. The sensing system detects deflections in the chest wall and converts that into a respiration profile [35].

An exciting active research topic is the utilization of advances in computer vision coupled with commercial IR [36], visible light [37] camera systems, or antennas [38] to detect chest movement and respiration rate.

Air exhaled from the respiratory pathway has a higher moisture content as compared to the typical measurement environment. By measuring the concentration of water vapor near a patient's respiratory pathway we can measure the respiration profile of the subject.

Different sensing techniques for measuring moisture content has been utilized for respiration with the most popular being capacitive [39]. The critical component of this type of sensor is a capacitor with a dielectric material that is responsive to changes in environmental moisture content. Modulation of moisture content stemming from exposure to respiration modulates the dielectric constant of the capacitor which in turn changes its capacitance. This capacitance is measured using front end circuits such as charge amplifier or oscillators. In [40] In_2O_3 nanocube-decorated GO nanosheets were used as a highly sensitive dielectric material. A oscillator based capacitive readout circuit is connected to the sensor and the entire module is integrated with wi-fi enabled STM32 microcontroller (Figure 6). Other categories include impedance [41] and fiber-optic based [42].
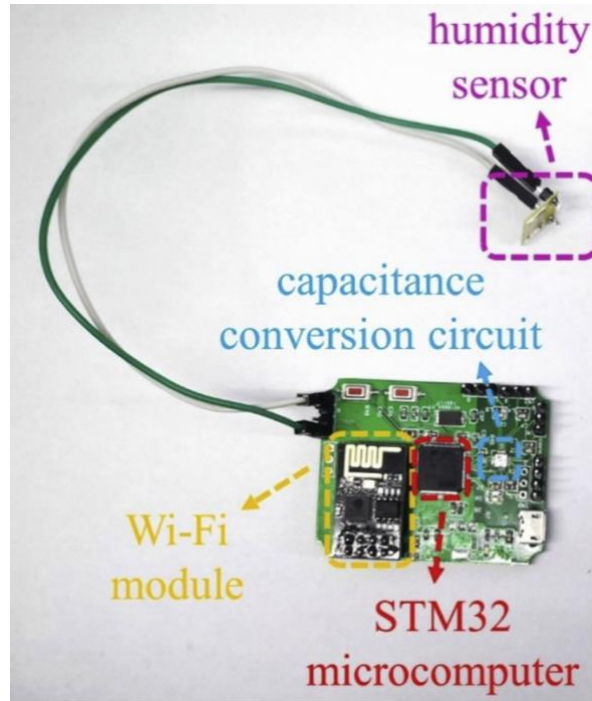
Figure 6. Capacitive humidity sensor composed of a In2O3 nanocube-decorated GO nanosheets layer. The change in capacitance of the sensor is measured using an oscillator type capacitance read-out circuit. A Wi-Fi module has also been incorporated into the sensing system to enable wireless operation [40].

Less common methods for measuring respiration profile include monitoring acoustic signatures of the respiratory system using one or multiple microphones [12], chemical analysis of exhalation for concentration of signature molecules such as CO_2 [43], and ECG [44] and PPG [45] based methods which use signal processing to isolate the respiratory signal from a signal generated by the cardiovascular system.

The diversity in developed respiratory sensing systems and the increasing number of publications in this field [17] reflect a need for respiratory monitoring systems that at the moment has not been met. The overarching trends that can be found are decrease in size sensing complexity, and unit cost and most importantly wearability.

While many of these sensors lend themselves to non-intrusive continuous long-term monitoring, typically their on-sensor circuitry and batteries increase sensor unit cost, footprint, and patient discomfort and hinder achievement of this goal. On the other hand, non-contact monitoring methods that enable patient comfort have difficulty measuring respiration profile, respiration flow, and respiration flow rate and are in most cases limited to measuring only rate of respiration.

To address these challenges and short comings, in this work a novel Thin-film Piezoelectric on Substrate (TPoS) RF-MEMS resonator-based sensor is presented. Ideally a wireless sensor should be small, lightweight, flexible, inexpensive, and durable. For the realization of these goals, we have opted for a passive wireless system instead of incorporating a battery in the sensor. The proposed sensing system is composed of a small, light-weight sensor that is attached to the upper lip of the subject and a base transceiver unit. The sensor itself is composed of custom antenna and a TPoS MEMS resonator, with the latter being responsible for the detection of the respiration profile. In the following chapter we will provide a background of piezoelectric MEMS resonators, the proposed sensor and its application for measuring respiration rate and profile is

12

shown detailed in chapter 3, and finally a highly novel flow rate sensor is explained in

chapter 4.

CHAPTER TWO: THIN-FILM PIEZOELECTRIC ON SUBSTRATE MEMS RESONATORS

Microelectromechnical systems (MEMS) have become essential for modern consumer electronic devices. Some important categories include MEMS microphones [46], inertial sensors [47], MEMS resonators used in oscillators [48] and RF filters [49]. Among these piezoelectric MEMS resonators used for RF front ends are one of the fastest growing categories.

The reversible conversion of mechanical energy (kinetic and potential) into electrostatic energy (stored in the electric field) is used to actuate piezoelectric MEMS devices. An electric field applied to a piezoelectric layer results in the propagation of stress waves throughout the microstructure. Microstructures are designed to harness the stress waves to actuate vibration modes. Without the formation of standing waves the amount of displacement from the stress created by electrically exciting the piezoelectric layer is extremely small and not enough to effectively excite microstructures.

In this work we utilize a specific type of piezoelectric MEMS resonator, Thin-film Piezoelectric on Substrate (TPoS) resonators. The major difference between TPoS resonators and other similar piezoelectric MEMS resonators [50] is the inclusion of a low acoustic loss substrate layer underneath the piezoelectric stack layer. The major advantages of TPoS resonators can be summarized as:

1- Acoustic waves traveling in the substrate layer experience lower loss compared to waves traveling in the piezoelectric layer. This results in a higher achievable quality factor. The most popular substrate material is single crystalline silicon, however in this work we have opted to use nanocrystalline diamond mainly for its lower loss and higher stiffness.

2- Increased volume and mass results in an increase in the resonator's power handling capacity [51]. This is critical for applications for which linearity of the resonator is critical.

3- Reduction of surface/volume ratio results in a decrease in surface loss for a given total stored energy.

4- Operational frequency is defined lithographically and is nominally not thickness dependent. This means that for a given wafer with a fixed substrate thickness we can develop resonators with a variety of frequencies.
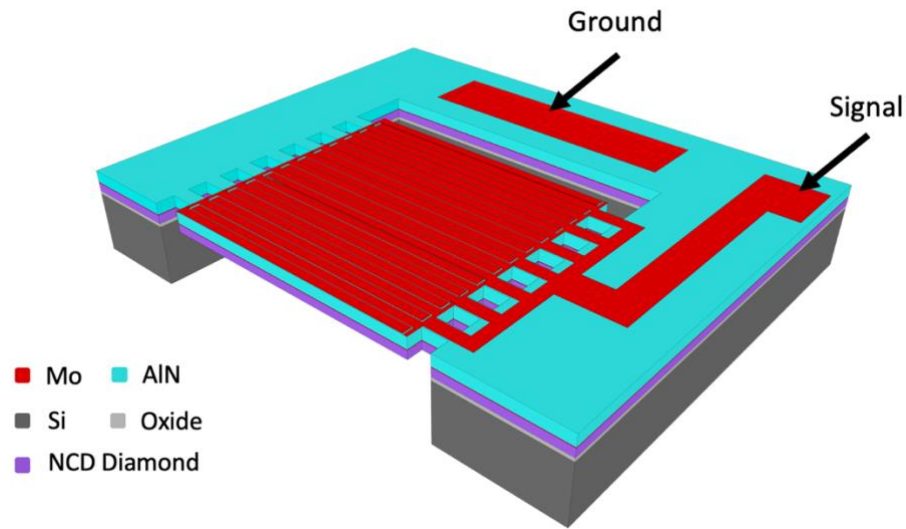
Figure 7. Schematic illustration of a 25th mode TPoS MEMS resonator operating in the lateral extensional mode [52]. The resonator illustrated here is configured as a 1 port device.

The stackup and structure of a diamond substrate TPoS MEMS resonator is depicted in Figure 7. The 25th mode resonator illustrated here is configured as a single port device with one ground pad and one signal pad. The stackup of the resonator consists of a low acoustic loss material such as single crystalline silicon or nanocrystalline diamond substrate layer with a metal-piezo-metal layers stacked on top.

The top metal is patterned to create an interdigitated finger pattern that makeup the input and output and the bottom electrode acts as the ground. Applying a voltage differential across the two metal layers creates and electric field between the two which in turn induces strain in the piezoelectric layer. In cases such as this thesis the resonator is utilized in a one-port configuration, meaning that the input is only applied to one of the two sets of inter-digitated fingers.

The TPoS MEMS resonators utilized in this work are designed to excite the lateral extensional mode. In this mode, as shown in Figure 8(b-d), the micromechanical structure oscillates in the XY plane and acoustic waves can be assumed to be longitudinal. The key to actuating this mode in a microstructure is designing the width of the interdigitated fingers to match that of half a wavelength of the desired frequency.

To calculate this wavelength, we first need to calculate the velocity of the acoustic wave at the desired mode. We can simply this problem by assuming that the resonator is homogenous (neglecting the piezoelectric and metal layers), its elastic properties are isotropic, and that length of an electrode finger is far larger than its width. With these assumptions the velocity of longitudinal acoustic waves can be calculated with Equation (1).

$$v = \sqrt{\frac{E}{\rho}} \tag{1}$$

Here, E is the Young's modulus of the substrate layer, v is the velocity of longitudinal acoustic wave, and ρ is the material density. We can then calculate the wavelength as $\lambda = v/f$. Given the extensive assumptions made, the calculated finger width can only be used as an initial point and extensive optimization needs to be performed using Finite Element Analysis (FEA) taking into account all the different layers and fabrication features such as backside etch window size.
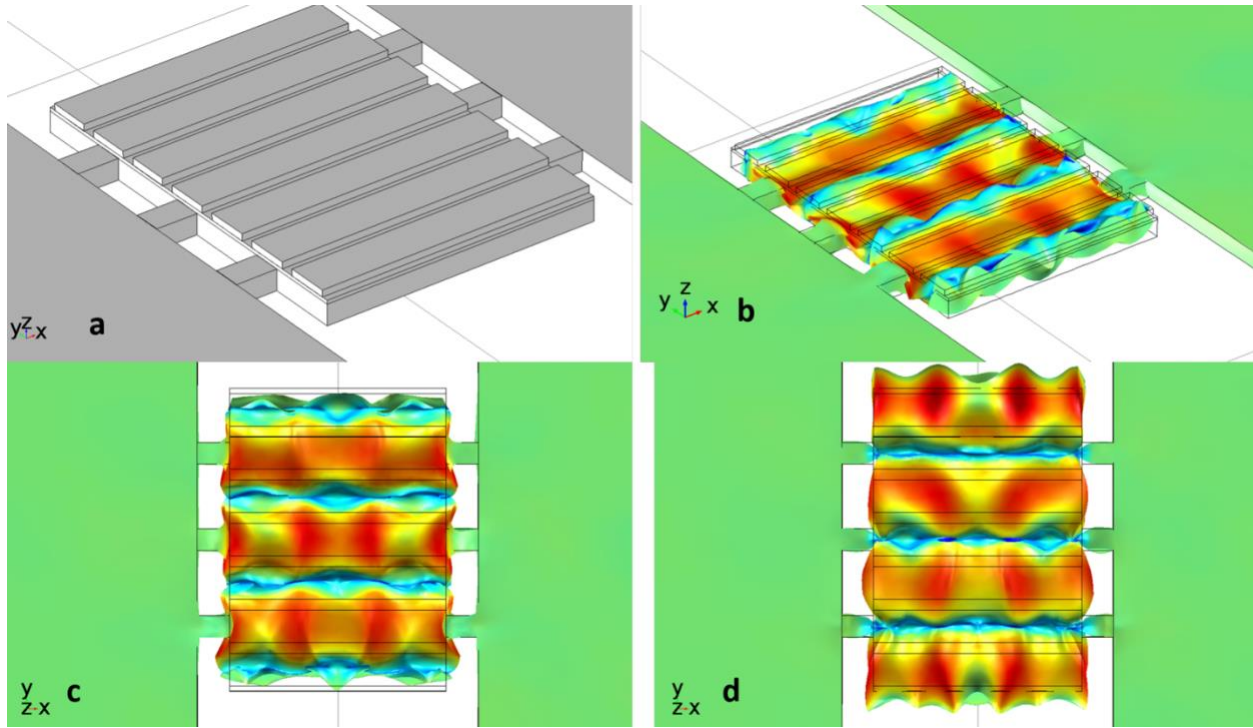
Figure 8. COMSOL Multiphysics FEA simulation of stress in the y axis for 7ᵗʰ mode resonator operating in the lateral extensional mode. (a) the resonator structure consisting of substrate, AlN, and top metal layers. The bottom metal is simulated as a 2D plane and cannot be seen in the schematic. The top metal electrodes are not drawn to scale. (b) side-view and (c) top-view of simulated y-axis stress with odd digit fingers at max compressive stress and the even fingers at max tensile stress. (d) top-view of simulated y-axis stress with odd digit fingers at max tensile stress and the even fingers at max compressive stress [53].

2.1 Butterworth Van Dyke model

To model the TPoS resonator we use the popular Butterworth Van Dyke (BVD) model [54]. The BVD model derives the values of a series RLC branch with a parallel capacitive

branch according to the frequency response of the resonator. The schematic of the equivalent circuit for a one-port resonator is shown in Figure 9.
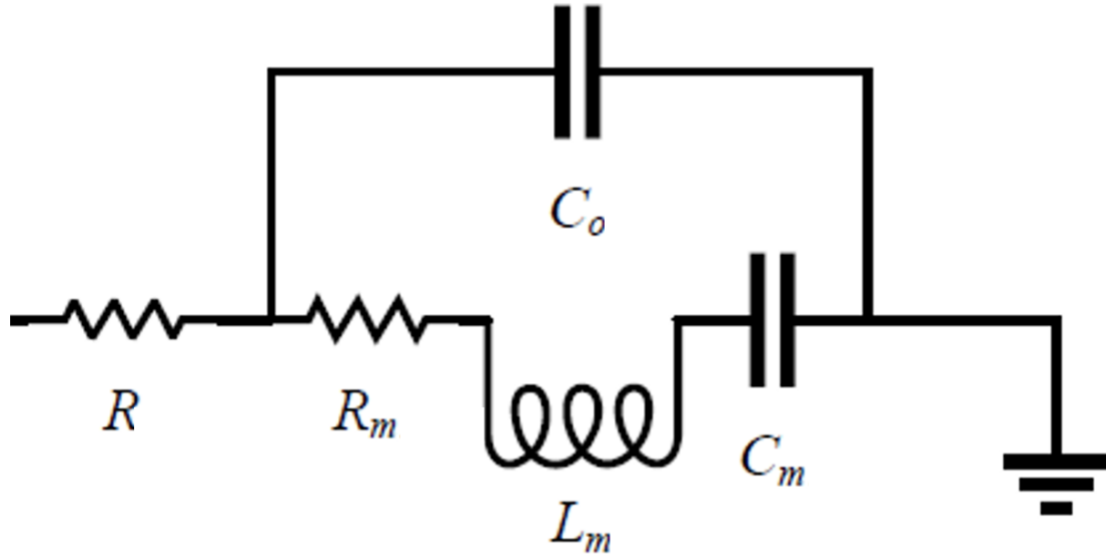
Figure 9. BVD model for a single resonance mode. The series RLC is the motional branch.

The series RLC branch is the motional branch and models the mechanical oscillation of microstructure and its effect on the electrical input and output. In this model R_m is the motional resistor, L_m is the motional inductor, and C_m is the motional capacitance. C_0 located in the parallel electrostatic branch is the capacitance formed between the signal and ground electrodes of the resonator. The parameters can be calculated from the impedance of the resonator as shown in Figure 10 using Equations (2-4).
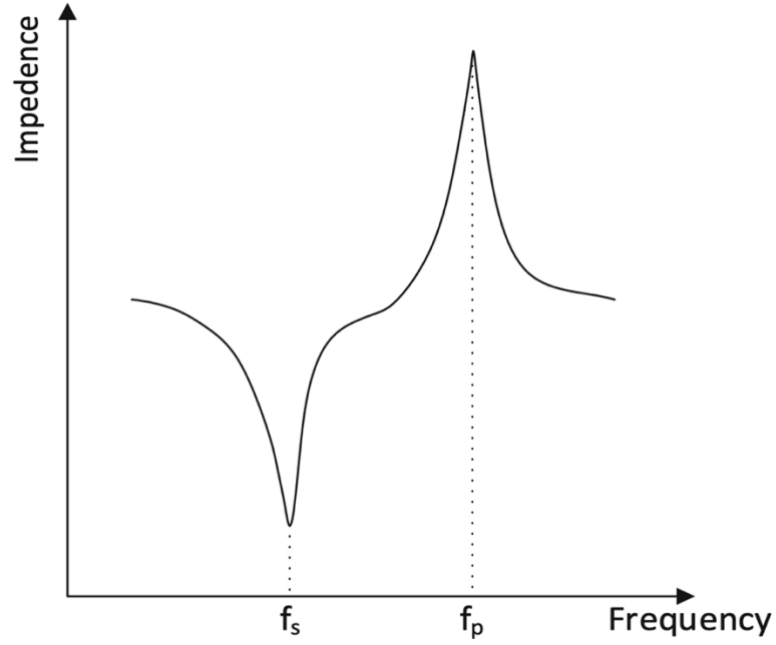
Figure 10. typical impedance response of a resonator for a given resonance mode with the series and parallel resonance frequencies highlighted [55].

$$f_s = \sqrt{\frac{1}{L_m C_m}} \tag{2}$$

$$f_p = \sqrt{\frac{C_m + C_0}{L_m(C_m C_0)}} \tag{3}$$

$$Q = \frac{\omega_0}{2} \frac{\partial(\angle Z)}{\partial f}\bigg|_{\omega_0} \tag{4}$$

2.2 Single port use of two port resonator

The resonators used in this work were originally designed in a two-port configuration. To determine whether to have the second port as an open termination or

short it by wirebonding it to ground pads, the impedance of the resonator was measured for the open port configuration using Rhode & Schwarz ZNB-8 Vector Network Analyzer (VNA). Based on this measurement and using Advanced Design System (ADS) the impedance magnitude and phase for port 1 for the shorted case was calculated and shown in Figure 11 and Figure 12, respectively. This change in impedance directly impacts the quality factor of the resonator through Equation (4). The quality factor for open port and shorted cases were calculated to be ~11000 and ~10100, respectively, representing an ~8% drop in quality factor. This result suggests that to maximize the effective quality factor of a two-port resonator, the second port should be configured as an open termination when applicable. For this reason, the second port of the resonators used in this work are all configured as an open termination.
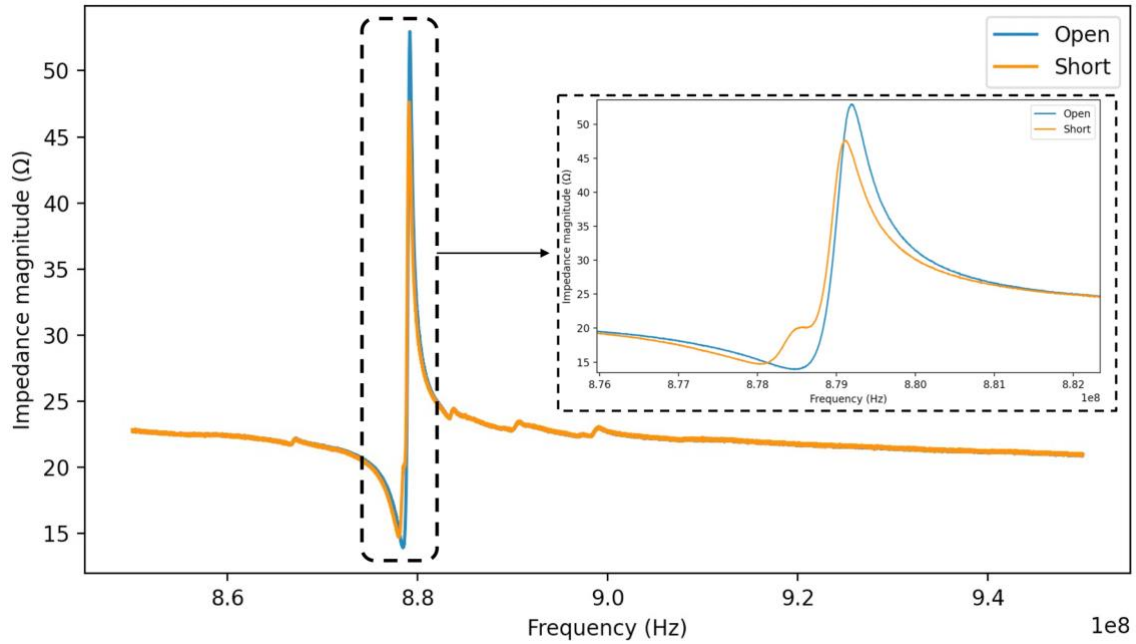
Figure 11 Impedance magnitude for port 1 of a two-port resonator for the case where port 2 is open and shorted.
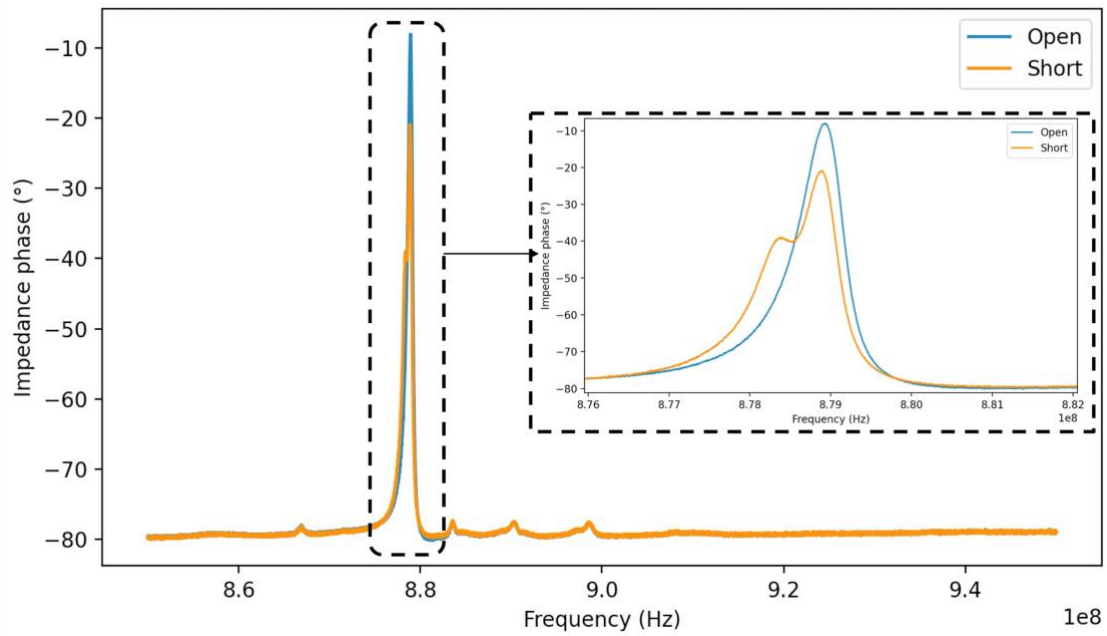
Figure 12 Impedance phase for port 1 of a two-port resonator for the case where port 2 is open and shorted.

To calculate the BVD model of the resonator measured in Figure 11and Figure 12 we first determine the series and parallel resonance frequencies. Here, using Figure 11the series (f_s) and parallel (f_p) resonance frequencies were measured to be 887MHz and 887.4MHz, respectively. Using this measurement, we can fine tune the values of the BVD model parameters to the measurement, using Equations (2-4) as a guiding tool. The BVD model of this resonator with the calculated parameters is shown in Figure 13 and the measured vs modeled impedance magnitude and impedance phase are shown in Figure 14 and Figure 15, respectively.

$$C_0 = 90fF$$

$$R = 10\Omega \quad R_m = 29\Omega \quad C_m = 2.5fH$$

$$L_m = 12.7\mu H$$
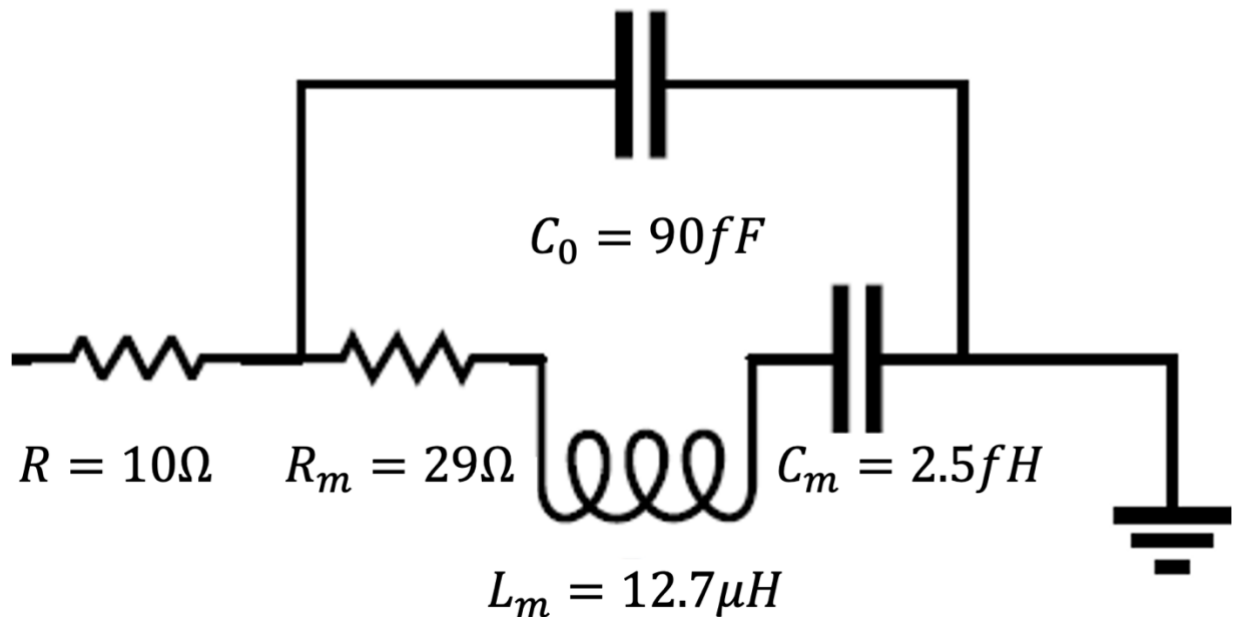
Figure 13 one port BVD model of diamond substrate TPoS resonator operating in the lateral extensional mode with the values for the various parameters highlighted.
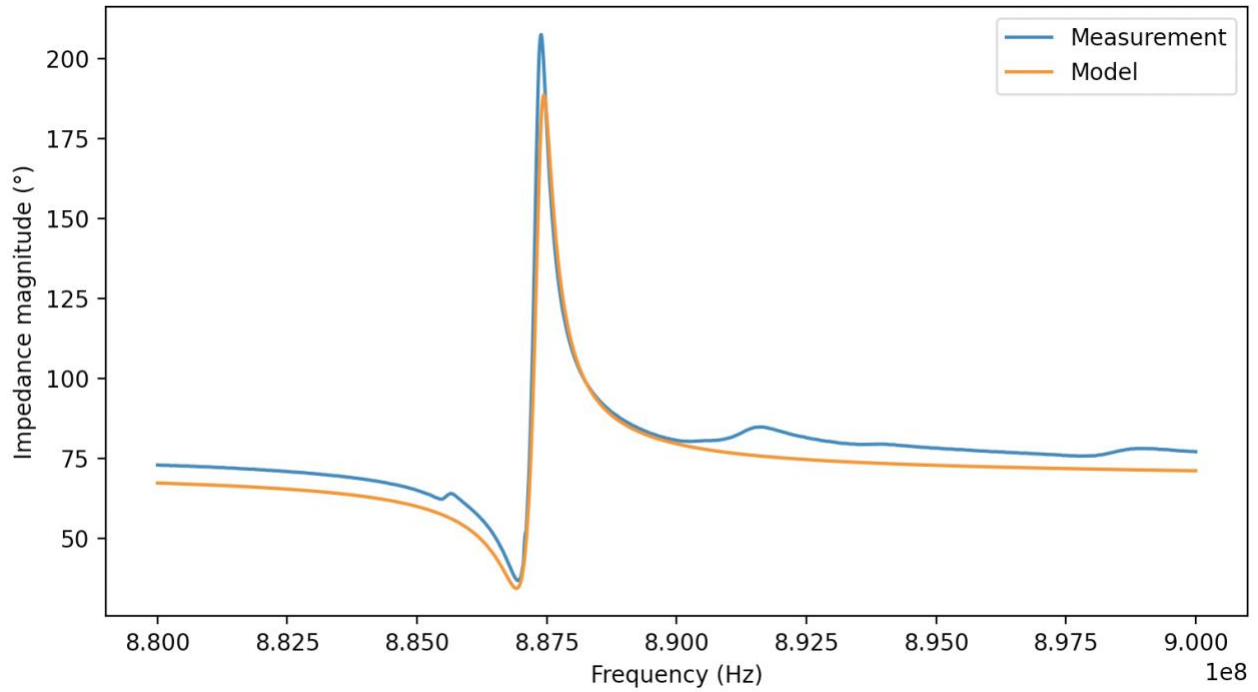
Figure 14 Impedance of TPoS MEMS resonator configured as one-port device, operating in lateral extensional mode. The series and parallel resonance frequencies are the minimum and maximum of the impedance magnitude shown here.
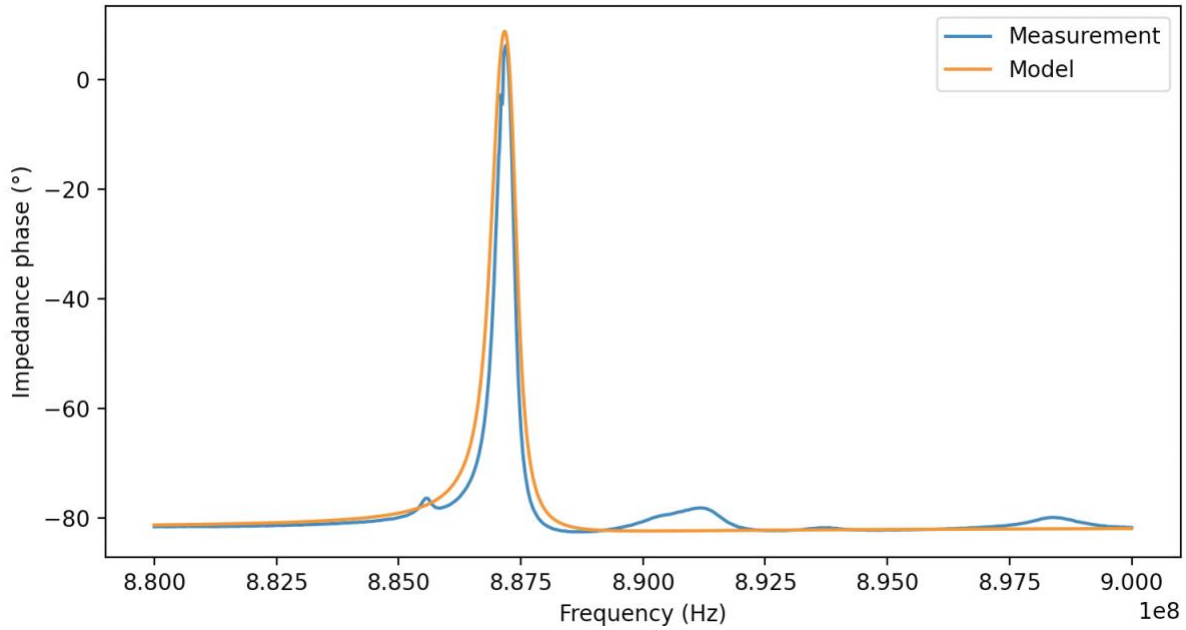
Figure 15 impedance phase of the TPoS MEMS resonator. The rapid change in phase around the resonance frequency is clearly visible.

2.3 TPoS MEMS device microfabrication

The process for fabricating TPoS resonators used in this work consists of 5 masks, as illustrated in Figure 16. To fabricate these devices, we start with a handle wafer made of polished single crystalline silicon. Next, this handle wafer is bonded with a thin oxide layer which will help act as an etch stop and help define the z dimension of the resonators. Depending on whether the substrate layer is silicon or nanocrystalline diamond the substrate layer is either bonded to the wafer or deposited using hot filament chemical vapor deposition. Following this, a 5nm of AlN thin film is sputtered on the wafer to both act as an electrical insulator and also to promote grow of c-axis crystalline orientation in the upcoming main AlN deposition by acting as a seed layer. Next, the a ~100nm layer of

Molybdenum is sputtered to form the ground plane of the wafer. Molybdenum has an advantage of having compatible crystal orientation with our desired c-axis AlN and therefore is suitable for this process. This layer is then patterned and etched in SF$_6$ plasma to form the ground electrodes of individual devices (Figure 16(a)).
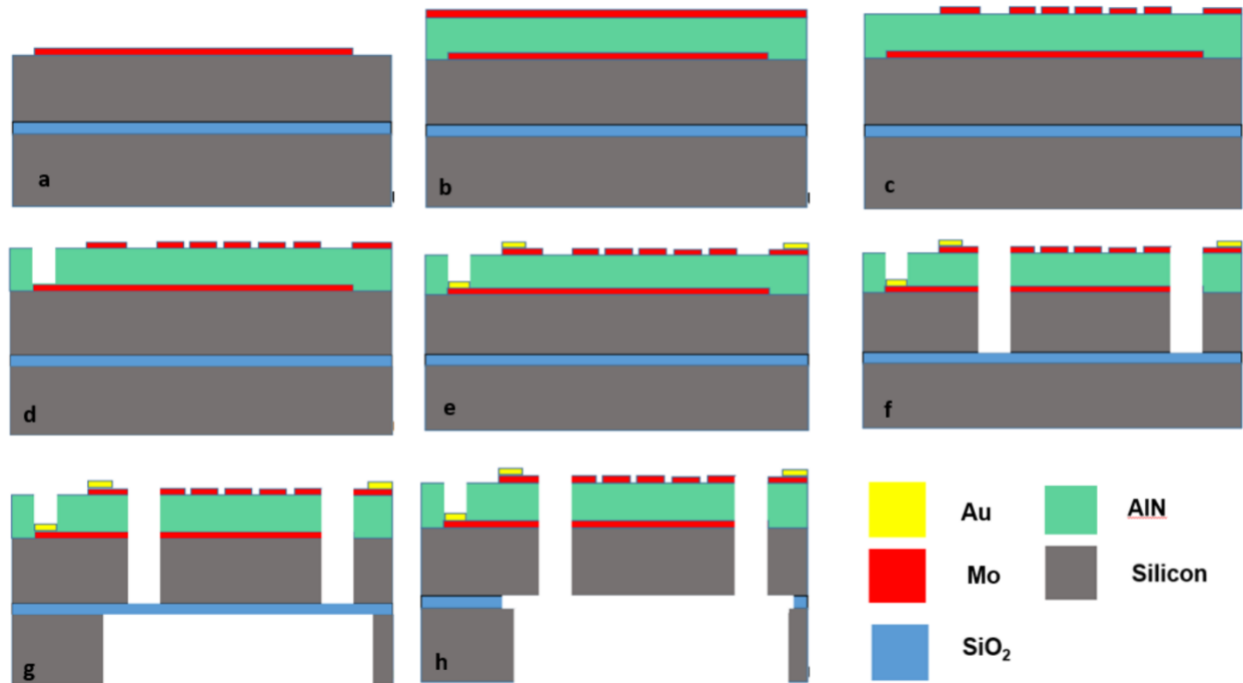
Figure 16. Process flow for fabrication of silicon substrate TPoS MEMS resonator [56]. In our case, the silicon substrate layer is substituted for a nanocrystalline diamond substrate layer.

In the next stage an AlN thin film with crystal structure highly oriented in the c-axis is sputtered on the wafer. The quality of the AlN thin film is critical for piezoelectric actuation therefore tight process control at this stage is crucial. In the next step, shown in Figure 16(b), a second Molybdenum layer with thickness of ~100nm is deposited. This layer is then patterned and etched (Figure 16(c)) to form the top electrode of the devices.

To gain access to the bottom Molybdenum layer windows are etched into the AlN layer by placing the wafer in a heated RD6 solution (Figure 16 (d)). It should be noted that prior to this step window patterns corresponding to devices bottom electrode pads are etched into an oxide mask to protect the AlN layer in other parts of the wafer. Time lapse of the AlN etching process as seen under a microscope is shown in Figure 17.
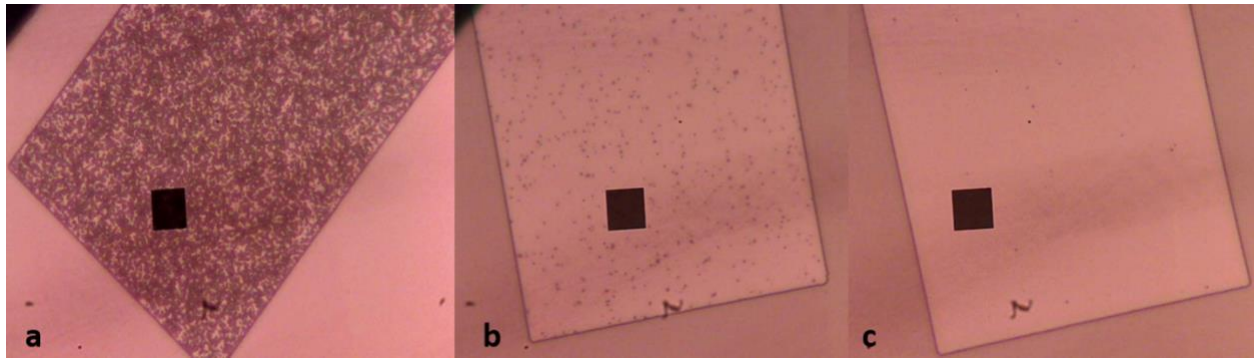
Figure 17. wet of AlN with RD6 solution heated to 90C (a) 30s, (b) 270s, and (c) 395s after the start of the etching process [53].

The top Molybdenum layer is then covered by a thin ~100nm gold layer with ~20nm Chromium layer to promote electrical contact between probes and the top and bottom electrode structures using e-beam evaporation and lift-off process. Because of the relatively high acoustic loss of gold, we do not deposit on the sections of Molybdenum residing on the resonators but rather the traces connecting the resonator to the contact pads (Figure 16 (e)).

Forming the geometry of the resonators necessitates etching out trenches in the stack (Figure 16(f)). This is accomplished by first depositing an oxide hard mask layer and

etching the AlN and bottom Molybdenum layer in BCl3/Ar/O2 plasma. Following this the diamond substrate layer can be etched in CF_4/O_2 plasma. In the case of devices with silicon substrate the DRIE process is preferred for etching silicon as it promotes perpendicular sidewall profiles.

Given that the resonators need to be released from the backside a thick oxide mask is deposited on the backside of the wafer and patterned. Following the etching of windows into the oxide mask the handle silicon layer is etched in DRIE process until the buried oxide layer is completely exposed Figure 16(g). After stripping of photoresist, the wafer is placed in BOE solution to remove the oxide layer thus completely releasing the resonators (Figure 16(f)). Fully fabricated and released devices are imaged using SEM and shown in Figure 18.
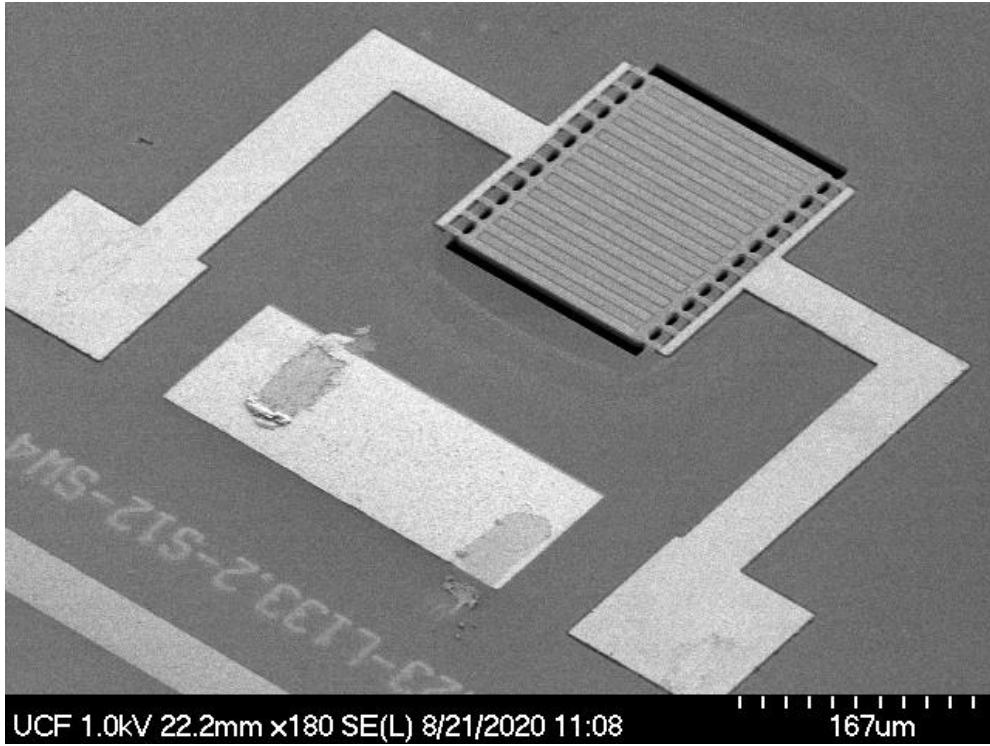
Figure 18. SEM image of high frequency TPoS MEMS resonator operating in the lateral extensional mode.

CHAPTER THREE: A BATTERY-LESS WIRELESS RESPIRATORY SENSOR USING MICRO-MACHINES THIN-FILM PIEZOELECTRIC RESONATOR

3.1. Introduction

Respiratory monitoring systems described in chapter 1 highlight the gap between current gold standard respiratory monitoring systems that severely restrict patient mobility and the need for monitoring systems that offer similar accuracy, reliability and richness of measurement data while being inexpensive and easy to use all while enabling patient mobility.

Respiratory monitoring systems created to fill this gap can be grouped based on the physiological signatures that are monitored in proxy of respiration [9]. The main categories are airflow temperature [10], moisture content [11], flow rate [14], acoustic signature [12], and chest movement [2]. While these sensors lend themselves to non-intrusive continuous long-term monitoring, typically their on-sensor circuitry and batteries increase sensor unit cost, footprint, and patient discomfort and hinder continuous[1] long-term monitoring.

---

[1] This material used in this chapter is taken from:

Moradain, Sina, Parvin Akhkandi, Junyi Huang, Reza Abdolvand, and Xun Gong, "*A battery-less wireless respiratory sensor using micro-machined thin-film piezoelectric resonators*", Micromachines, MDPI, to be published (March 2021).

Moradian, Sina, and Reza Abdolvand. "*Mems-based passive wireless respiration profile sensor.*" In 2016 IEEE SENSORS, pp. 1-3. IEEE, 2016.

In this chapter, we illustrate how high frequency TPoS MEMS resonators incorporated with a custom UHF RFID antenna can enable a lightweight, respiratory monitoring system that offers patient extensive mobility. This chapter builds on several iterations of this sensor. In previous work, we demonstrated for the first time a resonant wireless respiration monitoring sensor capable of measuring respiration rate without the use of onboard batteries or circuits [57]. With a weight of only 9 grams, a Micro-Electro-Mechanical (MEMS) resonator is connected to a commercial RFID antenna that operates in the ISM band (@902MHz) and was wirelessly energized from a transmitter.

Although this sensor offered a compact form-factor (~9cm^2), negligible thickness, and low unit cost, the relatively limited measurement range (~25cm) was less than desired. We extend this work by increasing the measurement range from a maximum of 25cm to 2 meters, improving motion-induced artifact resilience, and improving SNR and thus sensor accuracy without sacrificing the sensor's small footprint and low unit cost. We accomplish this by combining a custom-designed RFID antenna with a dual-mode low loss, high Q MEMS resonator. We demonstrated that using a proxy of moisture condensation and heat exchange, our sensor can wirelessly calculate human respiratory profiles.

In this chapter, first, the operation of the sensing system is described as well as the various components of the sensor and their interaction with respiratory flow. Next, the measurement system is illustrated and details such as the acquisition software and power

delivery to the sensor is described. Following this, the measurement results and conclusions of this chapter and detailed.

3.2. Systems Components and Methods

The sensor schematically illustrated in Figure 19 primarily consists of a nanocrystalline diamond TPoS MEMS resonator that is energized wirelessly from a transmitter antenna by a pulsed sinusoidal waveform. This excitation signal is generated by a signal generator. The resonator is energized during the on period of the pulsed sinusoidal excitation signal. During the off period of the pulsed sinusoidal excitation signal, the energized resonator sensor returns a decaying sinusoidal signal at its natural resonance frequency. This decaying sinusoidal signal is then transmitted by the sensor's antenna and is received for signal processing by the receiver antenna. In practice, the sensor's antenna and MEMS resonators do not operate independently and the resonance frequency of the MEMS resonator is in fact impacted by loading from the antenna and vice versa.

On the receiver side, the waveform picked up by the receiver antenna is recorded by the ADCs of the oscilloscope. Since this waveform contains both the excitation signal and the sensor's response we need to separate out the sensor's signature decaying sinusoidal waveform before any performing any other post-processing step. To achieve this time gating or a Fast Fourier Transform (FFT) window is applied.
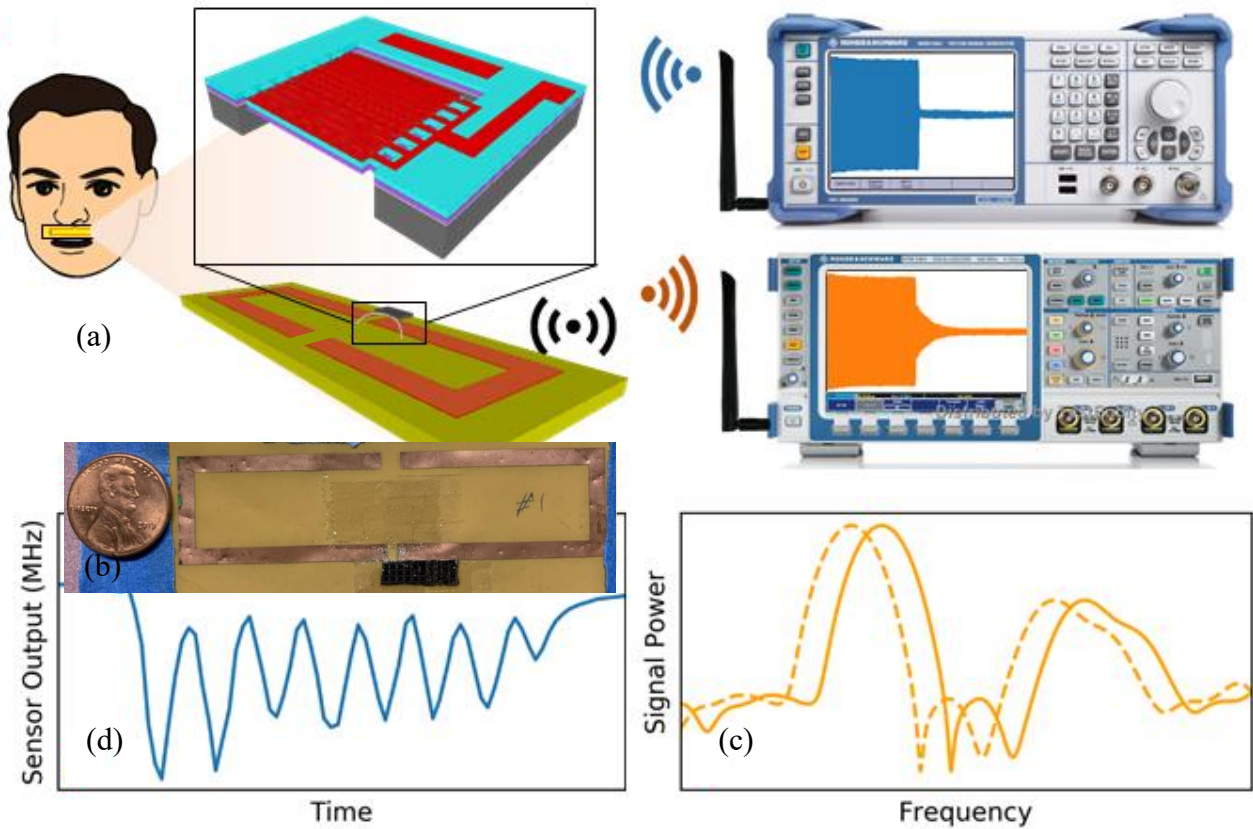
Figure 19. (a) A representation of the sensing device in schematic form. A pulsed sinusoidal signal (blue) from a transmitter excites the resonant sensor, and its response (orange) as seen by a receiver is analyzed using FFT. (b) An example of a sensor that was used in this research. (c) The resonators' downward frequency change as a result of respiratory flow exposure (d) Each fall and rise in frequency corresponds to a single respiratory cycle in the healthy subject's respiratory profile.

Energization of a given mode of a resonator is critically dependent on how well the frequency of the excitation frequency matches that of the resonance mode. Given that the sensor contains two MEMS resonators and multiple target resonance modes and the fact that in this setup we are limited to a single signal generator the signal generator is

programmed to successively target the individual target frequencies. This is complicated by the fact the sensor operates based on frequency modulation of the MEMS resonance frequencies as a function of respiratory airflow. This necessitates that the excitation signal's frequency be continuously updated to lock onto the MEMS devices resonance frequency. As will be detailed later on in this chapter this feedback loop is implemented via software.

In the next section, the critical criteria for choosing the MEMS devices and the UHF RFID antenna and the interaction of the MEMS devices with respiratory airflow is described.

3.3. Sensor Model

The sensor in this work's first design consisted of two RF MEMS resonators wire-bonded to a custom-designed flexible dipole antenna. This architecture aims to eliminate environmental effects including temperature variation and motional artifacts. The goal of this multi-resonator operation, as mentioned in the following sections, is to minimize the effect of environmental variability on the sensor.

We use TPoS MEMS resonators that operate near the ISM band in this application (902-928 MHz). The low insertion loss and high quality-factor of TPoS MEMS resonators were considerations in their selection [58]. These two factors are critical for the operation of this sensing system, as will be discussed further in this chapter. As described in chapter

2, the MEMS resonators used here, schematically shown in Figure 19, are made of a piezoelectric layer sandwiched between two metal layers stacked on top of a nanocrystalline diamond substrate. The piezoelectric layer is AlN with a thickness of 500nm, and the nano-crystalline substrate has a thickness of 3 μm. Beyond the details explained in chapter 2, readers are encouraged to see [59] and [60] to further understand the operation of the MEMS device, including the design and fabrication process.

To model this sensor, an equivalent circuit similar to what was described in chapter 2, was developed for the MEMS resonator. Here, the well-established Butterworth-Van Dyke (BVD) model [54] (detailed in chapter 2) is used. We model the effective mass, stiffness, and loss of a single resonance mode as a series inductor (L_m), capacitor (C_m), and resistor (R_m), respectively, by configuring the resonators in one port format. Furthermore, the energy stored in the electrical field generated between the ground and signal electrodes is represented in parallel with the series RLC mechanical branch as a capacitor (C_0). In addition, a resistor representing the resonator's ohmic losses is connected in series with the other components. In transmitting and receiving modes, the antenna was modeled as a complex load in series with a voltage source.

Near the ISM band, MEMS#1 has two target resonance modes. Both modes were modeled separately as two independent series RLC branches with a shared parallel capacitance and series resistance (highlighted in green and grey boxes). The

comprehensive sensor model including the antenna and the calculated BVD model values

for the two MEMS resonators used in this work is shown in Figure 20.
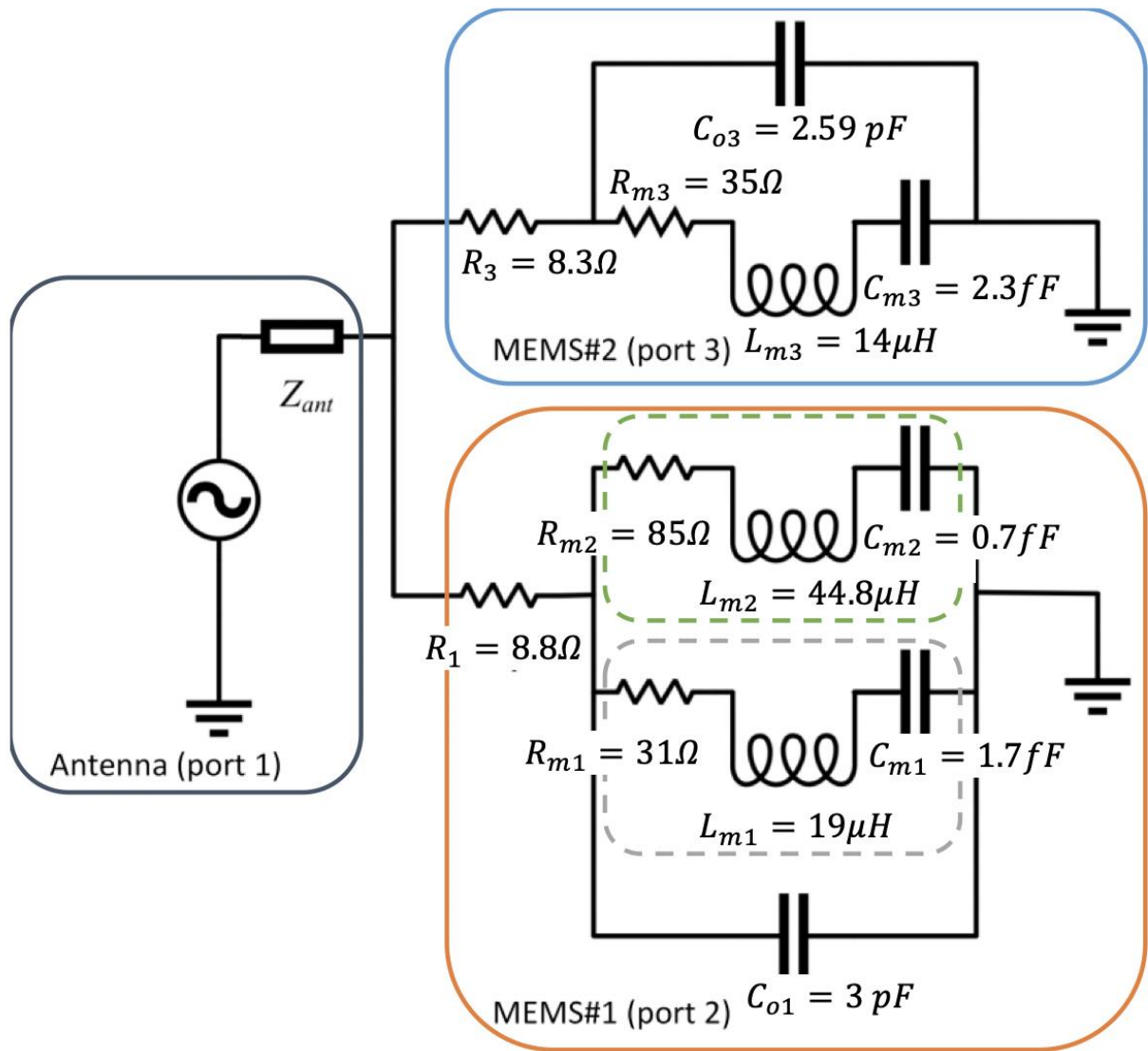
Figure 20. The sensor's equivalent circuit model in receive mode. The mechanical branches corresponding to each of the two modes are outlined in green and grey, and the model of the sensor MEMS (MEMS#1) is outlined in orange. The reference device's model (MEMS#2) is outlined in light blue. In receive mode, the antenna is modeled as a voltage source in series with a complex load (dark blue).

Figure 21 depicts the impedance responses of the two resonators that will be used for sensing. The modes of interest were measured at 874.7MHz, 879.9MHz, and 888MHz with unloaded quality factors of 1212, 2750, and 1750, respectively. The similarity between two MEMS devices' resonance frequencies helps in the design of a dipole antenna that is efficient at both frequencies. However, if the resonance frequencies are too close together, the modes may be misidentified during measurement. The impedance response for the two resonators derived from the BVD model values detailed in Figure 20 is plotted in Figure 21 and shown to be in good agreement for impedance phase and impedance magnitude. A small spurious mode centered at 881.5MHz is largely attributable to the presence mismatch between measurement and modeled values for MEMS#1 within 881MHz-882MHz range. This spurious mode was not modeled or studied in this work as it was found to be too close to the main mode centered at ~880MHz to be useful for sensing applications.
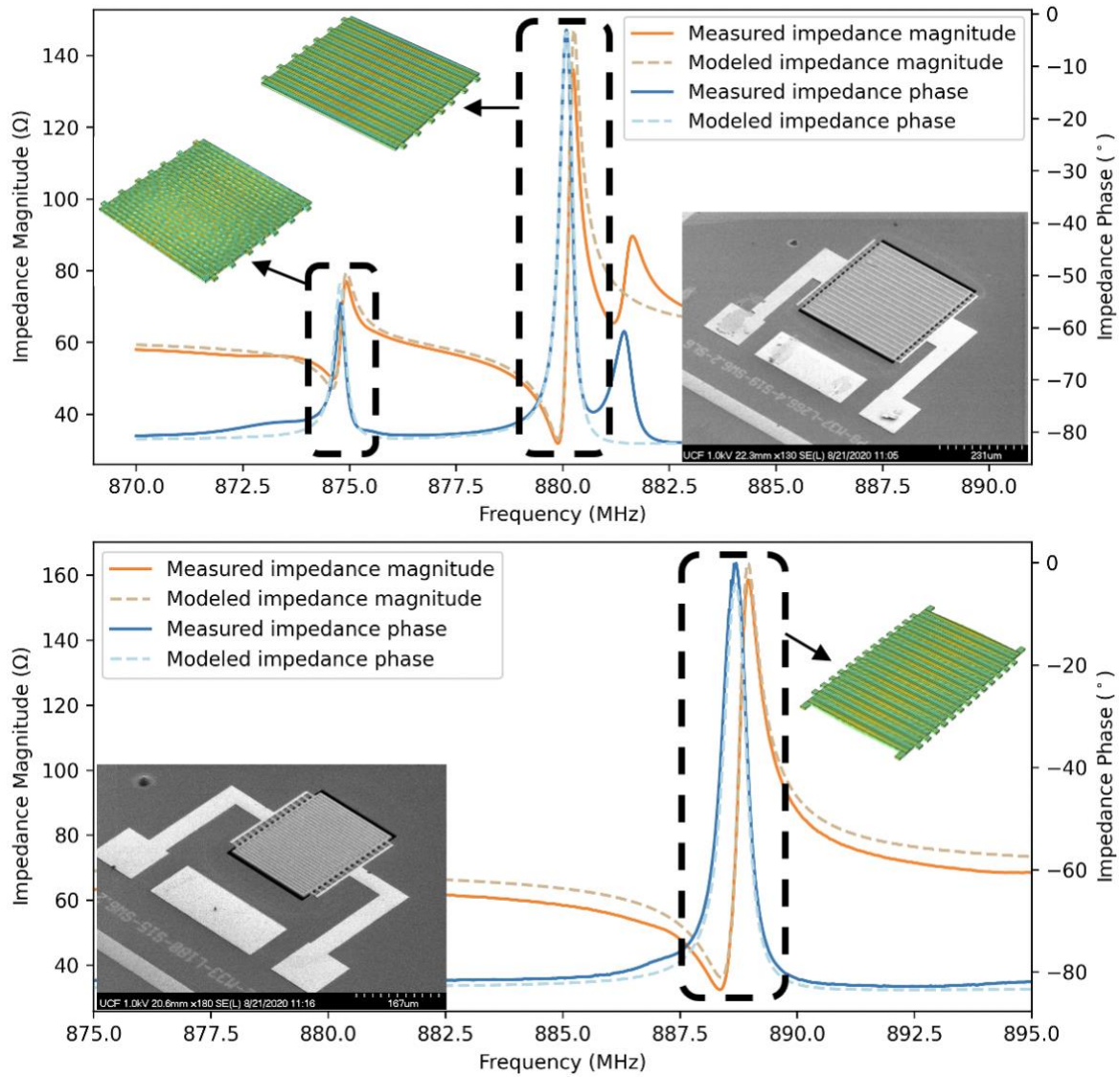
Figure 21. The modeled and measured impedance magnitude and phase of (a) MEMS#1 and (b) MEMS#2 resonators. COMSOL Multiphysics simulated mode shapes corresponding to each of the 3 modes.

39

3.4. Sensing Mechanism

The placement of the sensor on the upper lip region of the human subject, with the MEMS resonators aligned with the nasal pathway (see Figure 19) guarantees that air inhaled into and exhaled out of the nasal pathway interacts with the MEMS resonators. The impact that this exposure has on the MEMS resonators can be thought of in terms of modulation of both the MEMS resonators' temperature and vapor condensation on the surface of the devices.

Temperature change in the resonator has the primary effect of changing the effective stiffness of the resonator's constituting material. In our case, the stiffness of the constituting material, AlN, Molybdenum, and nanocrystalline diamond decreases with increase in temperature [59]. From Equation (1) we know that decrease in stiffness results in a decrease in resonance frequency. For a given respiration induced temperature change of ΔT the frequency shift can be calculated as:

$$\Delta f_T = TCF \times f_0 \times \Delta T \qquad (5)$$

Here, TCF is the temperature coefficient of frequency and has been measured to be effectively constant (~-9.6ppm) in the temperature range of interest for the targeted lateral extensional resonance mode of the TPoS MEMS resonators [59] targeted here and f_0 is the initial resonance frequency of the same mode.

The frequency shift as a function of temperature was simulated using COMSOL for all three modes measured in Figure 21. The resonance frequency for a given temperature is simulated from eigenmode analysis. To achieve this, first, the Temperature Coefficient of Elasticity (TCE) of the AlN and Mo layers were extracted from [61] and [62], respectively. Next, using these values we extract the TCE of the resonators' nanocrystalline diamond layer by fitting the simulated temperature-frequency profile to the measured profile. Knowing this value, we can simulate the temperature-frequency profile of all 3 modes, as shown in Figure 22. Therefore, for of all 3 modes of interest in the sensor, the increase in temperature associated with exhalation is expected to result in a drop in resonance frequency.
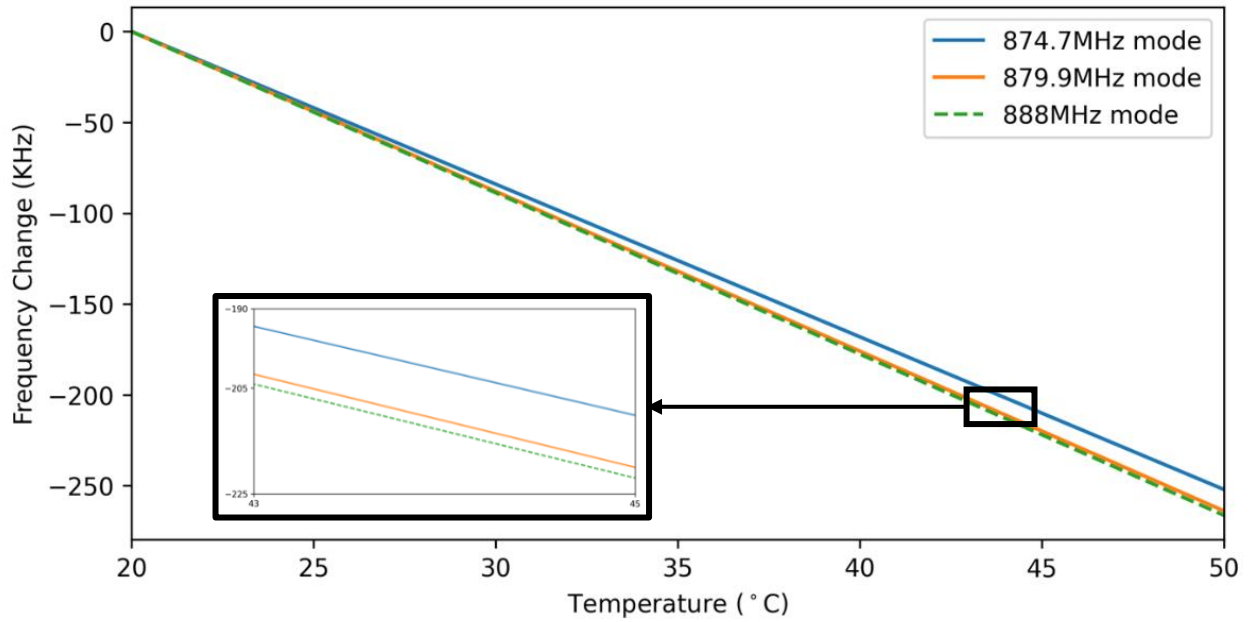
Figure 22. Simulated temperature-frequency profile of 874.7MHz and 879.9MHz modes of TPoS MEMS resonator used in the sensor. This resonator is fabricated on a 3μm nanocrystalline diamond-on-silicon substrate covered by 500nm of sputtered AlN. The frequency change profile of the 879.9MHz and 888MHz modes is very similar because of their common operating mode and the small variation can be attributed to the difference in center frequency.

The second major impact of exposure of the MEMS resonators to exhalation is surface vapor condensation. As exhaled air with high moisture concentration passes over the MEMS resonator a thin layer of water vapor condenses on the surface of the device. This thin layer increases the effective mass of the resonator proportional to its coverage and thickness. Modeling a MEMS resonator as a mass-spring-damper system the resonance frequency can be calculated as:

$$f_0 = \frac{1}{2\pi}\sqrt{\frac{k}{m_0}} \tag{6}$$

Here, m_0 is the initial effective mass and k is effective stiffness. Assuming a small mass loading term (Δm) the frequency shift is calculated to be proportional to the effective mass of the adsorbed water vapor:

$$\Delta f_m = -\frac{f_0}{2m_0}\Delta m \tag{7}$$

Adsorption of moisture induces higher acoustic energy loss due to both acoustic mismatch between condensation and the micromechanical structure and high acoustic loss in the condensation layer, in addition to mass loading.

Surface condensation and temperature increases cause a reversible drop in the resonance frequency of MEMS devices through different coupling pathways. However, the resulting frequency change due to both mechanisms is of the same polarity, which is critical for our application (negative). Temperature changes and vapor mass loading are both time-varying periodic parameters that are related by heat transfer during vapor condensation and evaporation. As a result of exposure to respiratory flow, the total sensor frequency change corresponding to a single resonance mode can be written as:

$$\Delta f(t) = -\frac{f_0}{2m_0}\Delta m(t) - TCF \times f_0 \times \Delta T(t) \tag{8}$$

3.4.1 Environmental Interference

When considering environmental variability, the same sensing pathways that promote respiration sensing may also serve as a source of measurement error. Any change in temperature, including environmental temperature, results in a change in the resonators' resonance frequency, as defined in Equations (3, 4) and illustrated in illustrated in Figure 22. If the transition is abrupt (as in exposure to sunlight and the opening of the refrigerator door), it may be misclassified as a respiration event.

As shown in Figure 22, the temperature-frequency profile of the 879.9MHz and 888MHz modes are almost identical in the 20-50°C range. By monitoring the difference in resonance frequencies in effect we can distinguish frequency change stemming from environmental temperature variation from respiration.

$$\Delta f_{888}(t) - \Delta f_{879.9}(t) = \left[-\frac{f_0}{2m_0} \Delta m(t) \right]_{888} - \left[-\frac{f_0}{2m_0} \Delta m(t) \right]_{879.9} \tag{9}$$

As a result of environmental electromagnetic loading, the RFID antenna exhibits slightly different impedance characteristics. As a consequence, motion-induced artifacts caused by spatial and temporal changes in surrounding objects will affect the sensor. Since the shift in sensor frequency induced by motional artifacts is supposed to be identical for different modes, we can differentiate respiration from such artifacts by monitoring the

difference in the resonance frequency of two different modes. In section 3.7 of this chapter, the feasibility of the two compensation methods is investigated experimentally.

3.5 Antenna Design

TPoS resonators through temperature and surface vapor condensation were found to be good candidates for resonant frequency modulated respiratory sensors. However, their application for wearable applications is entirely dependent on the development of robust, lightweight, high performance, and omnidirectional RFID antenna. While many commercial RFID antennas meet the above criteria, they are custom designed for a specific RFID tag chip and therefore cannot be used for our MEMS resonators. Critically, impedance mismatch between the MEMS resonators and antenna is a major source of efficiency loss and thus must be kept at a minimum.

One solution to this problem is the utilization of commercial RFID antennas combined with an on-sensor matching network between the resonators and antenna. Given the multiple resonance modes this approach would significantly complicate the design of the sensor, increase unit cost and weight, and also increase the sensor loss. As a result, in this work we opted to develop a custom UHF RFID antenna, specifically designed for the MEMS resonators measured in Figure 21.

A custom dipole antenna with in plane dimensions of ~2×6.5 cm^2, unnoticeable thickness, and a mass of only ~10g was created. The design of this antenna was based on

[63], in which a simple uniplanar antenna was developed for RFID tag applications. This compact design has the major advantage of straightforward impedance tunability.

The design and fabrication of the antenna used here was performed at Antenna, RF and Microwave Integrated Systems (ARMI) Laboratory at UCF by Junyi Huang under the supervision of Dr. Xun Gong.

The S-parameters of the MEMS resonators were characterized using the Rhode & Schwarz ZNB-8 Vector Network Analyzer (VNA) to design the antenna. The most challenging aspect of designing this antenna is achieving appropriate impedance matching between the antenna and the MEMS sensor, considering the fact that their impedances are different at their respective resonance frequencies.

Rather than exactly matching the antenna at only one of the MEMS resonance modes, we aligned the regression line of the corresponding MEMS sensor impedance at all resonance modes. The equivalent impedance was calculated using the Keysight Advanced Design System (ADS). Although power loss due to impedance mismatch is not removed in any of the MEMS sensor resonance modes, this design achieves the lowest overall impedance mismatch. It's worth noting that this antenna was built specifically for 879.9MHz and 888MHz frequencies.

In this first step of the design process the antenna's effective length is calculated to correlate with half a wavelength of the center frequency with the center frequency being between the 879.9MHz and 888MHz modes. Next, using this effective length, initial values

for the critical dimensions of the antenna (as highlighted in Figure 23(a)) are set. In the

next step, ANSYS High-Frequency Structure Simulator (HFSS) is utilized to simulate the

performance of the antenna. The design is judged based on how well it is matched to the

MEMS resonators, radiation efficiency, and radiation pattern. The final step entails

iterative fine tuning of the critical design dimensions to optimize the antenna design and

achieve good level of matching with the equivalent impedance of the two resonators.

This finetuning process is illustrated in Figure 23(b-c). Through experimentation the

imaginary and real components of the antenna's impedance response were found to be

mostly sensitive to L_3 and L_1, respectively.
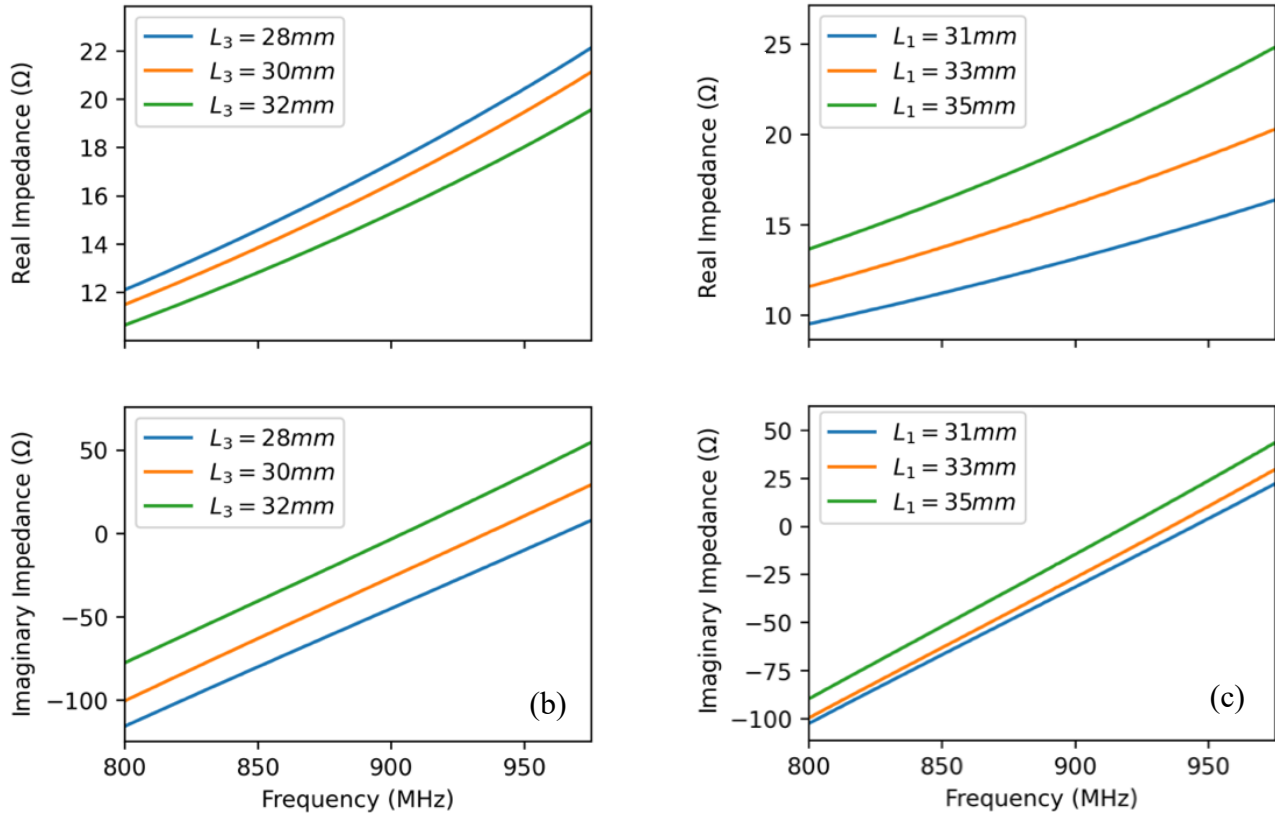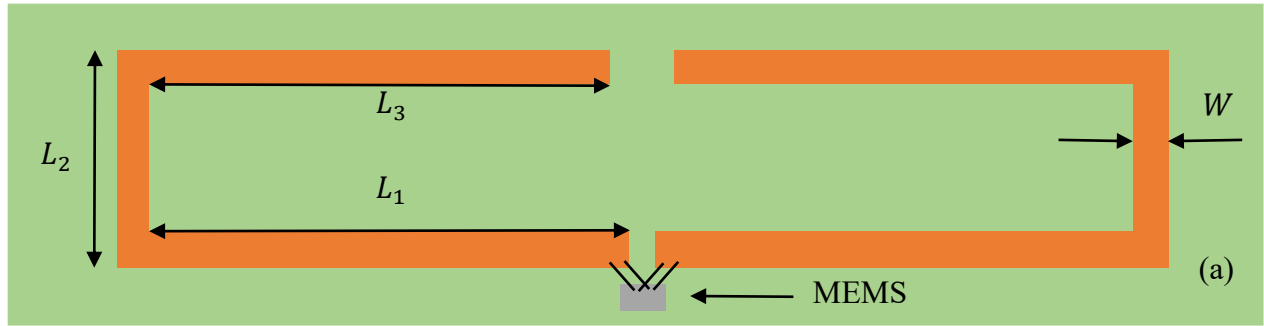
Figure 23. (a) The essential design vectors of the RFID antenna are illustrated in this schematic of the sensor. (b) Simulated impedance antenna for L_3 sweep and W=3mm, $L_1 = 33mm$, and $L_2 = 33mm$. (c) Simulated impedance antenna for L_1 sweep and $W = 3mm$, $L_2 = 33mm$, and $L_3 = 30mm$.

The impedance of the final design along with the fabricated antenna is shown in Figure 24. The optimized dimensions were found to be W=3mm, $L_1 = 35mm$, $L_2 = 20mm$, and $L_3 = 37.2mm$.

The print-screen method [63] was selected to fabricate the antenna optimized in the final design. The antenna was made from a thin flexible Pyralux copper laminate sheet. The thickness of the conductive copper and polyimide layers stands at 35μm and 25μm, respectively. To create the antenna pattern, we need to selectively remove copper from the sheet. A paper mask is laminated onto the Pyralux sheet using a heat gun forming a protective layer on the desired antenna pattern. Following this step, the Pyralux sheet is submerged in copper etchant for approximately 4 minutes. Following etching, the mask is carefully removed from the sheet exposing the desired copper pattern.

To calculate the expected power transfer efficiency (power delivered to the resonators and not reflected) the impedance response of the final design was exported. Using this model and the measured impedances of the MEMS resonators we can calculate how well the antenna can deliver power to the difference resonance modes with ADS. The summarized results shown in Table 1 illustrate the loss experienced by the signal in dB. Converting these values to efficiency% we can see that the efficiency was calculated to be noticeably higher for the 879.9MHz and 888MHz modes at 77.6% and 81.7%, respectively as compared to the 874.7MHz mode at 20%. This difference can be mainly attributed to the significant difference in impedance at 874.7MHz compared to the other two modes. It

should at the time of the design of this antenna, only the 879.9MHz and 888MHz modes were being considered.
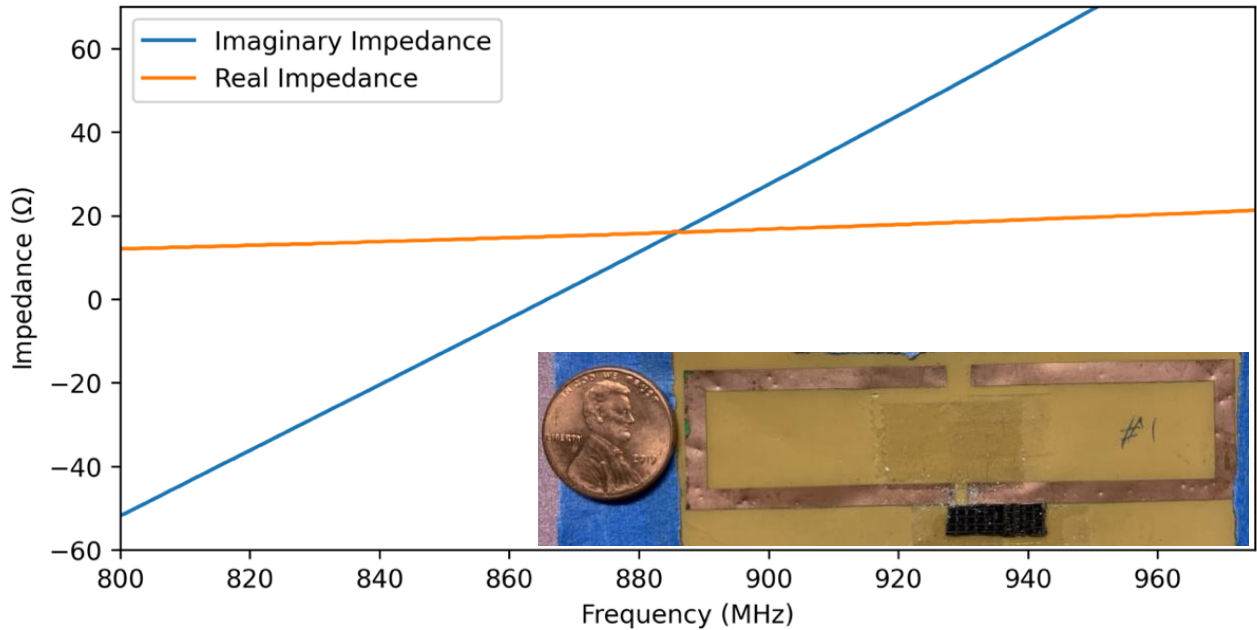
Figure 24. The finalized measured real and imaginary impedances of the final antenna design with fabricated antenna inserted as inset.

Table 1 The efficiency of power transfer between the final antenna configuration and three MEMS resonance modes was simulated. The sensor and reference devices are MEMS1 and MEMS2, respectively. Figure 20 shows the MEMS and port Figure 20.

Resonance mode (MHz)	$Z_{antenna}$ (Port 1)	Z_{MEMS1} (Port 2)	Z_{MEMS2} (Port 3)	S11(dB)	S21(dB)	S31(dB)
874.7	15.6 + 5.8j	24.109 - j44.57	21.91-j24.3	-3.5	-3.5	-9.6
879.9	15.9 + 9.9j	24.3 - 19.9j	9.9- 60.9j	-11.3	-0.8	-10.5
888	16.4 + 16.9j	9.1 - 62.4j	21.9 - 24.3j	-14.1	-10.2	-0.6

3.6 Power Delivery to Sensor

In the previous section we showed the extensive steps that were undertaken to minimize reflection of power at the interface between the resonators and antenna. We saw how this necessitated the development of a custom RFID antenna. Antenna-resonator mismatch, while critical, only minimizes the loss in power delivered to the resonators from the antenna and has a lesser impact on the power delivered to the antenna by the transmitter. In this section we study the parameters that are similarly important in determining how much power is delivered to the sensor, and ultimately the level of signal we should expect at the receiver given the value of the other critical parameters.

Given that the sensor does not contain any on-board power source, the magnitude of the excitation signal as received by the sensor directly impacts the maximum distance the patient can move from the transceiver unit without the sensor failing. Even in the case were the patient does not require extensive mobility minimizing the signal loss in various section of the sensing system enables us to reduce the exposure of the patient to high power RF signals.

For this reason, we have built on existing equations and developed a novel framework that connects the transmitted power to antenna characteristics, sensor-transceiver distance, sensor characteristics, signal acquisition settings, and ultimately the strength of the sensor's signal as measured by the receiver unit.

The well-established Frii's equation [64] is typically used to calculate the power delivered to a receiver from a transmitter taking into account factors such as wavelength of the EM wave used for communication (λ), distance between the transmitter and receiver (D_{TR}), gain of the transmitter antenna (G_T), and gain of the receiver antenna (G_R).

$$\frac{P_R}{P_T} = \frac{G_S G_T \lambda^2}{(4\pi)^2 D_{TR}^2} \tag{10}$$

Here, P_R is the power received by the receiver antenna and P_T is the power transmitted by the transmitter antenna. If we assume that receiver antenna in Equation (10) is the sensor's antenna, the power delivered to the resonator can be formulized as:

$$\frac{P_S}{P_T} = \frac{G_S G_T \lambda^2 L_M}{(4\pi)^2 D_{TS}^2} \tag{11}$$

Here, L_M is loss stemming from impedance mismatch between the resonators and antenna. It is assumed that losses stemming from the antenna itself (mismatch loss and ohmic loss) are taken into account in the antenna gain term (G_S).

Building on Equation (11), we can calculate the power of the sensor's response signal as measured by the receiver unit, taking into account sensor to receiver transmission, as:

$$\frac{P_R}{P_T} = \frac{G_R G_T G_S^2 \lambda^4 L_s}{(4\pi)^4 D_{RS}^2 D_{TS}^2} \tag{12}$$

Here, P_R and P_T are the power of the signal delivered to the receiver antenna and transmitted by the transmitter antenna, respectively. G_T and G_S are the gain of the

transmitter and sensor antenna, respectively. D_{TS} represents the transmitter-sensor

distance and D_{RS} is the distance between the sensor and receiver. λ is the EM wavelength

at the excitation signal frequency (assuming the frequency of excitation signal matches

either MEMS resonance mode) and L_s represents the total power lost in the sensor. Sources

of loss in the sensor include impedance mismatch between the resonator and antenna (as

described in detail in the previous section), Ohmic loss, dielectric loss, and losses

occurring in the MEMS resonator [65].

While Equation (12) takes into account all the sources of loss in the sensing system it

fails to consider that the ringdown nature of this sensor. Taking this into account we can

update Equation (12) as:

$$\frac{P_R}{P_T} = \frac{G_R G_T G_S^2 \lambda^4 L_s}{(4\pi)^4 D_{RS}^2 D_{TS}^2} \times \frac{(1 - e^{-T_w \omega / Q})}{T_w \omega / Q} \tag{13}$$

Here, T_w is the FFT time window, ω is the angular frequency of the MEMS resonance

mode, and Q is the effective quality factor at the receiver as measured by the ringdown

method. It's critical to understand that L_s is highly frequency dependent and minimum at

the resonance frequencies of the resonators. As a result, power received by the receiver for

any excitation signal frequency other than the resonance frequencies is effectively zero.

It should be noted that while theoretically increasing the transmitted power can

significantly improve measurement range, in practice transmitted power is often limited

by the RF front end (amplifier linearity and noise figure) and also concerns about patient safety from prolonged exposure to high power RF radiation. This highlights the importance of minimizing sources of energy loss in the sensor to maximize measurement distance. This equation is applied to the respiratory sensor in the following section and is utilized to calculate the actual total power loss in the sensor after all the different components are integrated.

3.7 Measurement Setup

The measurement setup used here is shown in Figure 25. The receiver and transmitter antennae are connected using SMA cables to a Rohde & Schwarz and RTO 1024 oscilloscope and SMC100A signal generator, respectively. The measurement system is only feasible through communication between the oscilloscope, signal generator, and a computer. This communication is enabled using LabVIEW installed on the computer and the communication itself is via ethernet connection on all 3 units and a trigger connection between the oscilloscope and signal generator through an SMA cable.
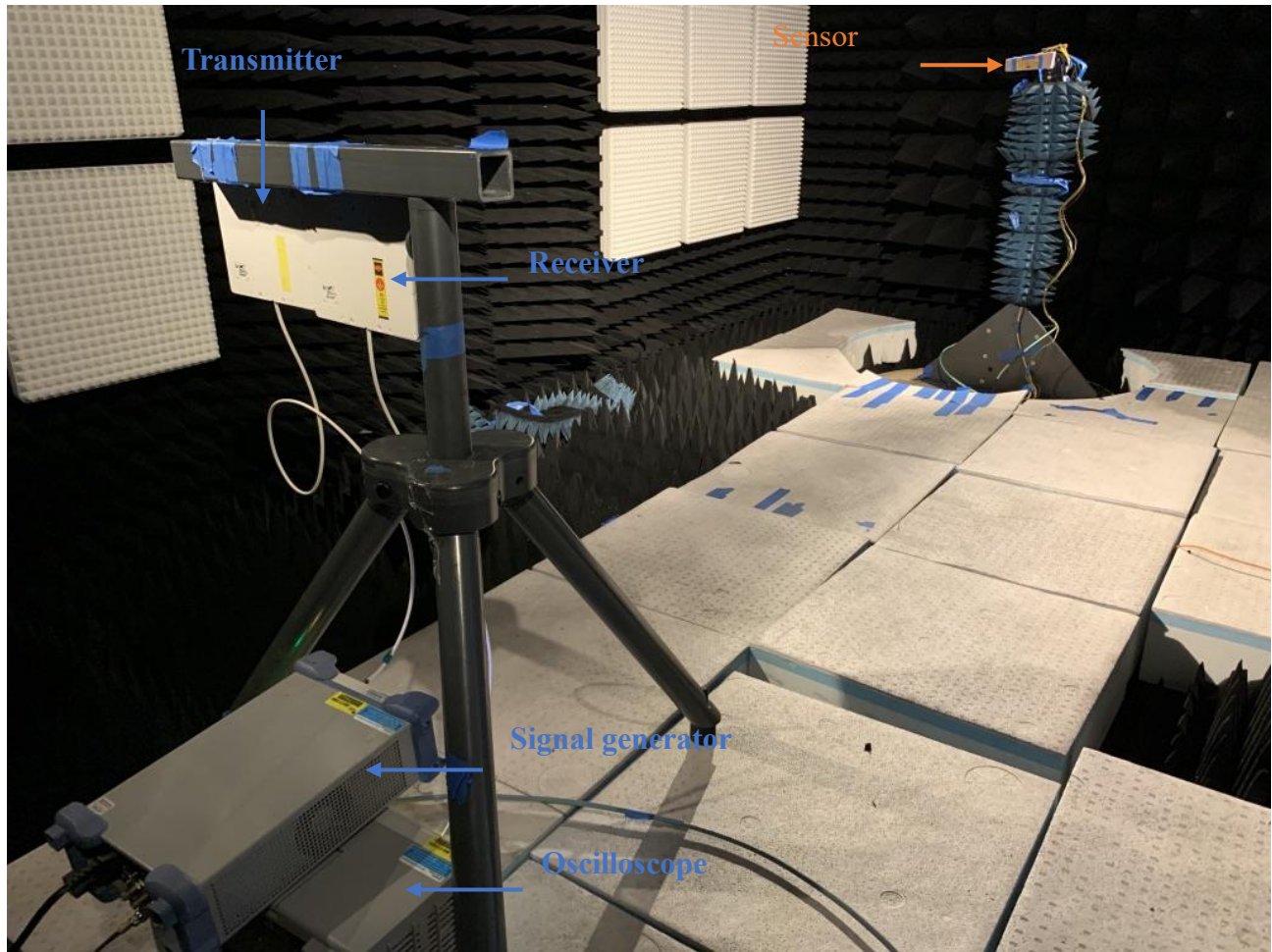
Figure 25. Anechoic chamber configuration for investigating power at the receiver end as a function of sensor distance. A PC outside the chamber controls both the signal generator and the oscilloscope using LabVIEW.

The overview of the measurement flow chart is illustrated in Figure 26. The processing of the measurement data including FFT, averaging, and visualization occurs in the computer and using LabVIEW. Any error between the frequency of the excitation signal and the resonance frequencies of the sensor results in a significant drop in power delivered to the sensor and lowering of the overall performance in terms of both SNR

and also maximum range. This can be largely attributed to the high quality factor of the MEMS resonators (and also overall sensor). As a result, a software based dynamic frequency locking mechanism is implemented. For this reason, in each measurement cycle the frequency of the excitation signal is updated to the moving average of the previous measured sensor resonance frequencies. It should be noted that this process is conducted separately for each of the resonance modes.
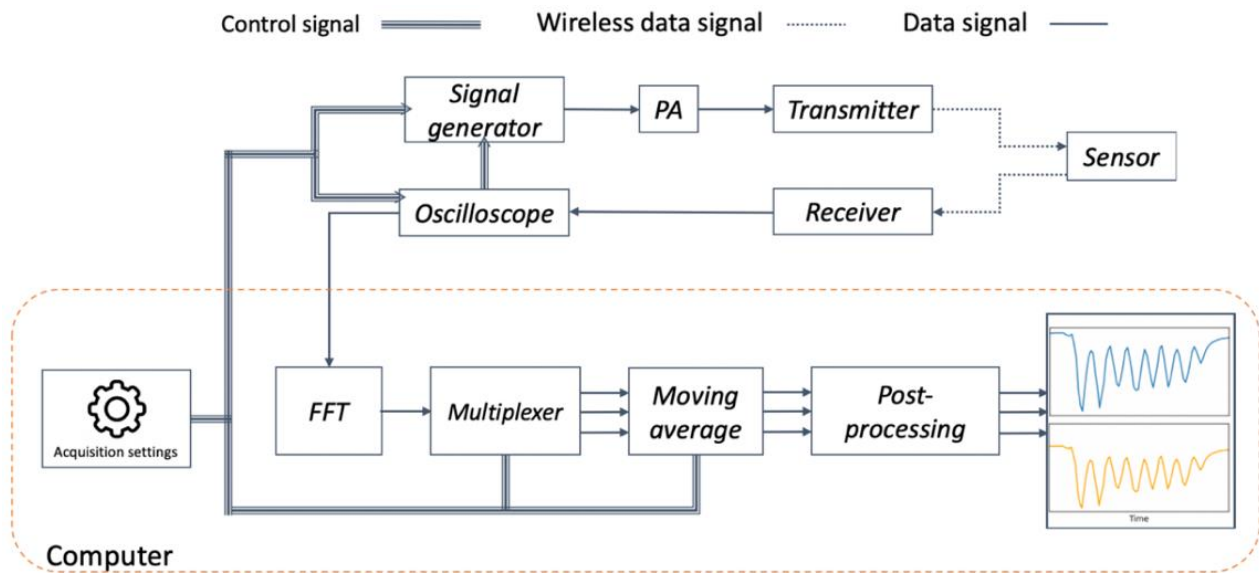
Figure 26. The major components/stages of the respiratory sensing system are illustrated in this signal acquisition flow map. The Power Amplifier (PA) is a completely optional function. The profile derived from the reference MEMS is not shown in the output in this case.

The LabVIEW front panel (the window that interfaces with the user) is shown Figure 27. Here, the user can enter their desired acquisition settings, set the TCPIP communication setting for the oscilloscope and signal generator, and visualize the

respiration profile as measured by each of the sensor's resonance modes, the raw FFT for

of the sensor's response, and also the time domain signal of the sensor's responses.

The acquisition settings including target frequencies, excitation signal power, duration of integration, averaging window, ADC dynamic range, ADC resolution, pulse width, start of acquisition time, FFT window type are all predefined as settings in the LabVIEW interface.

In sensing applications, typically the size of the moving average window is determined as a compromise between responsiveness and SNR, however in this case given that slow response to shifts in resonance frequency results in lower SNR a small window is preferred. A moving average with a larger window is applied in the post-processing step. The window size for the tracking system and post-processing step was 2 and 8, respectively.

Time resolution (sampling rate) of the respiratory profile determines how faithfully the patient's respiration is reconstructed and is a critical parameter as it sets the maximum detectable feature frequency through the Nyquist–Shannon sampling theorem. Given that the typical respiratory cycle of an adult human lasts ~4s our measurement system's time resolution of ~130ms fulfills the Nyquist frequency condition and can theoretically resolve features up to ~3.85Hz. It should be noted that in our measurement system the transfer of signals acquired by the oscilloscope to the PC and their processing by LabVIEW is the determining factor for time resolution.
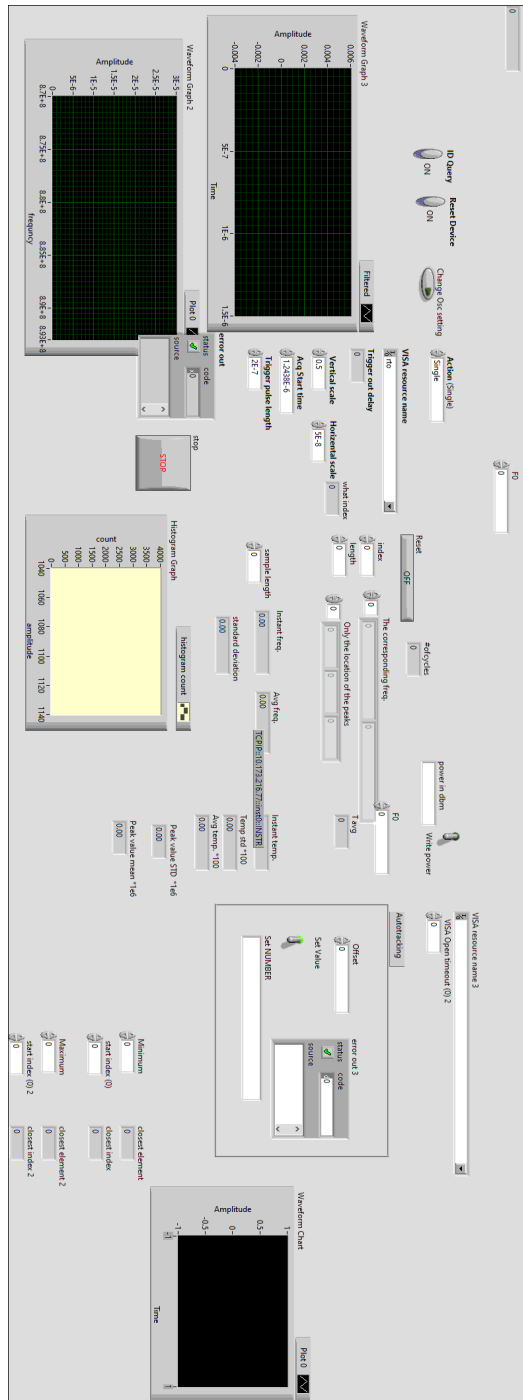
Figure 27 Front panel of the LabVIEW software. The interface includes insets for entering the TCPIP addresses for the oscilloscope and signal generator, acquisition setting, multiple graphs for plotting the respiration profile as calculated by each of the resonators, and a histogram to enable the calculation of the SNR of the sensor.

Set acquisition setting

Calculate FFT
spectrum and plot it

Calculate max(FFT)

Calculate moving
Average, plot
histogram, and
waveform

Set the frequency and power
of signal generator
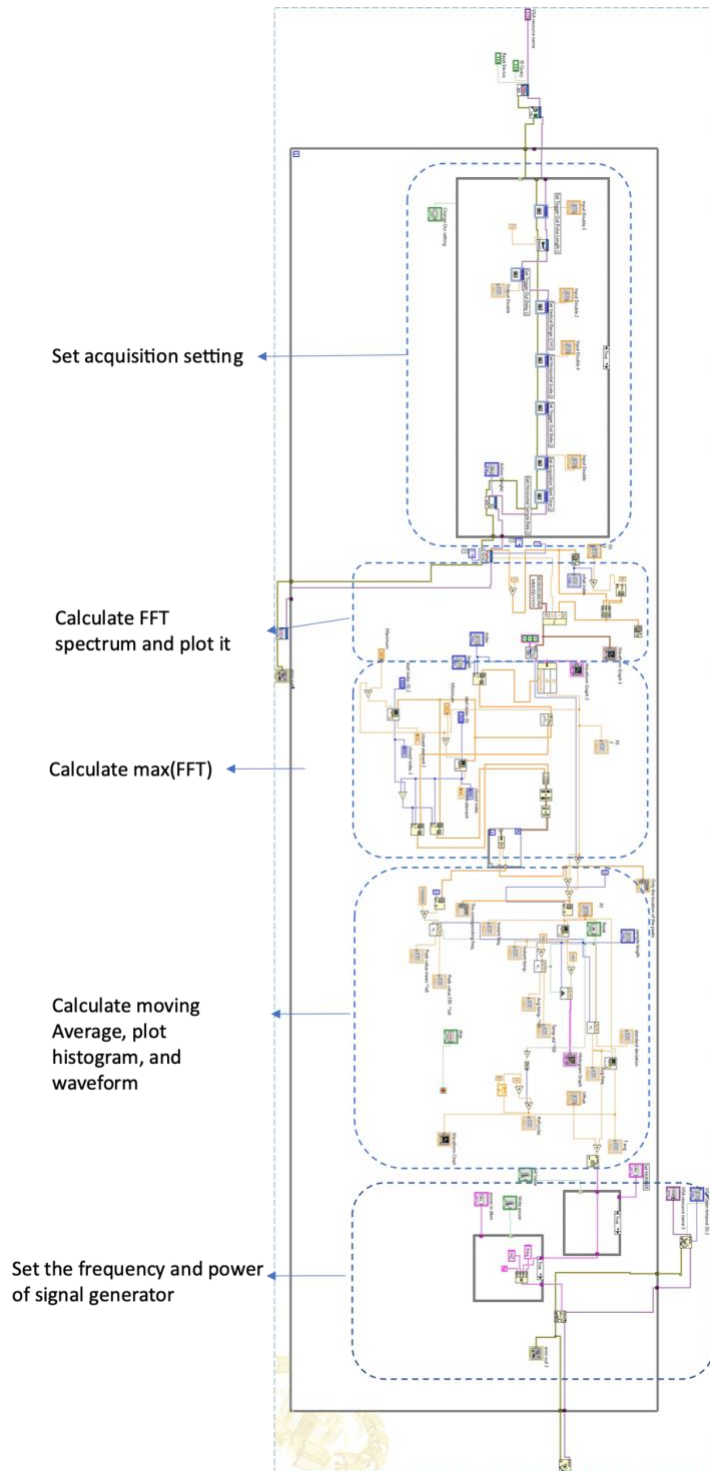
Figure 28 Block diagram of the LabVIEW file used for the respiratory monitoring system. The acquisition starts from the top by setting the TCPIP setting of the oscilloscope and ends at the bottom by updating the frequency of the excitation signal.

3.8 Results & Discussion

Multiple MEMS resonators were used in the sensor to distinguish between the effects of respiratory flow and environmental variations on the sensor. The two main causes of environmental variability analyzed in this research are: 1) separating changes stemming from respiratory flow from changes in environmental temperature and, 2) removing motional artifacts caused by minor variations in antenna loading as a result of electromagnetic environmental loading changing.

Since MEMS resonance frequency is a function of temperature, any sudden change in ambient temperature can be misclassified as a respiratory incident. As a result, we tried to eliminate frequency modulation caused by ambient temperature changes from the respiratory profile by adding two MEMS devices with identical TCF (as shown in figure 22). In summary, we attempted to differentiate temperature-induced frequency shift from mass loading frequency shift.

By blowing hot air over the sensor and measuring the frequency shift, the efficacy of this decoupling process was investigated experimentally. The aim of this experiment is to simulate a rapid change in ambient temperature in the absence of any substantial mass loading. The frequency shift exhibited by the 879.9MHz and 888MHz modes, as shown in Figure 29, is inconsistent with the decoupling mechanism's assumption of equivalent MEMS resonator temperature. We believe that this temperature gradient is due in part to unequal heat transfer caused by unregulated airflow at the sensor's surface.
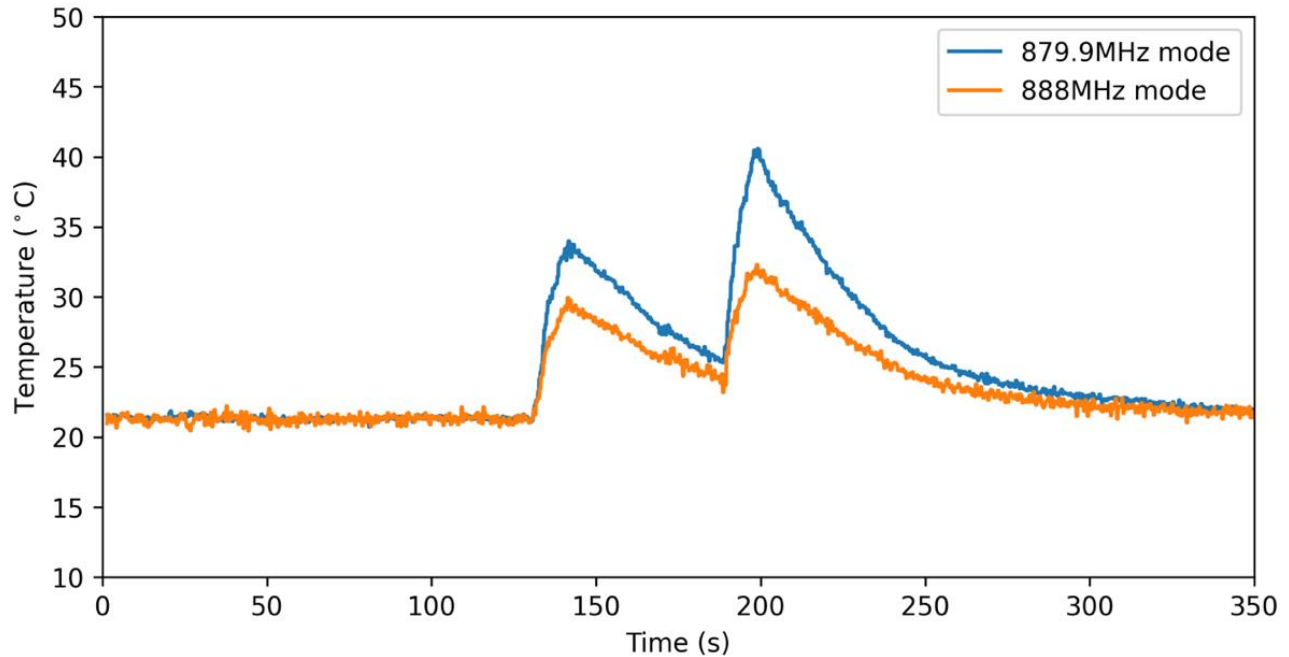
Figure 29. Temperature shifts were measured for the 879.9MHz and 888MHz modes in response to two different heating cycles. The temperatures of the resonators (each corresponding to an individual mode) were identical before the first heating event and the temperatures of the modes converged after the second cool-down cycle.

Depending on the electromagnetic loading from its surroundings, the RFID antenna has a slightly different impedance profile. Four independent 90° rotations of the sensor were used to measure the effect of sensor orientation on the excitation and receiver antennas. The objectives of this study were to replicate patient's body rotation. In an anechoic chamber, measurements were made for peak and mean power of 80mW and 80μW at 50cm. Figure 30 shows how sensor orientation has a noticeable effect on the frequency associated with both modes as seen by the receiver antenna.
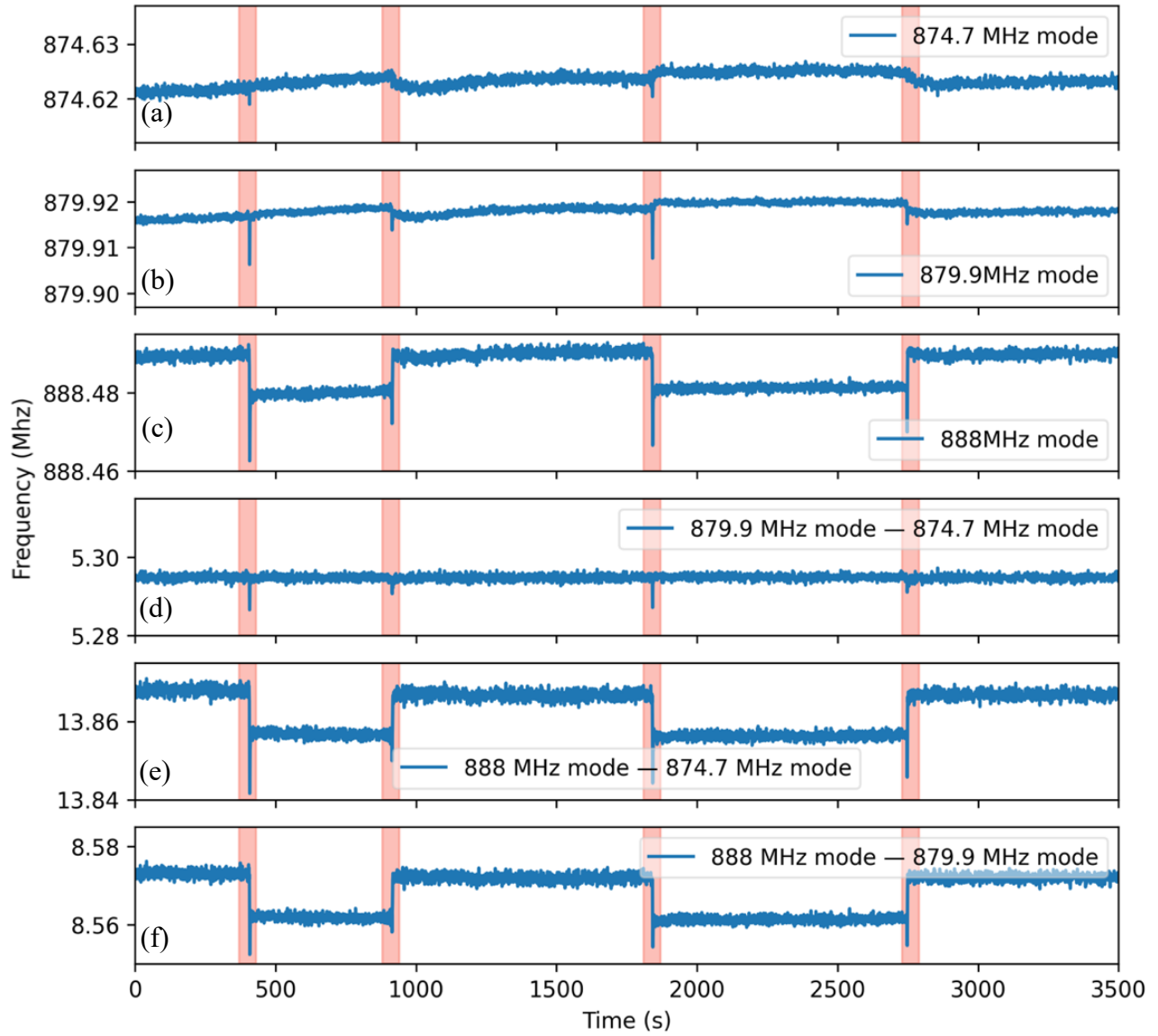
Figure 30. (a)-(c) Measured frequency corresponding to each of the sensor's 3 resonance modes at 50cm distance and peak and mean power of 80mW and 80μW, respectively. The sensor was rotated by 90° (highlighted in red) to simulate the sudden rotation of the patient's body. (d) For the 874.7MHz and 879.9MHz modes, this frequency shift can be canceled by subtracting the 879.9MHz and 874.7MHz modes whilst the same compensation method was found to be ineffective between 888MHz and 879.9MHz (e), 888MHz, and 874.7MHz (f).

The sensing system will identify the movement of a patient's head as a respiration event if there was no compensation mechanism in place. However, as shown in Figure 30, we can effectively distinguish changes in frequency associated with motion-induced objects by tracking the difference between the frequencies of the two modes. It should be noted that no similar compensation mechanism was found between either of MEMS#1's two resonance modes (874.6MHz and 879.9MHz) and MEMS#2 (888MHz). The experimenter's hand physically handled the sensor, causing a spike-like drop in frequencies.

Based on the results of the two experiments, we concluded that, although the sensor can remove motion-induced artifacts. Separating rapid changes in ambient temperature from respiratory flow without using a software-based solution is unlikely in its current form. As a result, in the following measurement results, the 888MHz resonance mode was not monitored.

The respiratory profile of a healthy adult was calculated using the measurement setup mentioned above, with a mean transmitted power of 80μW and a peak transmitted power of 80mW. Figure 32 depicts the sensor's response as seen by the receiver antenna.
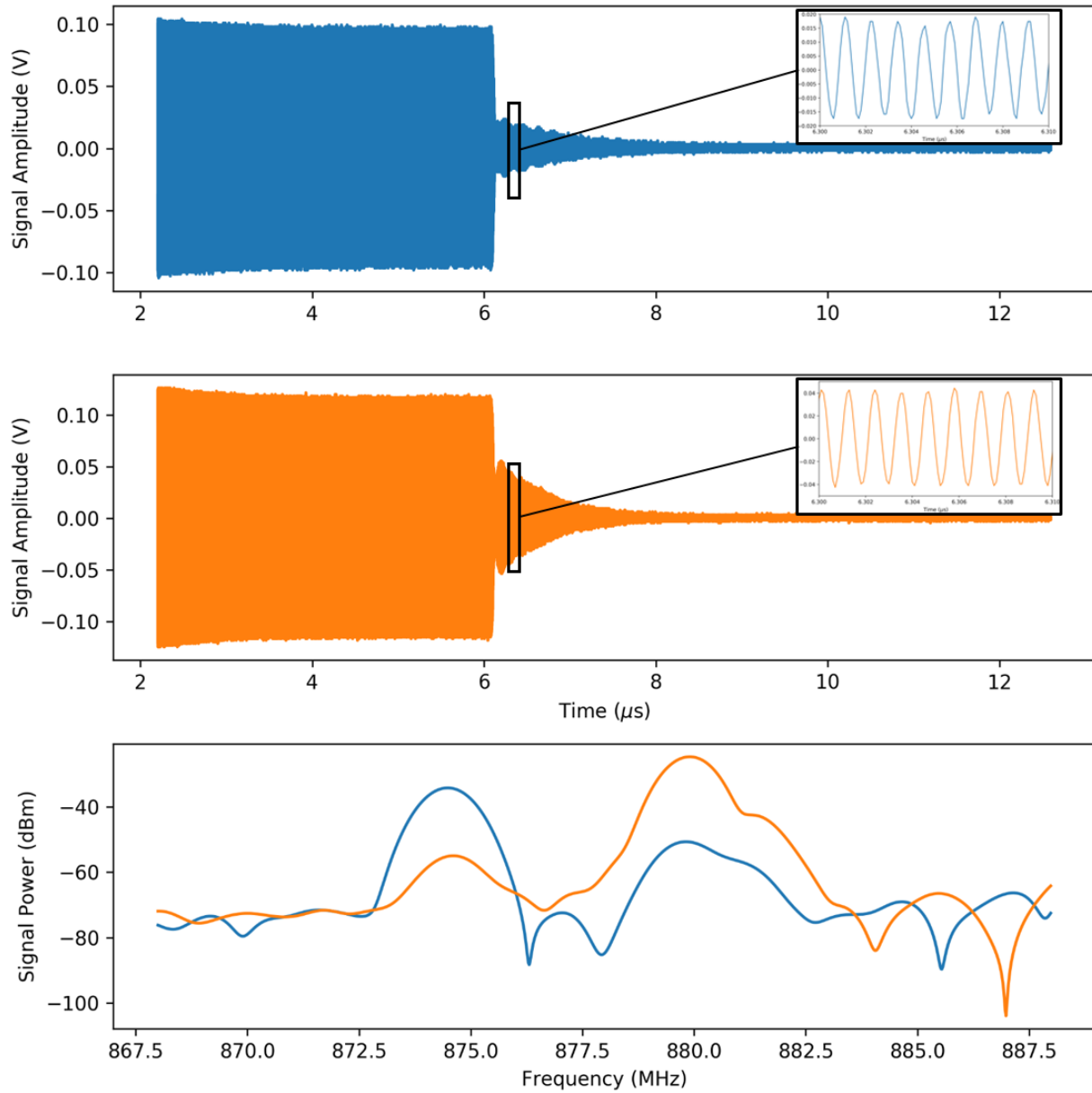
Figure 31. Excitation signal and sensor response as measured by receiving antenna for the 874.7MHz (top) and 879.7MHz (middle) modes. The FFT of the two signals are superimposed and shown in the bottom panel.

The sensor has reported three distinct respiratory patterns, as shown in Figure 32: abnormal, uniform-normal, and shallow, each of which is interrupted by a brief time when

the patient stopped breathing. Patients with sleep apnea often exhibit this pattern of brief interruption of breathing.
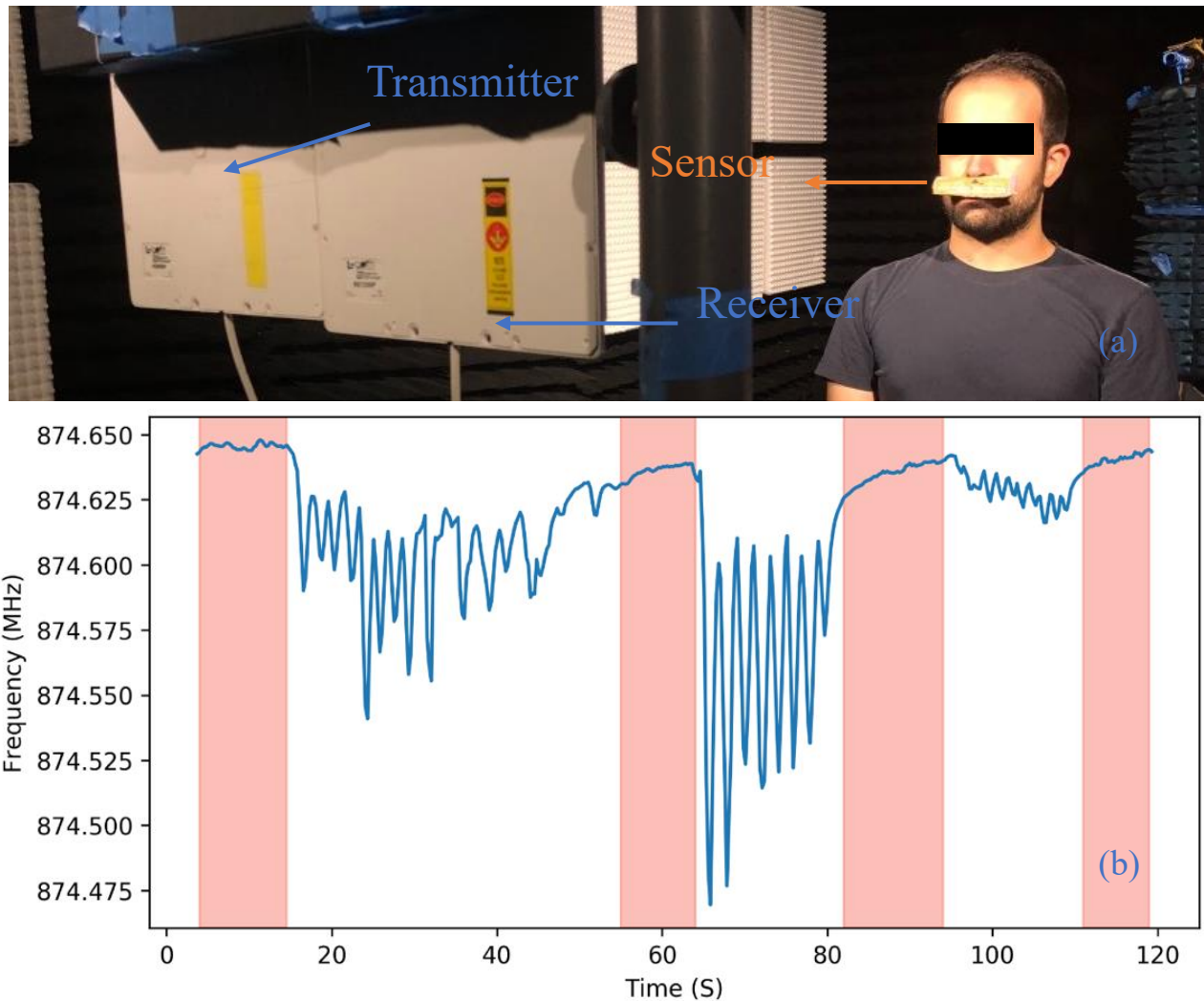
Figure 32. (a) Human respiratory measurement illustrating the sensor placed on the patient's upper lip region (b) Respiratory profile of human subject demonstrating non-uniform, uniform moderate, and shallow respiration in that order. Each drop in the frequency and subsequent recovery constitutes a single exhalation and inhalation event. Periods in which the patient ceased to breathe are highlighted in red.

The sensor's response was measured as a function of distance from the base unit in the 874.7 MHz and 879.9 MHz modes, with a peak and mean transmitted power of 80mW and 80μW, respectively. We can use the modified Frii's equation (Equation 12) for sensor, transmitter, and receiver antenna gains of 1.4dBi, 8dBi, and 8dBi, respectively, to estimate signal intensity as a function of sensor distance if we know the sensor's output for a given input power. Figure 33 depicts the simulated and measured signal power.

The cumulative effective loss of the sensor for the 874.7 MHz and 879.9 MHz modes was found to be 15dB and 13.4dB, respectively, by fitting Equation (12 to the measured power at the receiver. The gap between these values and the simulation results in Table 1 can be attributed to differences in HFSS antenna simulation and fabricated antenna, wire-bond inductance, and MEMS resonator degradation due to aging effects.
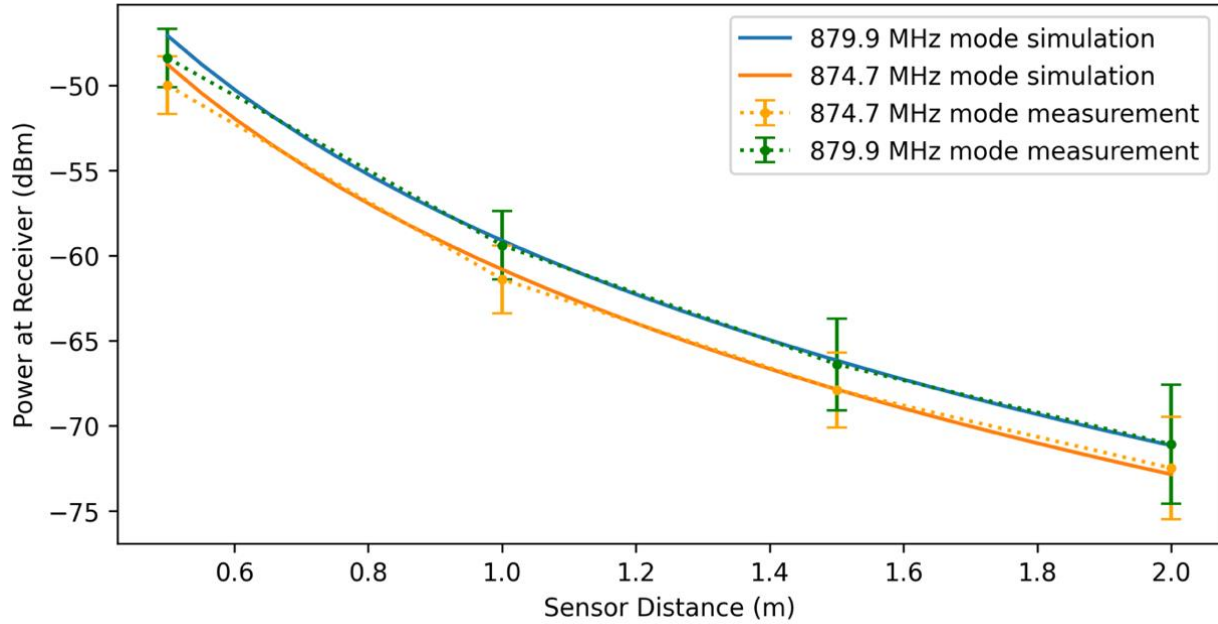
Figure 33. Signal power at receiver for peak transmitter power of 19dBm. The difference in measured and simulated values can be largely attributed to the impact of the directionality of the transmitter and receiver antennae at 50cm.

In an anechoic chamber, the accuracy of the sensing device was assessed by measuring the measurement variance over a long period of time (~45 minutes) at a distance of 0.5 meters from the receiver and excitation antenna. The peak and mean transmitted power were 80mW and 80μW, respectively, as in the previous experiment. Frequency drift due to temperature variations in the environment was eliminated in post-processing after measurement. The standard deviation was measured as 503 Hz by plotting the measurement's histogram and fitting it to a normal distribution (Figure 34). We can calculate the $SNR = \mu/\sigma$ to be 124.8dB .
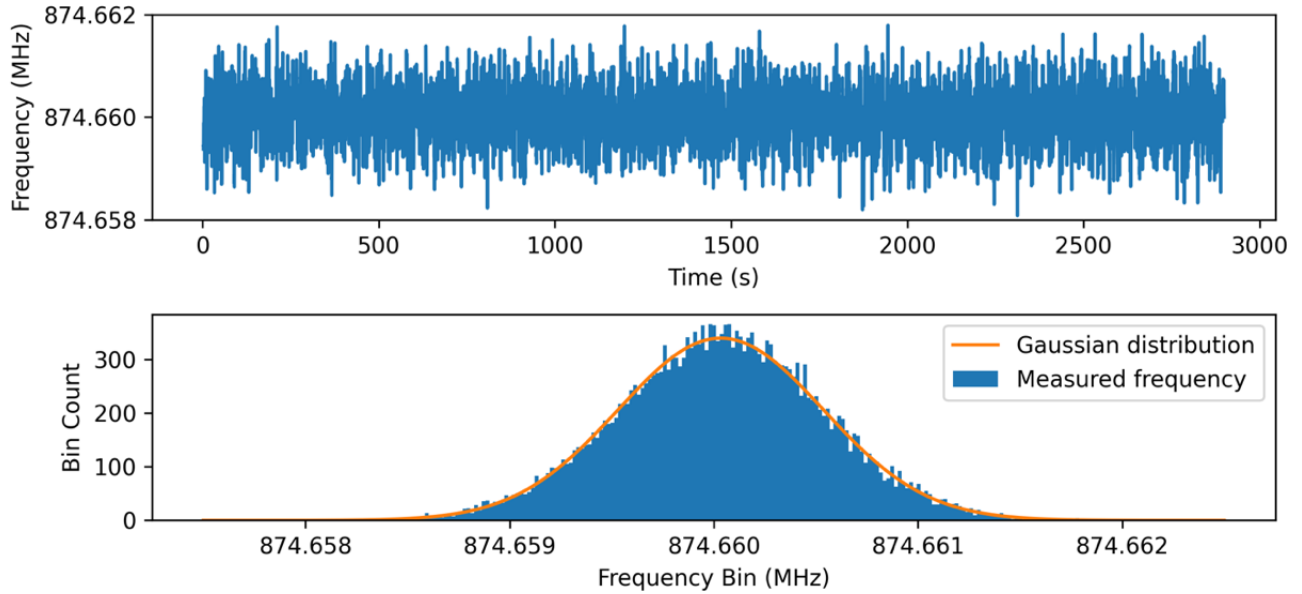
Figure 34. (top) Sensor measurement for 45 minutes for peak transmitted power of 80mW and mean transmitted power of 80μW. (bottom) Histogram of sensor response fitted with Gaussian distribution with a standard deviation of ~503Hz. Each count corresponds to a single measured response.

3.9. Conclusion

A passive wireless respiratory sensing system based on frequency modulation of TPoS MEMS resonator was developed. With a size of only ~10cm², the sensor was capable of measuring respiratory profile from up to a distance of 2 meters from the transceiver unit for mean transmitted power of 80μW and peak transmitted power of 80mW. The SNR was measured to be 124.8dB at a 50cm sensor distance with the same transmitted power.

The respiratory sensor is made up of an antenna wire-bonded to two low-loss piezoelectric MEMS resonators, which is excited by a transmitter antenna and registered

68

by a receiver antenna. We show that an increase in temperature and mass loading from surface vapor condensation caused by exhaled airflow causes a major and reversible decrease in MEMS resonance frequencies. The shift in MEMS resonance frequencies is then extracted using FFT analysis and plotted over time to create the patient's respiratory profile.

A custom RFID antenna was built to achieve optimal impedance matching with the two MEMS resonators despite their considerable difference in impedance at their respective resonance modes to reduce energy lost due to impedance mismatch between the MEMS resonators and sensor antenna.

The Friis equation, which is commonly used to measure the maximum operating distance for wireless passive devices, is insufficient for ringdown type sensors, as we demonstrated. A modified version of the equation was provided that took into account the FFT window and sensor quality factor and was used to calculate the sensor's effective loss in various operating modes.

The sensor was shown to be capable of separating shallow and abnormal breathing from normal breathing, as well as detecting breathing cessation events, which is critical for sleep apnea research.

The sensor response is cancelled using a novel approach that cancels the effect of motion-induced artifacts and drift. We can detect frequency changes caused by antenna

position changes by integrating a MEMS resonator with two modes near the frequency of

interest and monitoring the difference between their resonance frequencies.

CHAPTER FOUR: RF MEMS–BASED PASSIVE WIRELESS RESPIRATORY FLOW RATE SENSOR

Respiration monitoring beyond respiration rate and profile can only be measured using flow sensors. In this chapter, following an introduction on the state-of-the art of respiratory flow sensing, we will detail how the developments explained in the previous chapters enabled the creation of the first RF MEMS-based passive wireless flow rate sensor. [2]

Existing sensors used for respiratory flow monitoring can be categorized according to their underlying physical sensing principle [9], [17]:

Differential flowmeter: Differential flow meters are widely used to measure airflow in mechanical ventilators and spirometers [66], [15]. As shown in figure 5.1 this type of flow sensors functions by incorporation of a known pneumatic resistance in the flow pathway and monitoring of the resulting pressure drop (ΔP) for a given flow (Q) using a differential pressure sensor. Differential flowmeters can be divided into Pneumotachographs, which utilizes either a capillary [67] or mesh [68] to create flow resistance and Orifice meters which utilize an orifice plate [69] to create resistance to gas flow. Sensitivity of differential flowmeters are in part set by the flow resistivity with a

---

higher resistance resulting in a lower sensitivity but higher dynamic range. By setting

this parameter is it possible to design flow sensor that either suitable for adults or infants.

An additional advantage of differential flowmeters is that their capability to detect

direction of airflow and therefore distinguish between inhalation and exhalation. A

drawback of these sensors is the need for the patient to wear a mask, which represents a

significant challenge for critically ill patients [7].

As an accurate flow sensor, differential flowmeters are used to measure the temporal

trends of respiration including qualifying other flow sensors for respiratory monitoring

applications [70].
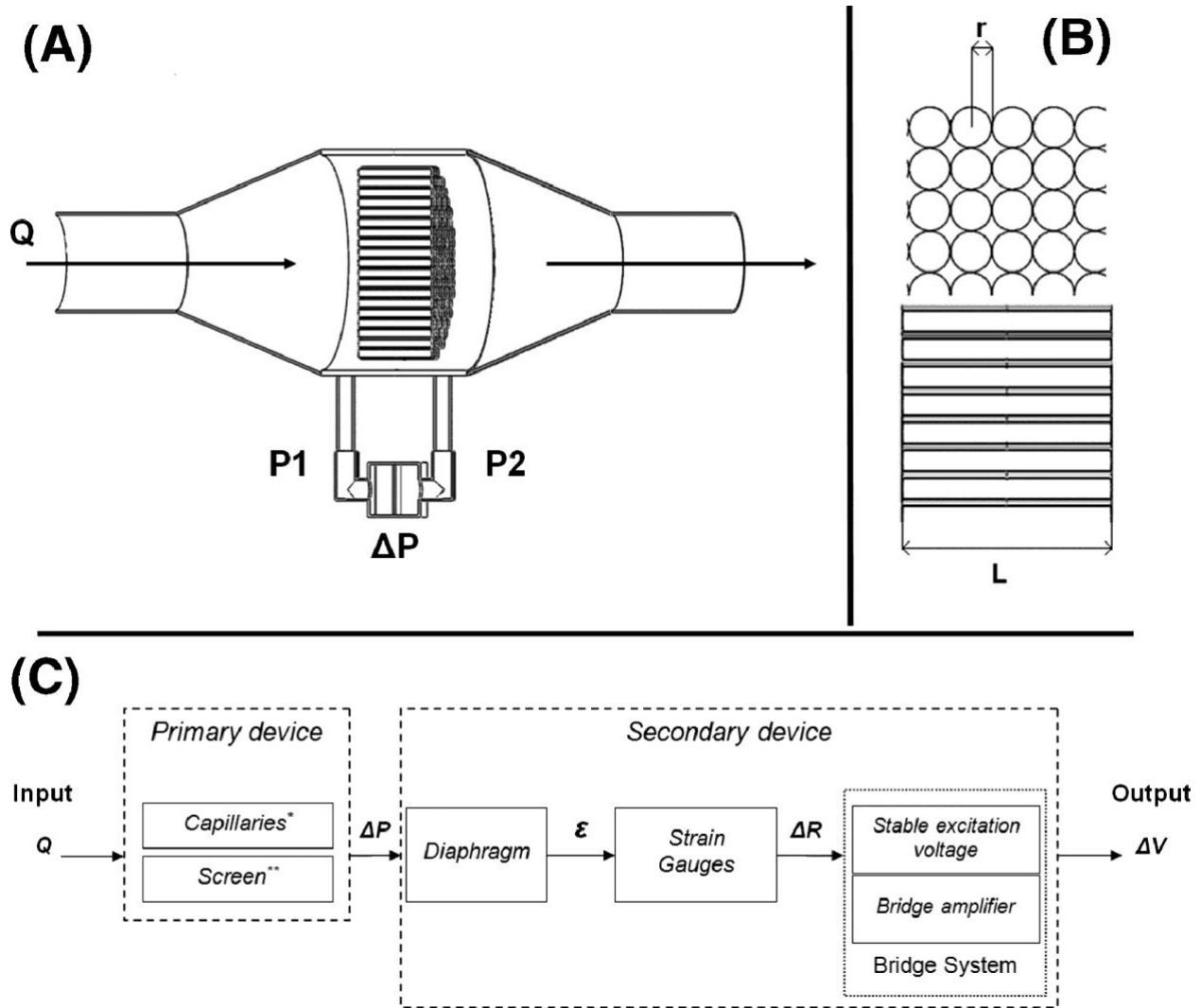
Figure 35. Fleisch pneumotachograph [67] produces a differential pressure drop (ΔP) across two capillaries that is linearly related to gas flow (Q) [15].
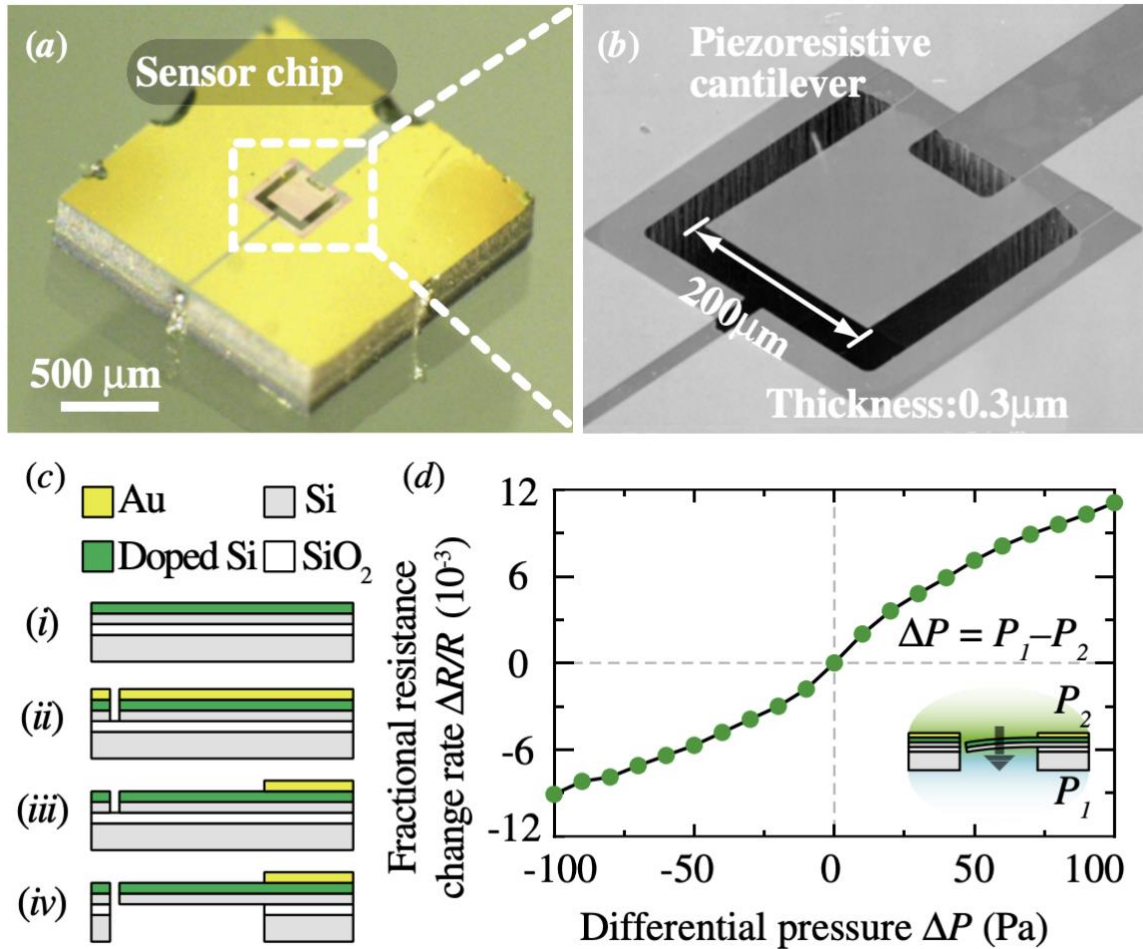
Figure 36. This pressure differential can be accurately measured using a modern MEMS pressure sensor. (B) An example of such a device, this MEMS sensor utilizes the piezoresistive property of doped Silicon measure the pressure induced displacement in the cantilever bream [31].

1- Turbine flowmeter: Fundamentally, turbine flowmeters operate by converting kinetic energy of the gas or liquid molecules flowing through the sensor into rotational kinetic energy of a miniature turbine. Although the most general form of a turbine flowmeter's governing equation does not promote a linear relationship between flow (Q) and

rotational velocity (*nrev*), by carefully designing the sensor's geometry as it relates to gas

or liquid's Reynold's number a linear profile is achievable:

$$Q = k \cdot nrev \qquad (14)$$

Turbine flowmeters have the added benefit of operation independent of gas/liquid

viscosity and temperature [71].
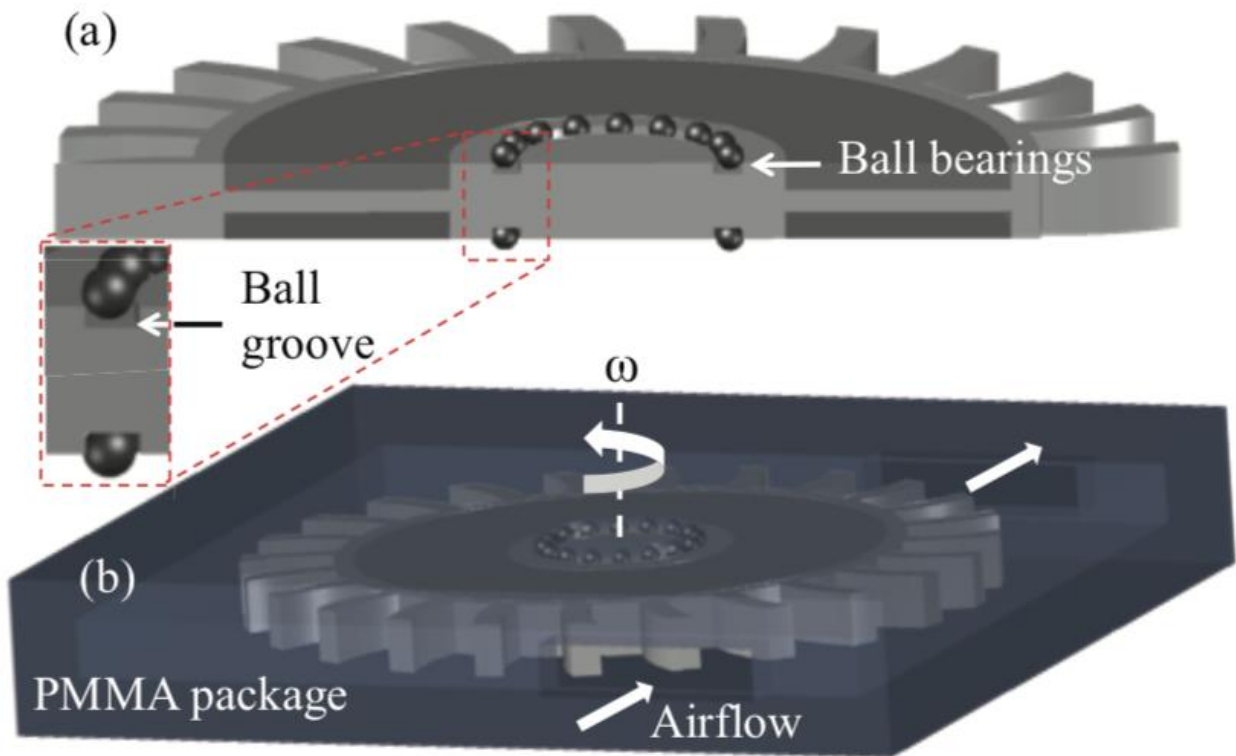
Figure 37. MEMS turbine designed to harvest energy from human respiratory flow [72]. The small footprint and simple design of the device makes it a competitive candidate for flow sensing applications.

2- Hot-wire and hot-film anemometer: operates based on principle of heat exchange between a heated element and gas/liquid flow. A higher flow rate results in a higher levels of heat transfer. Following calibration, by monitoring the temperature of the heated element it is possible to calculate air flow [16]. Given their propensity for miniaturization, hot-wire anemometer and similar thermal flow sensors are some of the most widely used sensors for wearable sensors [9], [17]. An overview of the operation of this sensor is shown in the figure below. As gas flow from inlet on the left it displaces warmer air molecules around the left temperature sensor resulting in a drop in temperature for that sensor. Inversely, gas flow from left to right results in a increase in temperature measured by the right temperature sensor.
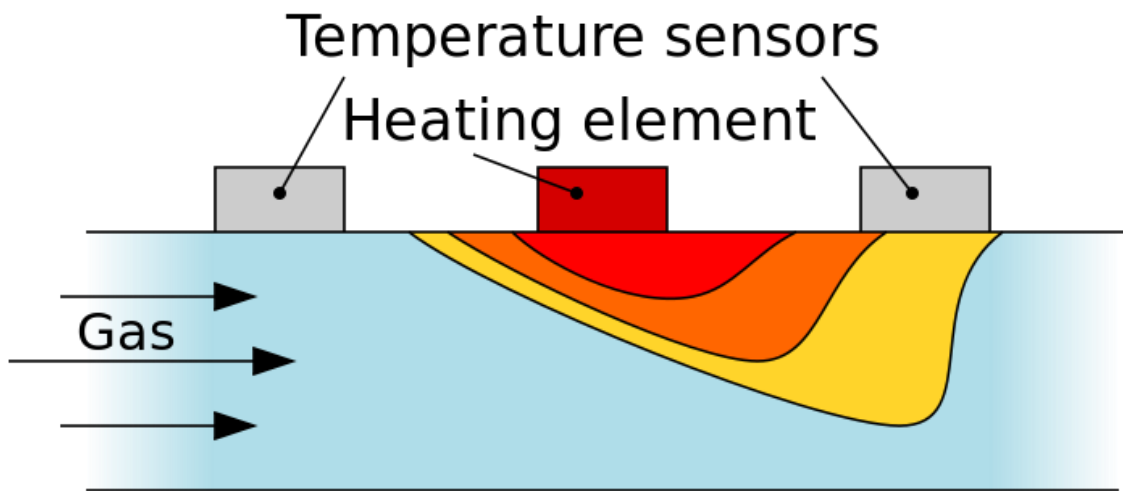
Figure 38. Schematic of bi-directional flow sensor composed of a heating element and two temperature sensors [73].

Fiber optic flow meter operates based on frequency or amplitude modulation of light passing through a fiber optical waveguide by exposure to respiration. In [74] the waveguide is covered by a humidity sensitivity coating that expands and contracts throughout the respiration cycle. The change in mechanical strain applied to the fiber optical waveguide results in a corresponding change in frequency of the optical signal. By calibrating the frequency shift using a standard flow meter, the authors created an inexpensive and highly sensitive flow meter.
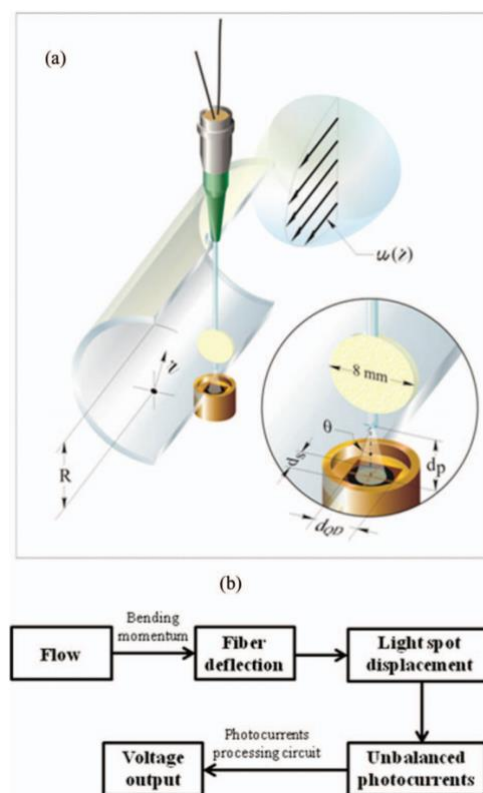
Figure 39. Overview of an optical flow sensor that utilizes displacement of the fiber caused by airflow to measure the flow. (a) The displacement is detected by a photodiode located under the fiber optic tip. (b) The schematic illustration of the flow to voltage transduction process [75].

Time-of-flight sensors: operate by monitoring the delay in the propagation of a transmitted wave through the target medium caused by flow. This type of flow sensor can be further categorized according to the wave that is used to measure flow into thermal [76], ultrasonic [77], and optical [78]. In [76] a heating-sensing pair of resistors are fabricated along a microfluidic channel. The heating resistor generates a heat pulse that is subsequently carried by the flowing liquid towards the sensing resistor. The heat wave's time-of-flight is then detected as a change in resistance of the sensing resistor and subsequently converted into flow rate. By knowing the cross-section area of the micro-channel, the authors were able to calculate the flow through the sensor.
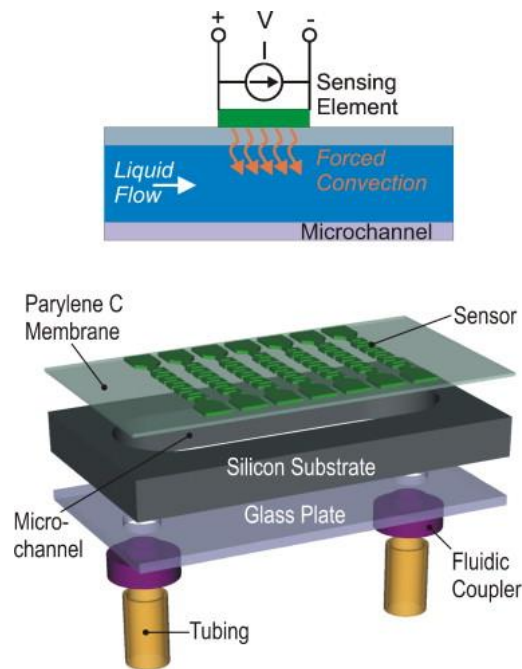
Figure 40. 3D rendering and cross sectional depiction of liquid-phase hot film flow sensor [76]. For this sensor to functional as a time-of-flight sensor a secondary sensor should be incorporated.
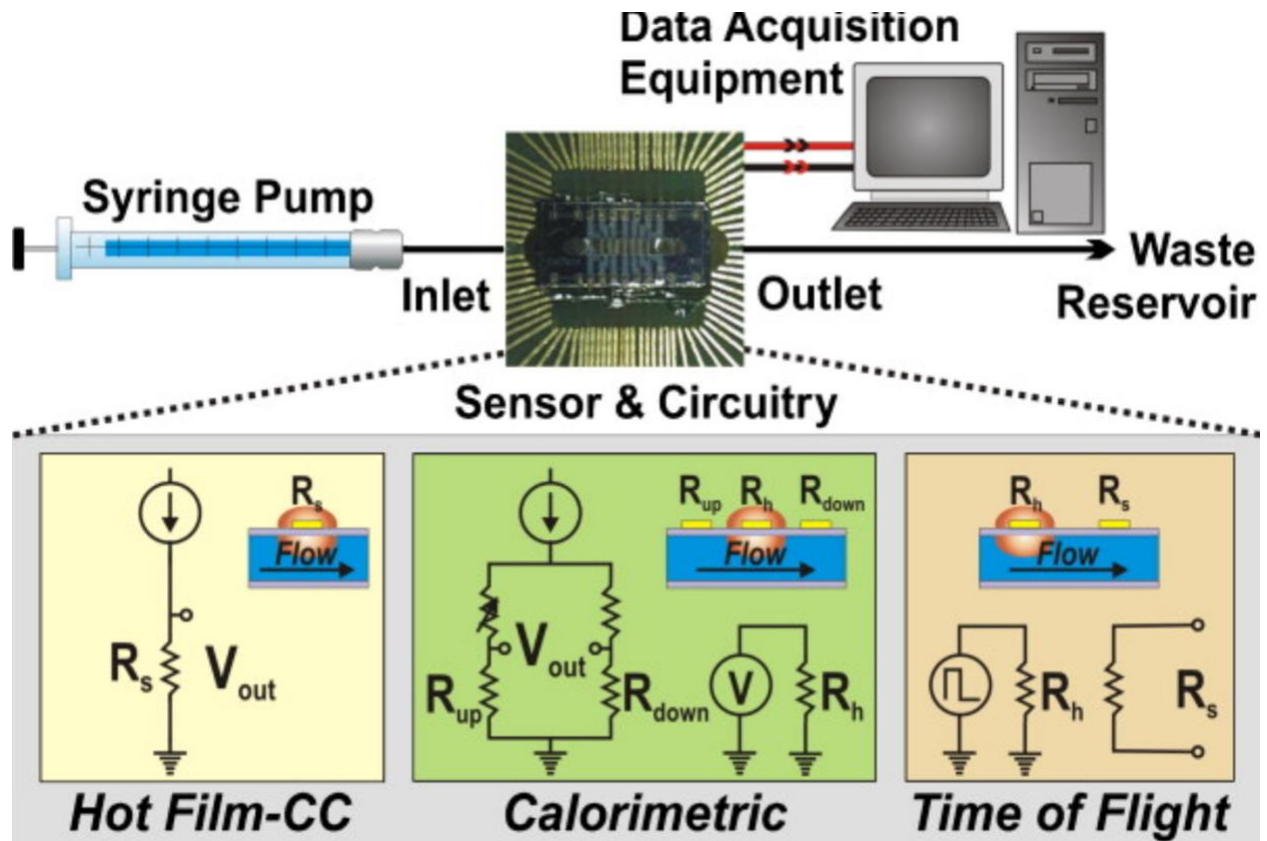
Figure 41. Schematic of flow sensor and it's circuitry for 3 different modes of operations (hot film, calorimetric, and time-of-flight). The time-of-flight operation is based on the amount of time it takes for the heat pulse generated by the heater resister to be sensed by the sensing resistor [76].

Recently the author of this thesis introduced a new category of time-of-flight flow sensor that utilizes RF-MEMS resonators to measure flow rate [55]. The remainder of this chapter details this work and the advantages and disadvantages of this category of sensor.

The large number of different categories and sub-categories of flow sensors available for respiratory monitoring present a challenge for selecting the correct type of sensor for a given application and optimizing the associated trad-offs. The following table was

adapted from [9], [16], [17] with the goal of providing the reader with a tool for quick evaluation of the advantage and disadvantages presented by different categories of flow sensors. This table is only designed for respiratory monitoring applications.

4.1 Passive Wireless RF MEMS Time-of-flight Respiratory Flow Rate Sensor

The need of portable, low cost and, practical respiratory monitoring systems motivated us to develop a wireless MEMS-based respiratory sensor. The sensor is designed to measure the respiratory rate without connecting to a power source and sensor front end. It is important to recall that this sensor has been specifically designed for wireless applications, but it is fully functional in a wired configuration.

As depicted in Figure 42 the sensor is consisted of a commercial planar grounded antenna, two high Q, low loss MEMS resonators, located with a distance of ~1cm away from each other.
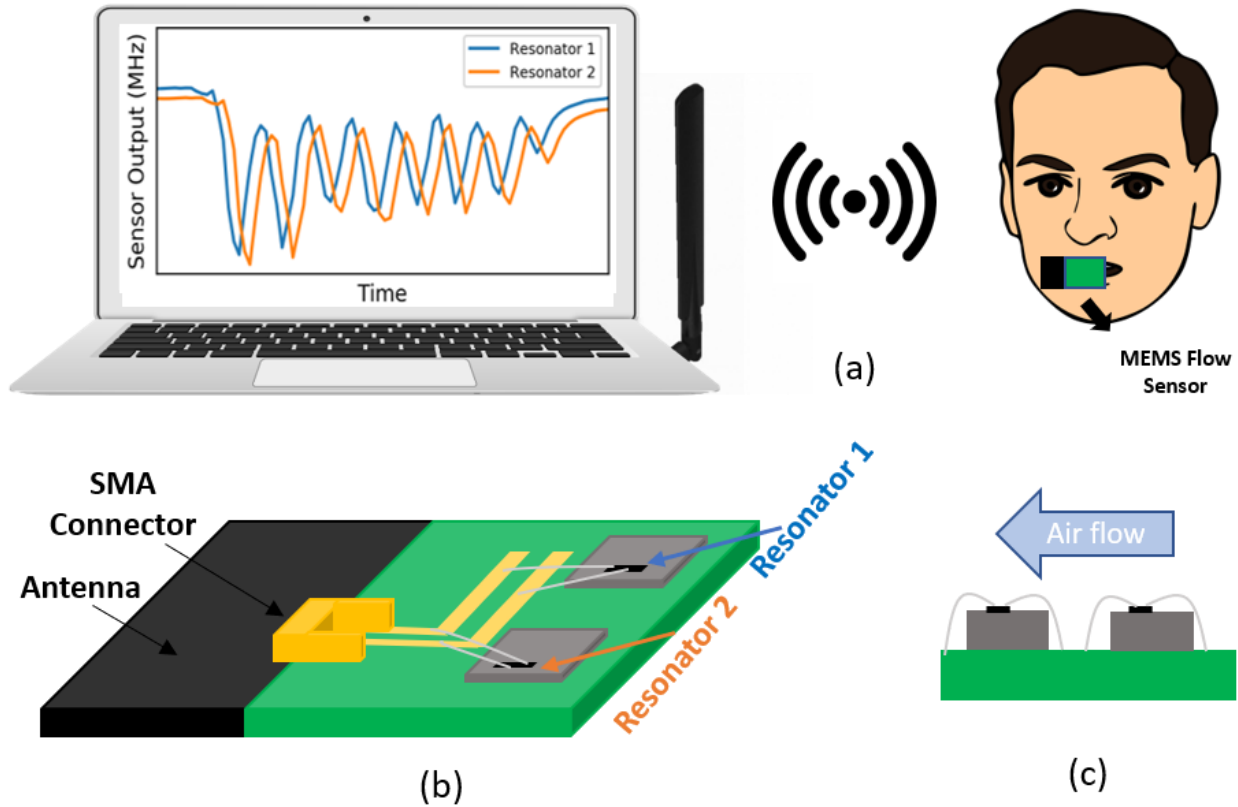
Figure 43. (a) Schematic of a respiratory flow rate established using time-of-flight sensing configuration. A signal generator (not pictured) connected to an external antenna generates a pulse modulated sinusoidal signal to communicate with the sensor's antenna. The sensor transmitted a response which could be monitored to plot the natural resonance frequencies of this excited sensor over time. (b) The sensor is composed of two low loss, high Q MEMS resonators connected in parallel electrically to a commercial chip antenna. (c) illustration of sensor super imposed with schematic respiratory airflow [55].

4.2 Sensor Design

Two thin-film piezoelectric-on substrate (TPoS) MEMS resonators operating near the ISM band (898.5MHz and 906MHz) connected to a grounded line commercial planar antenna is the makeup of the designed sensor. High quality factor and low insertion loss

make the TPoS MEMS resonators suitable for sensor applications. The operation mode of the MEMS resonators is bulk lateral extensional. In these resonators a thin layer of Aluminum-Nitride is sandwiched in between two Molybdenum layers stacked on a top of low loss nanocrystalline diamond substrate layer. An ANT-916-SP grounded line planar antenna was employed in the sensor. Surprisingly, despite the small footprint the antenna exhibits excellent performance in proximity to human body.

The excitation of the resonators on the sensor is through an antenna using a pulsed sinusoidal signal that periodically targets the resonance frequency of each of the two resonators at <10ms intervals. To extract the resonance frequency of the resonators from the reflected power, Fast Fourier Transform (FFT) is utilized. The temperature and moisture content of inhaled and exhaled air is different from ambient air and will result in resonance frequency modulation of MEMS resonators. A frequency shift results from passage of hot and humid exhaled air over the resonators, due to spatial distance between them a delay in frequency shift observed. The delay time is used to calculate air flow rate.

Additionally, by tracking the resonance frequency of the sensor over time, the respiration profile could be developed. As shown in Figure 43 and Figure 44 the MEMS devices are integrated in a single port configuration and are electrically connected in parallel to the antenna.
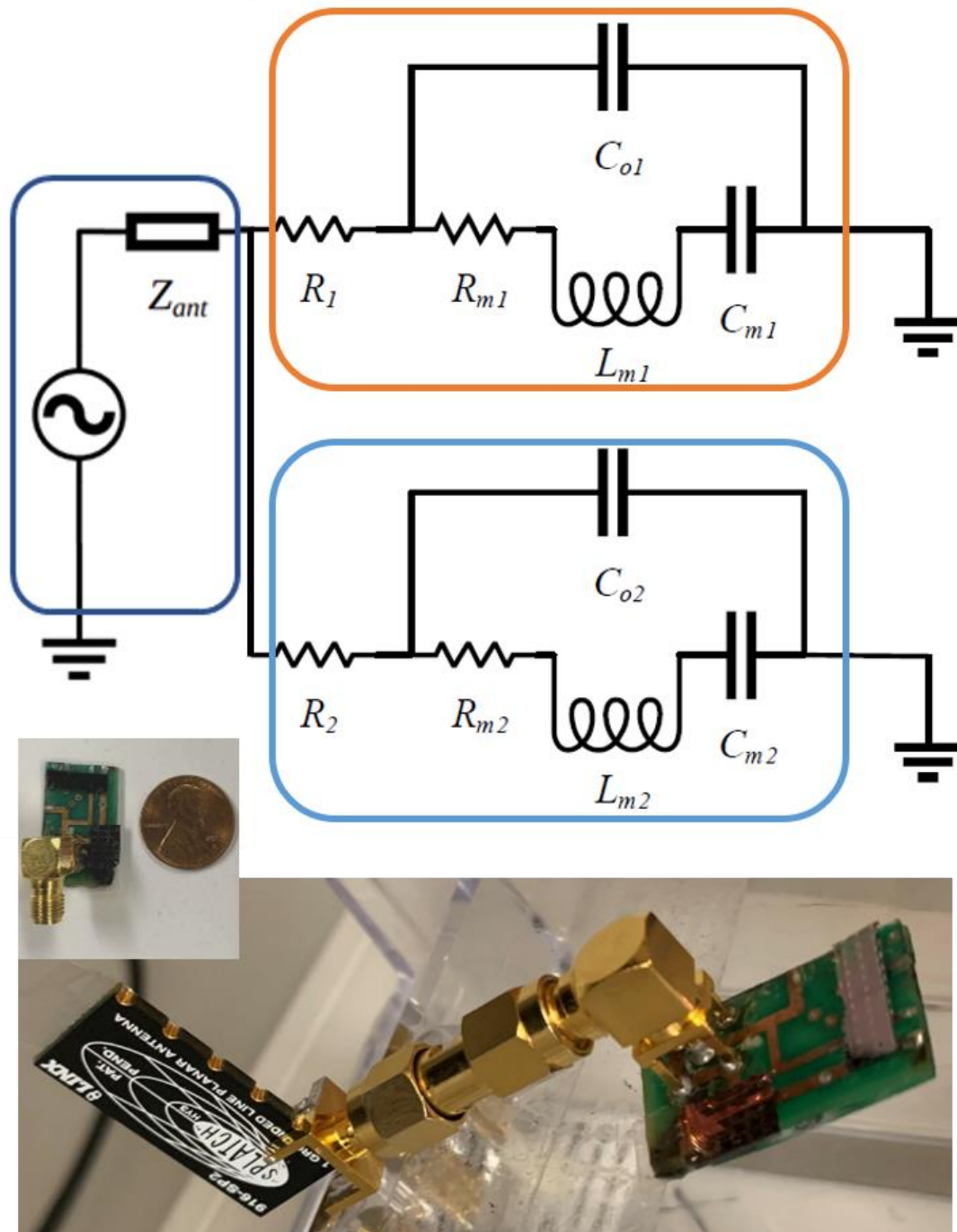
Figure 44. Circuit schematic of the flow rate sensor in receiving mode with the sensor tag shown in the insets. The antenna (outlined in dark blue) is modeled as a voltage source in series with a complex load and the two resonators (highlighted in orange and light blue) were modeled in single port configuration using the mBVD model.

To ensure that the devices exhibit strong resonances after they are electrically connected, the S-parameter of the two resonators is compared to the S-parameters of parallel configuration in Figure 45(a). ADS was also used to simulate the circuit model for the sensor in receiving mode (seen in Figure 44), with the results shown in Figure 45(b). The results demonstrate that for 1W of peak transmitted power provided by an isotropic excitation antenna at a distance of 1.5m, 0.63mW can be predicted to be delivered to each resonator with proper matching network.

4.3 Theoretical Framework

The frequency shift of the two resonators can be explained in terms of temperature and surface vapor adsorption modulation caused by exposure to periodic respiratory flow. Higher values of both parameters decrease the resonance frequency of the TPoS MEMS resonators in our application. A TPoS MEMS resonator's temperature-frequency profile is a function of its resonance mode and constituent materials. Equation (5) can be used to calculate the temperature-induced frequency change of a TPoS MEMS resonator.
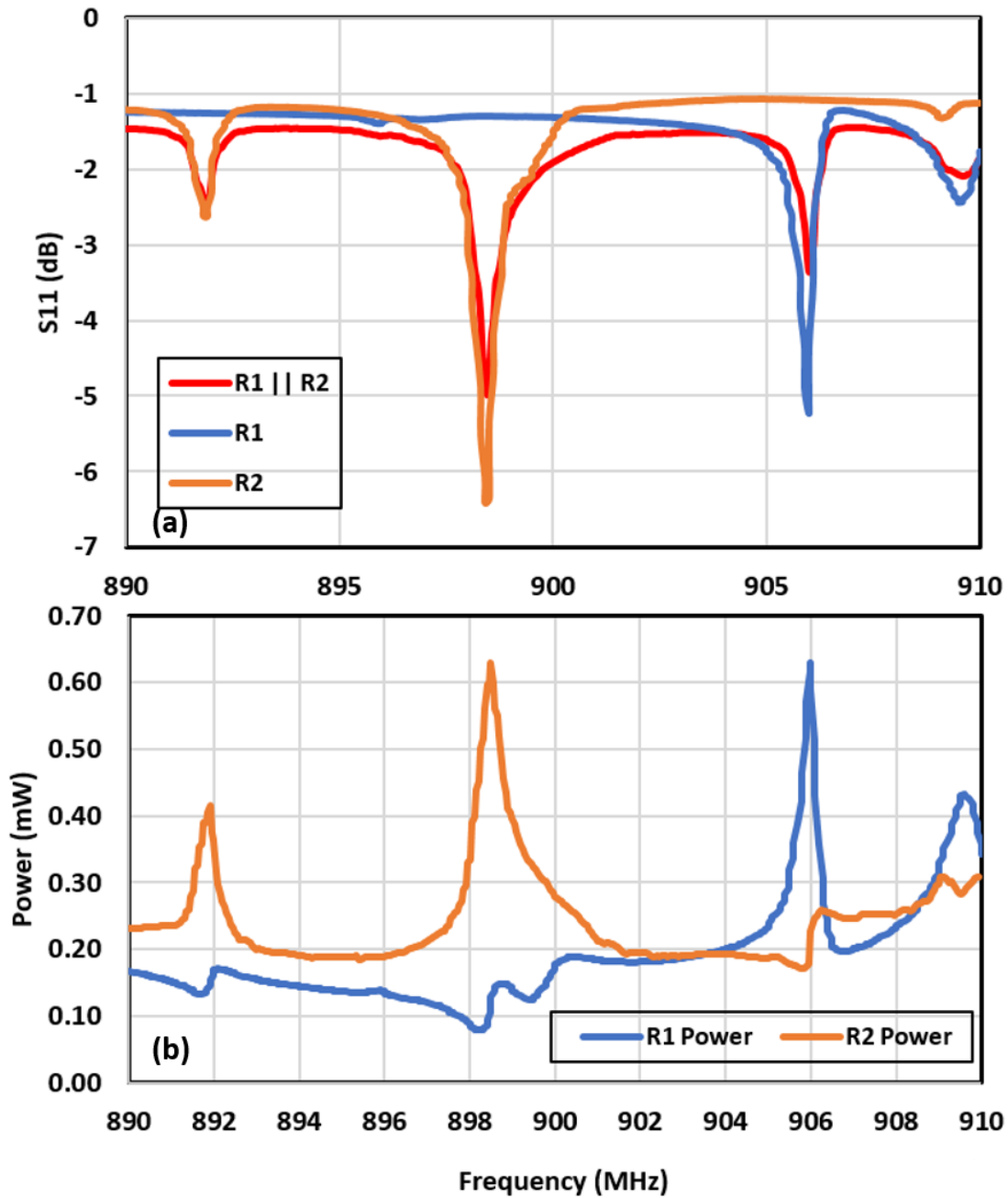
Figure 45. (a) measured S11 of the two resonators (R1 and R2) before being integrated into the sensor as well as the S11 of the two after being connected in parallel as calculated using ADS. (b) power delivered to two resonators for an input power of 1W applied at the shared port of the two resonators [55].

The vapor content of exhaled air from the respiratory tract is higher than that of inhaled air. As a result, the MEMS device's surface experiences a transient adsorption of water vapor during exhalation, which can be considered a loaded mass. Equation (7) can be used to measure the change in resonance frequency induced by water vapor adoration, and Equation (8) can be used to calculate the total shift in frequency (8). It should be noted that coupling mechanisms between temperature change and vapor mass loading would make accurate predictions of the overall frequency shift hard to maintain with analytical equations, therefore finite element analysis is encouraged for this purpose.

4.4 Measurement Results

From a distance of 20cm from the excitation antenna, the sensor was excited with a pulsed sinusoidal signal with a peak power of 12dBm and a second external antenna recorded its response in the form of a decaying sinusoidal signal. The frequency of the excitation signal is set to successively target the frequencies of the two resonators to optimize the power transmitted to the resonator and thus improve the SNR.

The measurement flow chart of the sensing system is shown in Figure 46. The signal generator successively targets the frequency of each of the sensor's two resonators. The Power Amplifier (PA) is optional here and can be either placed in the transmitter pathway or on the receiver side. The signal acquired by the oscilloscope is time gated and following FFT the frequency with maximum amplitude is added to the respiratory

profile. When a sudden drop in frequency is detected in the respiratory profile, the delay in onset of the drop between the two resonators is calculated and converted to flow rate.
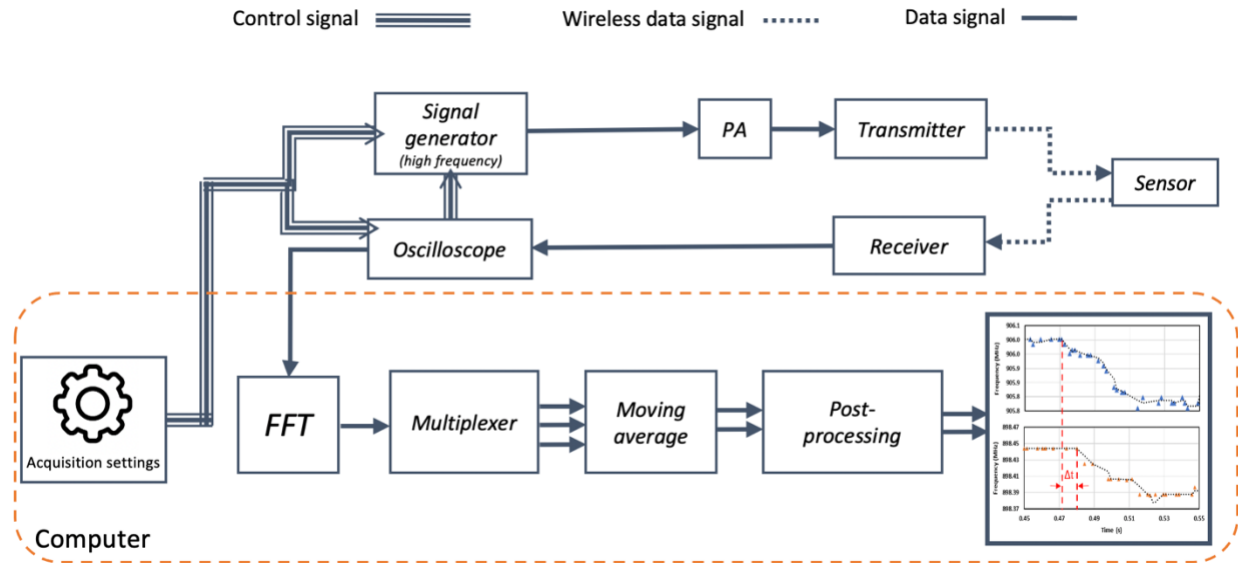
Figure 46. acquisition flow chart of novel time-of-flight flow sensor presented in this chapter. The signal generator successively targets the frequency of each of the sensor's two resonators. The Power Amplifier (PA) is optional here and can be either placed in the transmitter pathway or on the receiver side. The signal acquired by the oscilloscope is time gated and following FFT the frequency with maximum amplitude is added to the respiratory profile. When a sudden drop in frequency is detected in the respiratory profile is detected the delay in onset of the drop between the two resonators is calculated and converted to flow rate.

Figure 47(a) shows the sensor's response (as determined by the receiving antenna) to two excitation signals, one for each of the two resonators. Figure 47(b) represents the FFT spectrum of the sensor's response before and during respiration. During exhalation, note the small drop in frequency in the FFT peak power for both resonators.
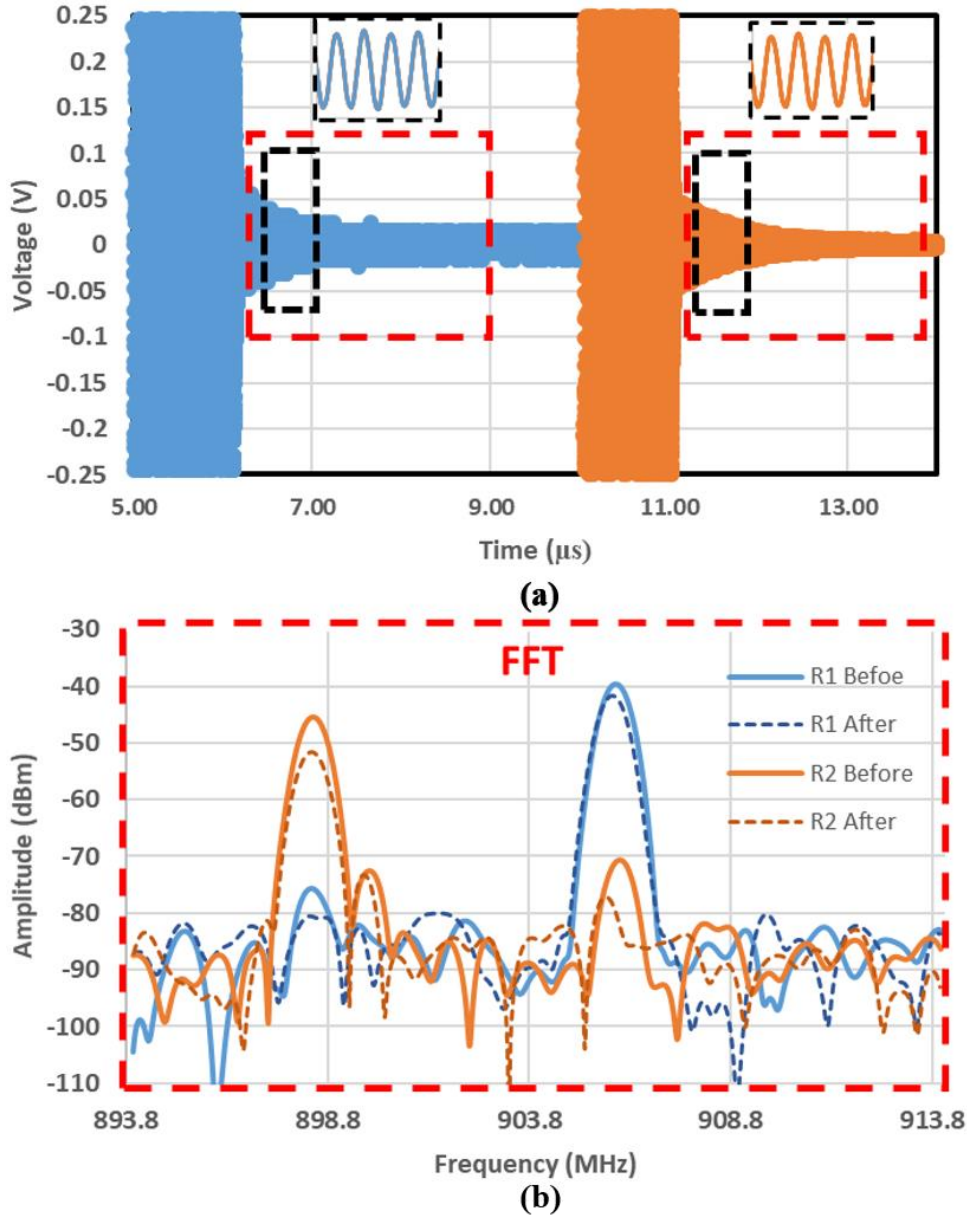
Figure 47. (a) Excitation signal and sensor response as measured by receiving antenna for the 906.9MHz (blue) and 898.4MHz (orange) resonators. (b) FFT spectrum of the time-gated response of the sensor before and directly after impact of exhalatory flow. Notice a small downshift in the FFT peak for both resonators as a result of impact of exhalatory flow.

Figures 48 and 49 show the flow measurement results. In this experiment, the participant was asked to exhale at various flow rates. Exhaled flow rates were determined

using the delay between the onset of frequency shift for the two resonators and were found to be 0.1m/s and 1m/s for the results shown in Figures 48 and 49, respectively.
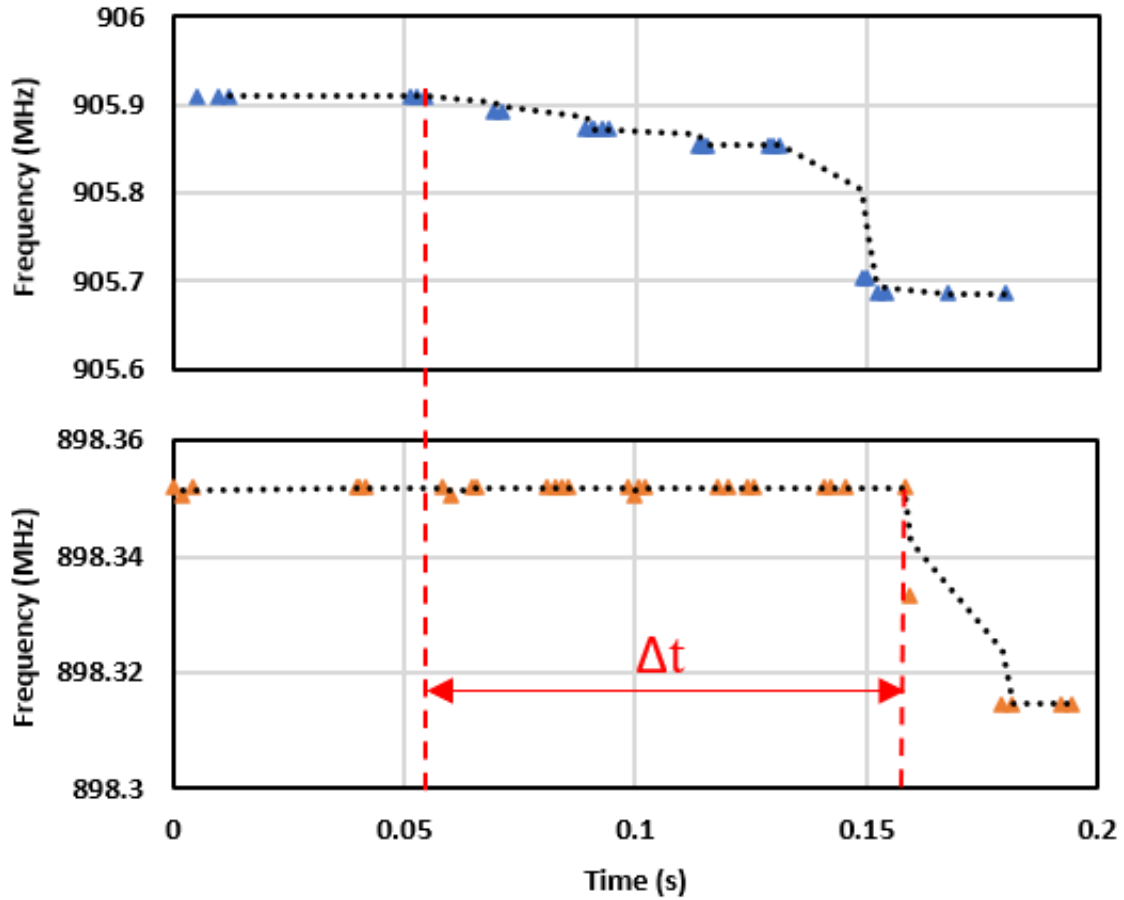
Figure 48. Time series of calculated frequencies of the two resonators (906.9MHz (top) and 898.4MHz (bottom)). The time of impact for either resonator has been marked by a vertical red line with the highlighted delay measured to be corresponding to a respiratory flow rate of ~0.1m/s.
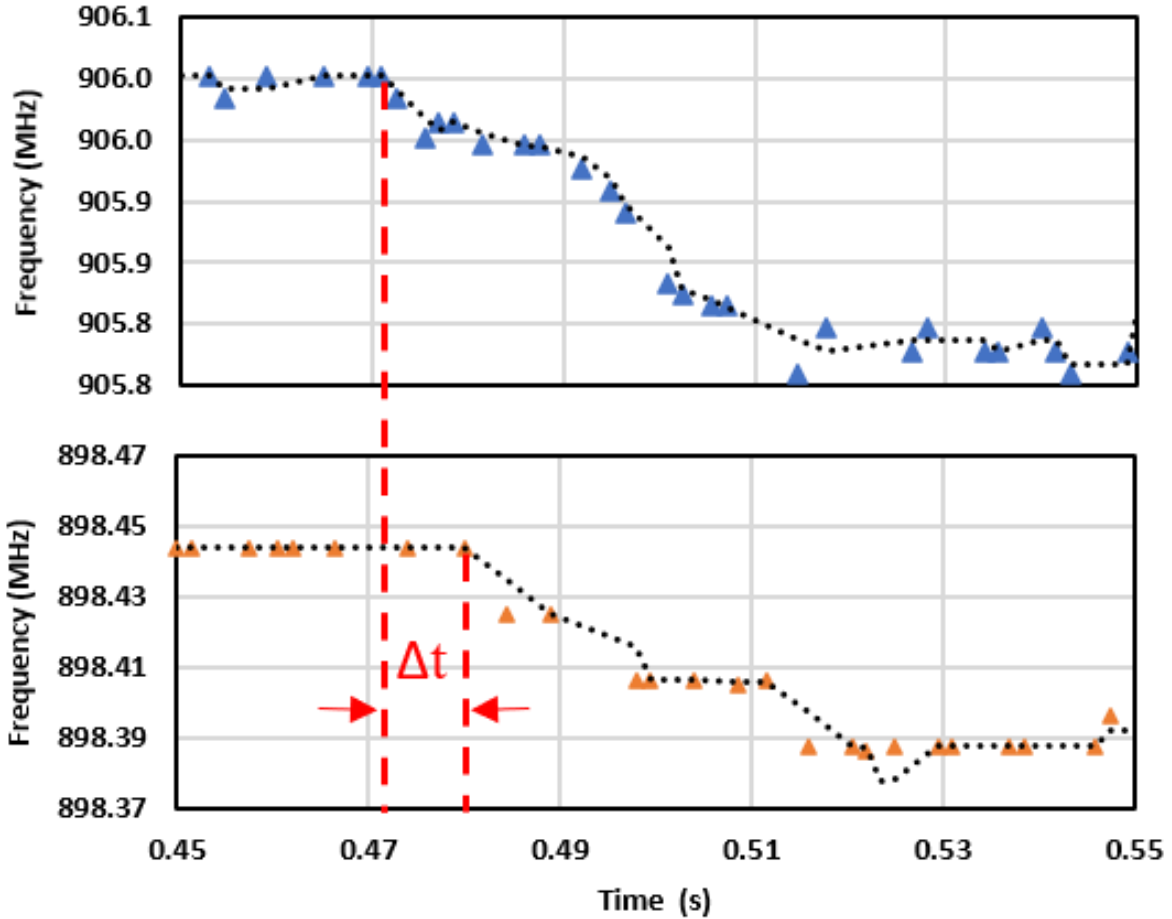
Figure 49. Time series of calculated frequencies of the two resonators (906.9MHz (top) and 898.4MHz (bottom)). The time of impact for either resonator has been marked by a vertical red line with the highlighted delay measured to be corresponding to a respiratory flow rate of ~1m/s.

The acquisition configuration detailed in Figure 46 necessitates that the signal generator switch frequencies intermittently. This limits the time resolution sensing system as: 1- during switch time no signal is transmitted 2- while one resonator is being measured, we are blind to the status of the other resonator. Time resolution of the profile is directly proportional to the maximum detectable flow rate. To improve the acquisition, process a mixer and a secondary signal generator operating at a lower frequency is

incorporated into the sensing system. Using this updated configuration, shown in Figure 50, there is no switching between the resonators' frequencies and the two resonators are excited and measured simultaneously and therefore there is no blind period.
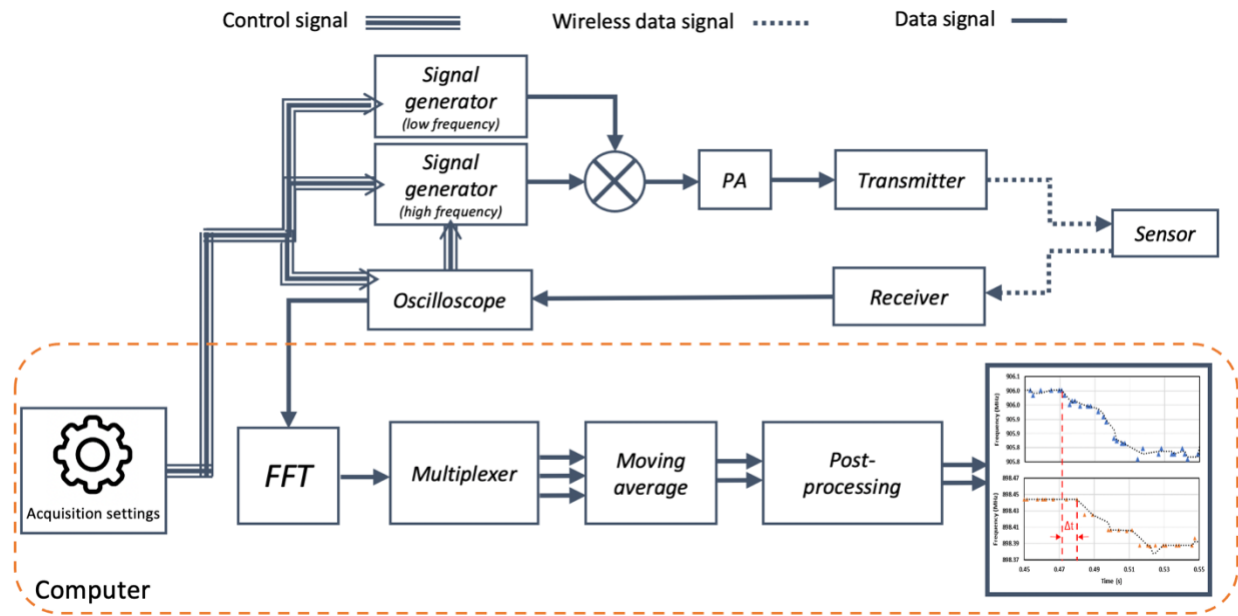
Figure 50. this updated acquisition flow builds on that shown using two signal generators and a mixer. This acquisition configuration removes any blind period in the measurement process, and this improves the maximum detectable respiratory flow rate.

Similar to the sensor described in chapter 3 one of the main advantages of wearable respiratory monitoring systems is their application for detection of respiratory conditions. For example, the applicability of the flow sensor for detecting sudden and brief secession of breathing events associated with sleep apnea is illustrated in Figure 51. Here, the subject was asked to suddenly stop breathing and subsequently resume after a

few seconds. This period is highlighted in red in Figure 51 can be clearly detected from
the response of either resonator.
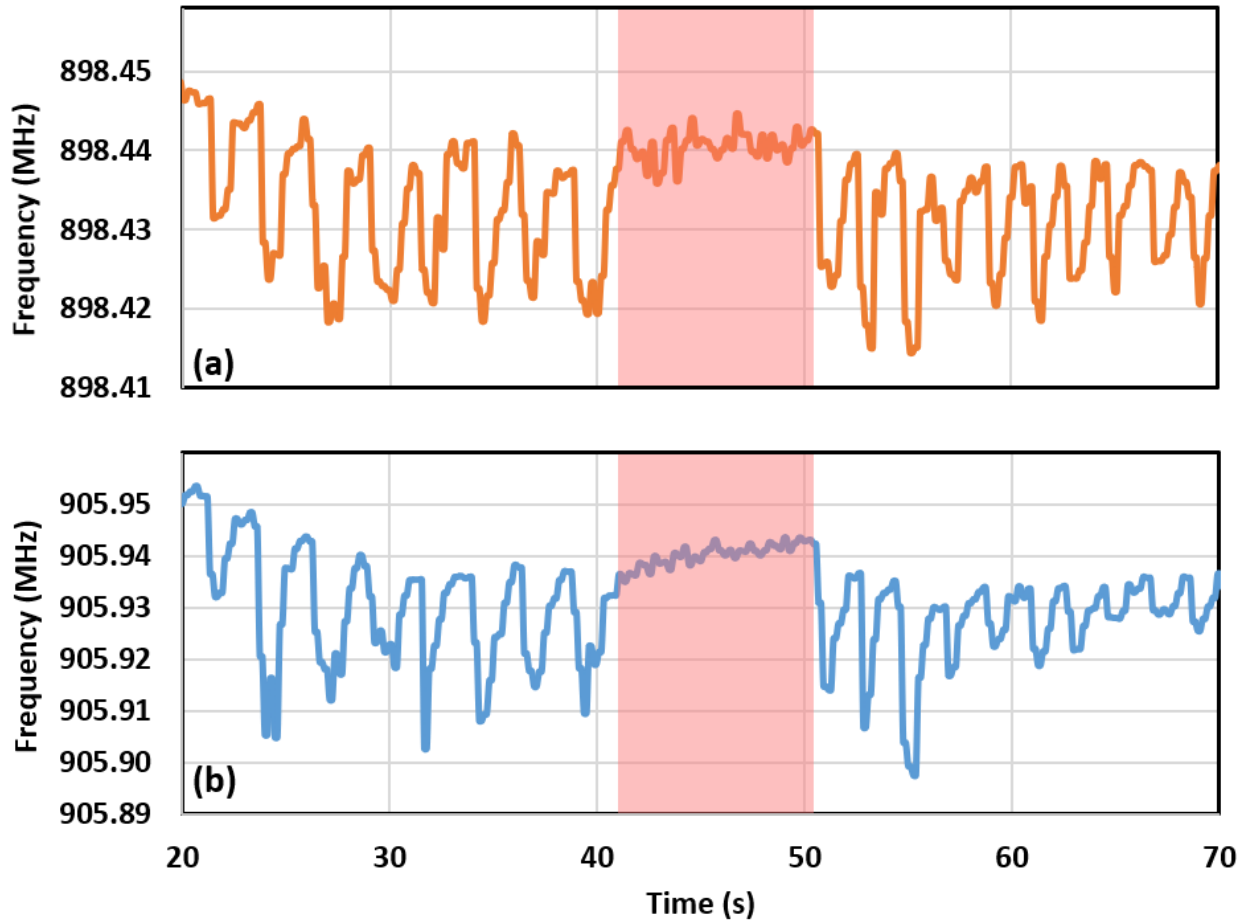
Figure 51. Measured frequency time series of the two resonators (898.4MHz (a)) and (906.9MHz (b)) constituting the respiration profile. Each drop in frequency and subsequent recovery corresponds to a single respiratory cycle. The highlighted time span corresponds to an abrupt cease of breathing by the patient. This experiment was performed to understand the applicability of this sensor for detection of apnea events.

4.5 Conclusion

This chapter introduces a novel method for passive wireless monitoring of respiratory flow rate. Our sensor employs a dual-MEMS architecture, which involves connecting two piezoelectric MEMS resonators that are spaced 1 cm apart and operate at similar frequencies in parallel. The sensor is energized by an external antenna, and the two resonance frequencies are extracted from its response using FFT analysis. The frequency of the resonators is modulated by hot and humid air passing over the sensor, as measured by their ringdown signal sequentially. We were able to determine a human subject's flow rate by measuring the impact delay. The operation of the sensor was found to be dependent on the loss provided by TPoS MEMS resonators, as well as impedance matching between the resonators and the antenna. We demonstrated that, in addition to passively measuring respiration flow rate, the sensor can also detect apnea events via measuring respiratory profile. Because of its small scale, robustness, and low unit cost, this sensing technology holds great promise for wireless multi-modal patient monitoring systems.

APPENDIX: PERMISSIONS FOR REUSING THE

PUBLISHED PAPERS [55,57] IN THE DISSERTATION

1- IEEE:

- **Does IEEE require individuals working on a thesis or dissertation to obtain formal permission for reuse?**

The IEEE does not require individuals working on a thesis to obtain a formal reuse license, however, you must follow the requirements listed below:

Textual Material

Using short quotes or referring to the work within these papers) users must give full credit to the original source (author, paper, publication) followed by the IEEE copyright line © 2011 IEEE.

In the case of illustrations or tabular material, we require that the copyright line © [Year of original publication] IEEE appear prominently with each reprinted figure and/or table.

If a substantial portion of the original paper is to be used, and if you are not the senior author, also obtain the senior author's approval.

Full-Text Article

If you are using the entire IEEE copyright owned article, the following IEEE copyright/ credit notice should be placed prominently in the references: © [year of original publication] IEEE. Reprinted, with permission, from [author names, paper title, IEEE publication title, and month/year of publication]

Only the accepted version of an IEEE copyrighted paper can be used when posting the paper or your thesis on-line.

2- MDPI

REFERENCES

[1]   T. Ferkol and D. Schraufnagel, "The global burden of respiratory disease," *Ann. Am. Thorac. Soc.*, vol. 11, no. 3, pp. 404–406, 2014.

[2]   M. Chu *et al.*, "Respiration rate and volume measurements using wearable strain sensors," *NPJ Digit. Med.*, vol. 2, no. 1, pp. 1–9, 2019.

[3]   J. F. Fieselmann, M. S. Hendryx, C. M. Helms, and D. S. Wakefield, "Respiratory rate predicts cardiopulmonary arrest for internal medicine inpatients," *J. Gen. Intern. Med.*, vol. 8, no. 7, pp. 354–360, 1993.

[4]   C. Subbe, R. G. Davies, E. Williams, P. Rutherford, and L. Gemmell, "Effect of introducing the Modified Early Warning score on clinical outcomes, cardio-pulmonary arrests and intensive care utilisation in acute medical admissions," *Anaesthesia*, vol. 58, no. 8, pp. 797–802, 2003.

[5]   A. Aliverti, "Wearable technology: role in respiratory health and disease," *Breathe*, vol. 13, no. 2, pp. e27--e36, 2017.

[6]   H. Hmeidi *et al.*, "Tidal breathing parameters measured by structured light plethysmography in children aged 2--12 years recovering from acute asthma/wheeze compared with healthy children," *Physiol. Rep.*, vol. 6, no. 12, p.

e13752, 2018.

[7]   M. Folke, L. Cernerud, M. Ekström, and B. Hök, "Critical review of non-invasive respiratory monitoring in medical care," *Med. Biol. Eng. Comput.*, vol. 41, no. 4, pp. 377–383, 2003.

[8]   M. A. Cretikos, R. Bellomo, K. Hillman, J. Chen, S. Finfer, and A. Flabouris, "Respiratory rate: the neglected vital sign," *Med. J. Aust.*, vol. 188, no. 11, pp. 657–659, 2008.

[9]   C. Massaroni, A. Nicolò, D. Lo Presti, M. Sacchetti, S. Silvestri, and E. Schena, "Contact-based methods for measuring respiratory rate," *Sensors*, vol. 19, no. 4, p. 908, 2019.

[10]   M. K. Marks, M. South, and B. G. Carter, "Measurement of respiratory rate and timing using a nasal thermocouple," *J. Clin. Monit.*, vol. 11, no. 3, pp. 159–164, 1995.

[11]   S. Kano, K. Kim, and M. Fujii, "Fast-response and flexible nanocrystal-based humidity sensor for monitoring human respiration and water evaporation on skin," *ACS sensors*, vol. 2, no. 6, pp. 828–833, 2017.

[12]   S.-H. Li, B.-S. Lin, C.-H. Tsai, C.-T. Yang, and B.-S. Lin, "Design of wearable breathing sound monitoring system for real-time wheeze detection," *Sensors*, vol. 17, no. 1, p. 171, 2017.

[13]   P. H. Charlton *et al.*, "Breathing rate estimation from the electrocardiogram and photoplethysmogram: A review," *IEEE Rev. Biomed. Eng.*, vol. 11, pp. 2–20, 2017.

[14]   P. Jiang, S. Zhao, and R. Zhu, "Smart sensing strip using monolithically integrated flexible flow sensor for noninvasively monitoring respiratory flow," *Sensors*, vol. 15, no. 12, pp. 31738–31750, 2015.

[15]   E. Schena, C. Massaroni, P. Saccomandi, and S. Cecchini, "Flow measurement in mechanical ventilation: A review," *Med. Eng. Phys.*, vol. 37, no. 3, pp. 257–264, 2015.

[16]   F. Ejeian *et al.*, "Design and applications of MEMS flow sensors: A review," *Sensors Actuators A Phys.*, vol. 295, pp. 483–502, 2019.

[17]   E. Vanegas, R. Igual, and I. Plaza, "Sensing systems for respiration monitoring: A technical systematic review," *Sensors*, vol. 20, no. 18, p. 5446, 2020.

[18]   P. Höppe, "Temperatures of expired air under varying climatic conditions," *Int. J. Biometeorol.*, vol. 25, no. 2, pp. 127–132, 1981.

[19]   D. E. Hurtado, A. Abusleme, and J. A. P. Chávez, "Non-invasive continuous respiratory monitoring using temperature-based sensors," *J. Clin. Monit. Comput.*, pp. 1–9, 2019.

[20]   S. Moradian, M. J. Modarres-Zadeh, and R. Abdolvand, "Thermal conductivity in

nanoscale polysilicon structures with applications in sensors," *Sensors Actuators, A Phys.*, vol. 295, 2019, doi: 10.1016/j.sna.2019.06.006.

[21]   A. W. Van Herwaarden and P. M. Sarro, "Thermal sensors based on the Seebeck effect," *Sensors and Actuators*, vol. 10, no. 3–4, pp. 321–346, 1986.

[22]   S. D. Min, J. K. Kim, H. S. Shin, Y. H. Yun, C. K. Lee, and M. Lee, "Noncontact respiration rate measurement system using an ultrasonic proximity sensor," *IEEE Sens. J.*, vol. 10, no. 11, pp. 1732–1739, 2010.

[23]   T. G. Beckwith, N. L. Buck, and R. D. Marangoni, "Mechanical Measurements. Vol. 5." Reading, MA, USA: Addison-Wesley, 1969.

[24]   Y. P. Huang, M.-S. Young, and C. C. Tai, "Noninvasive respiratory monitoring system based on the piezoceramic transducer's pyroelectric effect," *Rev. Sci. Instrum.*, vol. 79, no. 3, p. 35103, 2008.

[25]   S. Milici, J. Lorenzo, A. Lazaro, R. Villarino, and D. Girbau, "Wireless breathing sensor based on wearable modulated frequency selective surface," *IEEE Sens. J.*, vol. 17, no. 5, pp. 1285–1292, 2016.

[26]   J. G. Webster, *The Measurement, Instrumentation, and Sensors: Handbook*. Springer Science & Business Media, 1999.

[27]   J. Cooper, "A fast-response pyroelectric thermal detector," *J. Sci. Instrum.*, vol. 39,

no. 9, p. 467, 1962.

[28] E. Schena, D. Tosi, P. Saccomandi, E. Lewis, and T. Kim, "Fiber optic sensors for temperature monitoring during thermal treatments: an overview," *Sensors*, vol. 16, no. 7, p. 1144, 2016.

[29] W.-J. Yoo *et al.*, "Development of respiration sensors using plastic optical fiber for respiratory monitoring inside MRI system," *J. Opt. Soc. Korea*, vol. 14, no. 3, pp. 235–239, 2010.

[30] N. M. White, J. Ash, Y. Wei, and H. Akerman, "A planar respiration sensor based on a capaciflector structure," *IEEE sensors Lett.*, vol. 1, no. 4, pp. 1–4, 2017.

[31] H. Takahashi, N. M. Dung, K. Matsumoto, and I. Shimoyama, "Differential pressure sensor using a piezoresistive cantilever," *J. micromechanics microengineering*, vol. 22, no. 5, p. 55015, 2012.

[32] N. Bu, N. Ueno, and O. Fukuda, "Monitoring of respiration and heartbeat during sleep using a flexible piezoelectric film sensor and empirical mode decomposition," in *2007 29th Annual International Conference of the IEEE Engineering in Medicine and Biology Society*, 2007, pp. 1362–1366.

[33] G. P. Heldt and R. J. Ward, "Evaluation of ultrasound-based sensor to monitor respiratory and nonrespiratory movement and timing in infants," *IEEE Trans. Biomed. Eng.*, vol. 63, no. 3, pp. 619–629, 2015.

[34] N. N. Lepine, T. Tajima, T. Ogasawara, R. Kasahara, and H. Koizumi, "Robust respiration rate estimation using adaptive Kalman filtering with textile ECG sensor and accelerometer," in *2016 38th Annual International Conference of the IEEE Engineering in Medicine and Biology Society (EMBC)*, 2016, pp. 3797–3800.

[35] A. Shahshahani, C. Laverdiere, S. Bhadra, and Z. Zilic, "Ultrasound sensors for diaphragm motion tracking: An application in non-invasive respiratory monitoring," *Sensors*, vol. 18, no. 8, p. 2617, 2018.

[36] P. Jagadev and L. I. Giri, "Non-contact monitoring of human respiration using infrared thermography and machine learning," *Infrared Phys. Technol.*, vol. 104, p. 103117, 2020.

[37] K. Gibson *et al.*, "Non-contact heart and respiratory rate monitoring of preterm infants based on a computer vision system: a method comparison study," *Pediatr. Res.*, vol. 86, no. 6, pp. 738–741, 2019.

[38] P. Sharma, X. Hui, J. Zhou, T. B. Conroy, and E. C. Kan, "Wearable radio-frequency sensing of respiratory rate, respiratory volume, and heart rate," *NPJ Digit. Med.*, vol. 3, no. 1, pp. 1–10, 2020.

[39] Z. M. Rittersma, "Recent achievements in miniaturised humidity sensors—a review of transduction techniques," *Sensors Actuators A Phys.*, vol. 96, no. 2–3, pp. 196–210, 2002.

[40]   B. Li, Q. Tian, H. Su, X. Wang, T. Wang, and D. Zhang, "High sensitivity portable capacitive humidity sensor based on In2O3 nanocubes-decorated GO nanosheets and its wearable application in respiration detection," *Sensors Actuators B Chem.*, vol. 299, p. 126973, 2019.

[41]   S. Kano, A. Yamamoto, A. Ishikawa, and M. Fujii, "Respiratory rate on exercise measured by nanoparticle-based humidity sensor," in *2019 41st Annual International Conference of the IEEE Engineering in Medicine and Biology Society (EMBC)*, 2019, pp. 3567–3570.

[42]   D. Lo Presti *et al.*, "Agar-coated fiber Bragg grating sensor for relative humidity measurements: Influence of coating thickness and polymer concentration," *IEEE Sens. J.*, vol. 19, no. 9, pp. 3335–3342, 2019.

[43]   S. Nurulain, M. R. Radin, K. Suzalina, and H. Manap, "Spectra comparison for an optical breathing gas sensor development," in *AIP Conference Proceedings*, 2017, vol. 1835, no. 1, p. 20035.

[44]   I. Alikhani, K. Noponen, A. Hautala, R. Ammann, and T. Seppänen, "Spectral fusion-based breathing frequency estimation; experiment on activities of daily living," *Biomed. Eng. Online*, vol. 17, no. 1, pp. 1–12, 2018.

[45]   H. R. W. Touw *et al.*, "Photoplethysmography respiratory rate monitoring in patients receiving procedural sedation and analgesia for upper gastrointestinal

endoscopy," *J. Clin. Monit. Comput.*, vol. 31, no. 4, pp. 747–754, 2017.

[46] S. A. Zawawi, A. A. Hamzah, B. Y. Majlis, and F. Mohd-Yasin, "A review of
MEMS capacitive microphones," *Micromachines*, vol. 11, no. 5, p. 484, 2020.

[47] M. Varanis, A. Silva, A. Mereles, and R. Pederiva, "MEMS accelerometers for
mechanical vibrations analysis: A comprehensive review with applications," *J.
Brazilian Soc. Mech. Sci. Eng.*, vol. 40, no. 11, pp. 1–18, 2018.

[48] C.-Y. Chen, M.-H. Li, and S.-S. Li, "CMOS-MEMS resonators and oscillators: A
review," *Sensors Mater.*, vol. 30, no. 4, pp. 733–756, 2018.

[49] R. Aigner, "BAW Filters and Duplexers for Mobile Communication," in
Piezoelectric MEMS Resonators, Springer, 2017, pp. 387–413.

[50] G. Piazza, P. J. Stephanou, and A. P. Pisano, "Piezoelectric aluminum nitride
vibrating contour-mode MEMS resonators," *J. Microelectromechanical Syst.*, vol. 15,
no. 6, pp. 1406–1418, 2006.

[51] H. Fatemi and R. Abdolvand, "Fracture limit in thin-film piezoelectric-on-
substrate resonators: Silicon VS. diamond," in *2013 IEEE 26th International
Conference on Micro Electro Mechanical Systems (MEMS)*, 2013, pp. 461–464.

[52] H. Fatemi, "Performance optimization of lateral-mode thin-film piezoelectric-on-
substrate resonant systems," 2015.

[53]   S. Moradian, "Wearable Passive Wireless MEMS Respiration Sensor," 2017.

[54]   J. D. Larson, P. D. Bradley, S. Wartenberg, and R. C. Ruby, "Modified Butterworth-Van Dyke circuit for FBAR resonators and automated measurement system," in *2000 IEEE Ultrasonics Symposium. Proceedings. An International Symposium (Cat. No. 00CH37121)*, 2000, vol. 1, pp. 863–868.

[55]   S. Moradian, P. Akhkandi, H. Fatemi, and R. Abdolvand, "Wireless Passive Time-of-Flight Respiratory MEMS Flow Rate Sensor," in *2020 Joint Conference of the IEEE International Frequency Control Symposium and International Symposium on Applications of Ferroelectrics (IFCS-ISAF)*, 2020, pp. 1–4.

[56]   R. Abdolvand, H. Fatemi, and S. Moradian, "Quality Factor and Coupling in Piezoelectric MEMS Resonators," 2017, pp. 133–152.

[57]   S. Moradian and R. Abdolvand, "Mems-based passive wireless respiration profile sensor," in *2016 IEEE SENSORS*, 2016, pp. 1–3.

[58]   R. Abdolvand, H. M. Lavasani, G. K. Ho, and F. Ayazi, "Thin-film piezoelectric-on-silicon resonators for high-frequency reference oscillator applications," *IEEE Trans. Ultrason. Ferroelectr. Freq. Control*, vol. 55, no. 12, pp. 2596–2606, 2008.

[59]   H. Fatemi, H. Zeng, J. A. Carlisle, and R. Abdolvand, "High-frequency thin-film AlN-on-diamond lateral--extensional resonators," *J. microelectromechanical Syst.*, vol. 22, no. 3, pp. 678–686, 2013.

[60] H. Fatemi and R. Abdolvand, "Low-loss lateral-extensional piezoelectric filters on ultrananocrystalline diamond," *IEEE Trans. Ultrason. Ferroelectr. Freq. Control*, vol. 60, no. 9, pp. 1978–1988, 2013.

[61] C.-M. Lin, T.-T. Yen, V. V Felmetsger, M. A. Hopcroft, J. H. Kuypers, and A. P. Pisano, "Thermally compensated aluminum nitride Lamb wave resonators for high temperature applications," *Appl. Phys. Lett.*, vol. 97, no. 8, p. 83501, 2010.

[62] R. Farraro and R. B. McLellan, "Temperature dependence of the Young's modulus and shear modulus of pure nickel, platinum, and molybdenum," *Metall. Trans. A*, vol. 8, no. 10, pp. 1563–1565, 1977.

[63] J.-P. Chen and P. Hsu, "A compact strip dipole coupled split-ring resonator antenna for RFID tags," *IEEE Trans. Antennas Propag.*, vol. 61, no. 11, pp. 5372–5376, 2013.

[64] C. A. Balanis, *Antenna theory: analysis and design*. John wiley & sons, 2016.

[65] R. Abdolvand, H. Fatemi, and S. Moradian, "Quality factor and coupling in piezoelectric mems resonators," in *Piezoelectric MEMS Resonators*, Springer, 2017, pp. 133–152.

[66] J. Stocks, P. D. Sly, R. S. Tepper, and W. J. Morgan, *Infant respiratory function testing*. John Wiley & Sons, 1996.

[67]   A. Fleisch, "Der pneumotachograph; ein apparat zur

        geschwindigkeitsregistrierung der atemluft," *Pflüger's Arch. für die gesamte Physiol.*

        des Menschen und der Tiere, vol. 209, no. 1, pp. 713–722, 1925.

[68]   J. C. Lilly, "Flow meter for recording respiratory flow of human subjects,"

        Methods Med. Res., vol. 2, pp. 113–121, 1950.

[69]   G. Tardi, C. Massaroni, P. Saccomandi, and E. Schena, "Experimental assessment

        of a variable orifice flowmeter for respiratory monitoring," *J. Sensors*, vol. 2015,

        2015.

[70]   C. Sharp *et al.*, "Toward respiratory assessment using depth measurements from a

        time-of-flight sensor," *Front. Physiol.*, vol. 8, p. 65, 2017.

[71]   Y. I. Sokol, R. S. Tomashevsky, and K. V Kolisnyk, "Turbine spirometers

        metrological support," in *2016 International Conference on Electronics and

        Information Technology (EIT)*, 2016, pp. 1–4.

[72]   U. Goreke, S. Habibiabad, K. Azgin, and M. I. Beyaz, "A MEMS turbine prototype

        for respiration harvesting," in *Journal of Physics: Conference Series*, 2015, vol. 660,

        no. 1, p. 12059.

[73]   "thermal flow sensor wiki."

        https://en.wikipedia.org/wiki/Thermal_mass_flow_meter.

[74] C. Massaroni, D. Lo Presti, P. Saccomandi, M. A. Caponero, R. D'Amato, and E. Schena, "Fiber Bragg grating probe for relative humidity and respiratory frequency estimation: assessment during mechanical ventilation," *IEEE Sens. J.*, vol. 18, no. 5, pp. 2125–2130, 2017.

[75] E. Schena, P. Saccomandi, and S. Silvestri, "A high sensitivity fiber optic macro-bend based gas flow rate transducer for low flow rates: Theory, working principle, and static calibration," *Rev. Sci. Instrum.*, vol. 84, no. 2, p. 24301, 2013.

[76] E. Meng, P.-Y. Li, and Y.-C. Tai, "A biocompatible Parylene thermal flow sensing array," *Sensors Actuators A Phys.*, vol. 144, no. 1, pp. 18–28, 2008.

[77] S. F. Mousavi, S. H. Hashemabadi, and H. A. Moghaddam, "Design, simulation, fabrication and testing of ultrasonic gas flowmeter transducer (sensor)," *Sens. Rev.*, 2019.

[78] C. Dam-Hansen and S. R. Kitchen, "Holographic optical element for laser time-of-flight flow sensor," *Opt. Lasers Eng.*, vol. 44, no. 9, pp. 954–964, 2006.